Summary of Revisions

We thank all the reviewers for these very helpful reviews. We appreciate the careful scrutiny of our mechanistic work, especially as it pertains to organic photolysis.

Reviewers 1 and 2 provided a number of important, overlapping comments. Before addressing each point, we would like to summarize the main changes to the manuscript. All changes made to the manuscript are highlighted in red text.

(1) As the reviewers point out, we did not clarify the sources that were used to evaluate photolysis frequencies. We apologize for this oversight. All of the photolysis parameters used in modeling the mini chamber were calculated using published cross-sections, known or estimated quantum yields, and the reported photon flux at 254 nm. We have added 2 tables in the supplemental information that summarize the sources used to calculate photolysis frequencies employed in the MCM (Table S1) as well as other reactions that were added to the mini chamber model to account for photolysis of primary species and NOx reservoirs (Table S2). In general, we use sources recommended by the MCM, unless these sources do not report cross-sections at 254 nm. The ambient model utilizes the MCM parameterizations relevant to ambient photolysis. We have also added text to the manuscript on pages 8 and 9 to describe these calculations.
(2) In light of revision (1), we have also clarified the purpose of the mini chamber model to acknowledge the uncertainties associated with photolysis. The primary reason for incorporating furan mechanisms into the MCM is for use in understanding VOC oxidation in ambient plumes. Our intention for modeling the mini chamber was to evaluate the likely identities of secondary NMOG detected by PTR-ToF-MS (e.g. maleic anhydride) and I-CIMS (e.g. hydroxyfuranones), and to show that furan chemistry plays an important role in this formation. We have added text on page 8 to explain the scope of the mini chamber analysis.
(3) We have included a FACSIMILE + readme file that includes the full mechanism used in this modeling - i.e., MCM 3.3.1 + furans.
(4) We have speciated the monoterpenes to account for differences in reactivity between exocyclic and endocyclic double bonds. We have also updated the RO2 + HO2 rate constants to account for carbon number. All of the graphs and tables have been updated to reflect these changes.

Reviewer 1 Comments

This paper investigates the role of a number of identified furans and other oxygenated aromatic compounds in the chemistry of ageing biomass burning emissions. Chemical schemes are developed for these species, and are used to extend the chemistry in the Master Chemical Mechanism (MCM). The extended mechanism is used to interpret the results of simulation experiments in which biomass burning smoke is oxidized in a chamber under illumination from UVC lamps; and the description of secondary organic compound formation (measured by PTR-ToF-MS) is reported to be improved. The

mechanism is also tested in a Lagrangian box model used previously to model a real biomass burning plume. This is reported to provide an improved representation of the chemistry in biomass plumes, in particular the formation of maleic anhydride which may be used as a tracer for this source. This is an interesting piece of work, providing results and interpretation that will potentially help to improve the understanding and representation of the chemistry of ageing biomass burning emissions. The work is suitable for publication in ACP, but there are a number of points where additional clarification and information would seem to be required. The authors should address the following comments in producing a revised version of the manuscript.

We thank the reviewer for their careful evaluation of our mechanistic work. Please find our responses to these comments below.

1) Lines 107-115: Some information is given here on primary OH radical sources in the“mini-chamber”, and more generally in Sect. 3.2.3 and the SI about photolysis rates using the UVC lamps. MCM v3.3.1 recommends sources of cross-section and quantum yield data in relation to the specific and generic photolysis processes it represents. Can the authors confirm that these were used, or provide more details on what information was used (e.g.in Table S1 for emitted compounds and elsewhere for product species, e.g. carbonyls, hydroperoxides and nitrates)?

   Thank you for this helpful comment. In general, we used the recommended sources from the MCM, unless these sources did not report cross sections at 254 nm, or higher resolution data were available. These sources and assumptions are provided in Tables S1 and S2, as described in the Summary of Revisions.

2) Line 122. It is stated that “Gas-phase species have a high affinity to metal surfaces....”Acetonitrile is a gas phase species, but is assumed not to be lost to surfaces (stated in the SI). Perhaps a little more information on this is required in the manuscript, including a reference to support the acetonitrile assumption

   Thank you for pointing this out - we could have been more clear about what we meant by this analysis. VOC losses to metal surfaces were studied by Deming et al. (2019), who showed that metal tubing effects are largely driving by volatility, functionality, and displacement processes at adsorption sites. However, all VOCs that were studied by Deming et al. (2019) had some delay through metal tubing. Our assumption was that acetonitrile is not lost to a greater extent than other species, given its higher volatility. In truth, we are not concerned by absolute losses (we acknowledge that assessing absolute losses is difficult), but rather relative differences in the NMOG distribution between the stack and chamber. The analysis in the SI shows that NMOG/acetonitrile ratios between stack and mini chamber were different (on average 15% lower in the mini chamber), but were not orders of magnitude different, which implies that the VOC distribution in

the mini chamber is reasonably representative of the mixture sampled from the stack.

We have clarified this in the main text, as well as in the SI.

3) "Deuterated butanol" is abbreviated as "d-butanol". Neither of these terms tell the reader what the molecule actually is, and more clarification is required. Indeed, the prefix "d-" (as opposed to "l-") usually specifies the rotation direction of optical activity...and this is not relevant in this case. Assuming "deuterated butanol" is the same species for which Barmet et al. (2012) measured the OH rate coefficient(line 139), it is CD3CD2CD2CD2OH. This should be identified as "1-butan-d9-ol" or"butanol-d9".

   Thank you for the clarification on butanol-d9. The molecule is the same as described by Barmet et al. We've updated the molecular name to be consistent with your recommendation for butanol-d9

4) A little more explanation could be provided on the deviations between chamber and ambient chemistry that occur at high OHR, and why values of 70 s-1 and below are acceptable.

   Peng et al. (2016) recommend OHR values less than ~50 - 100 s^{-1} when operating oxidation flow reactors using 254 nm. We now note this in the text.

5) The use of the MCM a-pinene mechanism alone to represent all monoterpenes seems unnecessarily simplistic. As stated, the MCM includes a-pinene, b-pinene and limonene as examples of monoterpenes respectively containing endocylic-,exocyclic- and endocyclic- + exocyclic- double bonds, and therefore has significant coverage of the list given previously on line 390. An improved approach would surely have been to represent those three monoterpenes explicitly, and use them as mechanistic surrogates for the remaining ones. For example, the OH- and O3- initiation reactions for camphene (containing an exocyclic- double bond) could be included explicitly in the mechanism, but represented to form the corresponding products in the b-pinene scheme (this being the closest structural representative).

   We agree with the reviewer that this may be an over simplification. The purpose of Figure S3 is primarily to show that the signal we detect at m/z 137 is unaffected by the fragmentation of other masses detected by PTR-ToF-MS. We do this because the monoterpenes are a significant contributor to OH reactivity in the mini chamber, and we want to be sure that are only quantifying monoterpenes.

   We originally treated all monoterpenes as alpha pinene simply to capture the primary OH reactivity; however, we do agree that some degree of speciation is pertinent. In Figure S3, we now also include the monoterpene speciation for

Engelmann spruce. We feel the best approach would be to use this speciation for the F26 experiment (Figure S3), and the speciation reported from Hatch et al. (2015) for ponderosa pine in modeling F38. We now separate the signal measured by PTR-ToF-MS to alpha pinene, beta pinene, and limonene using the monoterpene speciation described above, then lump other species to these surrogates based on exocyclic- and endocyclic- double bonds. We have added these details to the main text.

6) Hydroperoxide photolysis is a slow process in the atmosphere, even if much more rapid with 254 nm illumination in the chamber. What photolysis rates are used? Reaction with OH will almost certainly dominate in the atmosphere. Have you investigated the effect of assuming a radical forming process (photolysis) in place of a radical propagating process (OH reaction) in the ambient plume simulations?

   We apologize, our explanation of the hydroperoxide fate was incomplete and we appreciate this comment. We glossed over these details because in the ambient plume, the fate of the RO2 radical is predominantly reaction with NO; therefore, hydroperoxide formation from RO2 + HO2 is not considered significant for ambient analysis. We recognize that this is an oversight for the mini chamber, and that additional details are needed. We do incorporate OH reactions for the hydroperoxides, and the fate is different depending on structure. For all hydroperoxides, we assume a photolysis frequency equivalent to that of methyl hydroperoxide (J<41> in the MCM). For hydroperoxides with a hydrogen alpha to the peroxide, we assume that this hydrogen is abstracted, and that the resulting radical quickly decomposes to form a carbonyl + OH (example: HYDFURANOOH, Fig S4), which is analogous to the reactions that occur for aromatic and alkane hydroperoxides. For other hydroperoxides (e.g. HYDDIMEFURANOOH, which has no alpha H, Fig S), we assume that the hydrogen of the peroxide group is abstracted, and that the RO2 radical is recycled. All of these reactions occur with a rate constant of 4e-11 (consistent with other hydroperoxides in the MCM). We did not list these reactions in the supplemental figures, but have now added these for clarity. We have also clarified this in the main text.

7) It would be a very helpful service to the community if the added chemistry was also provided in the form of a reaction listing that can be used in conjunction with MCM v3.3.1. It should also be made clear that expressions like "the updated MCM" used at various points in the manuscript do not imply that the MCM itself has been updated. Perhaps "the extended MCM" or "the customized MCM" would be more appropriate.

   We agree with the reviewer on phrasing and have changed “updated MCM” to “customized MCM”. We also agree that including the mechanism would be useful to the community, and we have added the FACISIMILE file as supplemental information. This file contains all of the reactions used to model the mini chamber

and ambient plume, but a readme file explains which reactions were added based on this work.

8) kRO2HO2 actually has a size-dependence term in the MCM, based on carbon number (see Saunders et al., 2003). The quoted rate constant is the limiting value at high carbon number. Was this taken into account?

   Thank you for catching this. We did not incorporate the size-dependence term in our previous draft. We now include these factors (0.62 for C4, 0.7 for C5 RO2s, 0.77 for C6), which is reflected in the main text, mechanisms, and SI figures.

9) Although MCM v3.3.1 does not generally contain RO2 H-shift isomerization reactions, it does contain those specifically identified to occur during the degradation of isoprene (see Jenkin et al., 2015), which is included in the speciation applied in this study. Perhaps this statement should be qualified accordingly.

   We've added a statement qualifying the isomerization reactions.

10) If butanol-d9 is a significant contributor to OH reactivity, this approach would seem over simplified. Fig. 7 suggests use of 45 ppb, equating to and OH reactivity of about 3.8 s-1 - compared with about 2.3 s-1 for 5-methylfurfural and 2-methylfurancollectively. If this latter pair is significant (as stated on line 399) then butanol-d9 is even more significant and it would seem prudent to represent its chemistry more explicitly.

    The statement about OH reactivity for furans is specifically aimed at assessing missing reactivity in biomass burning emissions, rather than the mixture in the mini chamber. We appreciate that butanol-d9 will contribute to OH reactivity in the mini chamber (our estimates are ~5%), but we expect that the products will only be a small fraction of reactivity. We feel that the reaction that we do add for butanol-d9 is enough to capture the primary OH reactivity of this species (butanol-d9 + OH = butanol-d9 products + HO2). Since we are focused on developing a mechanism that could be used for ambient biomass burning plumes, we don't aim to dig deeply into the chemistry of butanol-d9.

11) There is also the possibility that its degradation might form products of masses that interfere with those from the studied oxygenated compounds, and this should be checked. Based on a quick appraisal, I think one product type (C4H2D8O3 - i.e.CD3CD2CD(OOH)CD2OH and CD3CD(OOH)CD2CD2OH) is formed in the first generation of oxidation of butanol-d9, from RO2 + HO2 reactions. This has an interfering mass of interest (114), which I believe is isobaric with methyl hydroxy furanone and beta-acetylacrylic acid.

Our PTR-ToF-MS has the resolution (R ~ 4000) to separate isobaric species. In general, we are only concerned with overlaps in isomers. We do detect the products of butanol-d9 oxidation (mostly as proton-transfer fragments); however, these species have a significant positive mass defect that does not interfere with the quantification of non-deuterated molecules.

12) Presumably, the slower decay might also result from formation of isobaric products in the system?

This is a very good point. We've added a sentence mentioning that part of this disagreement could be due to the formation of isomers.

13) Statements like "....chemical pathways that are unaccounted for within MCM v 3.3.1" are very easy to include as explanations, but are often not backed up by evidence or specific examples. The degradation of almost all VOCs produces formaldehyde, and this is actually generally found to be substantial and quite well represented in MCM. For example, looking at your list of species, the 3 most abundant (after formaldehyde itself) are 1-butene, methanol and ethene, with these making a collectively significant contribution to the OH reactivity. 1-butene and methanol generate formaldehyde essentially quantitatively (on a molar basis) from radical propagation pathways in the first oxidation step, with ethene producing about 1.7 molecules of formaldehyde. MCM represents this very well, and continues to represent formaldehyde formation from the further oxidation of C2 and higher products (e.g. C2H5CHO from 1-butene). Going on down the list, most of the species make formaldehyde from first- and/or higher-generation chemistry in MCM v3.3.1 - but with the obvious exceptions being species that do not contain a -CH2- substructure (e.g. ethyne, formic acid, glyoxal, phenol and benzene) which cannot make formaldehyde. The much more likely explanation for the under-representation of formaldehyde formation is therefore missing species in the starting speciation. It might also be very sensitive to uncertainties in the [NO] initialization in the model, as this would influence the relative importance of radical propagation and radical termination processes.

We completely agree with the reviewer, and we appreciate the need for clarifying these semantics. Our intention with that statement was much more broad. When we referred to "chemical processes," we also mean to say that there are likely other precursors of formaldehyde that are not measured well by PTR-ToF-MS, and therefore their chemistry is not represented. There are also uncertainties about photolysis and to what degree does the use of 254 nm light contribute to formaldehyde formation. We've clarified this message to highlight all these uncertainties.

We would like to note that the presentation of formaldehyde is primarily to show species that are typically regarded as secondary. We've removed the statement about "Additional work is needed to better describe small oxygenate formation"

since these oxygenates are not a primary focus of this study and, as the reviewer points out, this statement is not supported by a thorough analysis.

14) MCM only includes RO2 + NO2 for acyl peroxy radicals and CH3O2. The reaction is not represented in most cases because the RO2NO2 products are thermally unstable and rapidly regenerate RO2 and NO2 (as indeed the CH3O2 + NO2reaction does at 298 K). The RO2 + NO2 contribution is therefore probably dominated by a very limited set of reactions. The C1 reaction is only CH3O2+NO2, C2 is probably dominated by CH3C(O)O2 + NO2, C3 by C2H5C(O)O2 + NO2: and the small C7contribution is probably mainly C6H5C(O)O2 + NO2. Figure 9 therefore suggests that this limited set of reactions has a big effect. It might also be more correct to check the back decomposition rates for RO2NO2 = RO2 + NO2 and to present the net (forward minus reverse) effect of the RO2 + NO2 reaction - particularly for CH3O2 + NO2 =CH3O2NO2. Note also that the decomposition rates are very sensitive to temperature. Was temperature measured in the mini-chamber and taken into account in the simulations?

We thank the reviewer for this comment - we agree, this graph is a bit misleading as presented. Our intention with this graph is not to show the net products, but rather the relative importance of each RO2 pathway to a given RO2 species. We agree with the reviewer that this graph inflates the influence of CH3O2NO2 due to the cycling between the RO2 radical and the semi-stable intermediate. As presented, it would seem that NOx losses due to CH3O2NO2 formation are enormous! We do constrain the rate constant based on the temperature measured in the mini chamber, and CH3O2NO2 does fall apart quickly following formation.

We've changed this graph to show the relative contributions within each carbon category. We believe this more clearly shows our intended message, that RO2 pathways in ambient plumes and those in the mini chamber were different.

15) Line 399: "2-dimethylfuran" should be either "2-methylfuran" or "2,5-dimethylfuran".

We have changed this to read 2,5-dimethylfuran

16) Line 586: "undesireable" should be "undesirable"

We have made the correction

Reviewer 2 Comments

Coggon et al., have used an extensive data set of PTR-ToF-MS and I-CIMS measurements, carried out during a wide range of chamber biomass burning /OH

oxidation experiments in order to investigate the impact of a range of observed emitted furans and oxygenated aromatics on the formation of secondary reactive VOC and ozone in aged smoke. This was inferred from model/measurement comparisons of detailed chemical box modelling, where schemes from the Master Chemical Mechanism (MCMv3.3.1)were updated and extended. The results highlight significant formation of a range of C4 and C5 anhydrides and furanone species in aged biomass burning plumes. The derived mechanisms were put into a Lagrangian box model in order to model the chemical evolution of a real life biomass burning again highlighted the importance of furan chemistry and its impact on ozone formation. The work presented is scientifically and mechanistically interesting and the comprehensive compositional measurement dataset, mechanism development and model interpretation work significantly adds to our further understanding of the atmosphereic impact of biomass burning on fundamental atmospheric chemistry and air quality. The work is very much suitable for publication in ACP, after the following comments and clarifications have been addressed.

We thank the reviewer for their time in reviewing our work and helpful comments. Please find our responses below.

1) “mini-chamber” experiments and the use of UVC lamps as a large, “clean” source of OH

   The burn smoke is diluted with humidified air (why 30%?) and introduced into the mini-chamber along with ozone (why 70 ppb?), where the chamber reactive mixture is exposed to (predominantly?) 254 nm UVC radiation in order to produce OH to initiate the chemical degradation of the chamber mix. Therefore, the chemistry in the system is not carried out under atmospherically relevant conditions, these studies are aimed mainly at looking at the mechanisms of the OH chemistry. The chemistry is dominated by OH chemistry, with little information given on the NOx and NOy composition in the mini-chamber (only estimated from stack measurements) and any photolysis chemistry of photo-labile species is occurring at non-atmospherically relevant wavelengths.

   We thank the reviewer for this comment. Before addressing each point specifically, we wish to direct the reviewer to our summary of revisions. In this updated manuscript, we explicitly outline the scope of the mini chamber modeling (i.e., identifying the secondary NMOG detected by PTR-ToF-MS and I-CIMS) and provide more details about the estimations of photolysis frequencies. In our previous draft, we discussed the uncertainties associated with mini chamber UVC lights, and we quantified the extent to which non-OH losses were responsible for the evolution of primary and secondary NMOG (Sections 3.2.2). We also compared the chemistry of the mini chamber with that expected for an ambient biomass burning plume in order to benchmark mini chamber observations (Section 3.2.3).

Smoke was diluted with humid air (RH = 30%) and mixed with 70 ppb of ozone in order to simulate 1 -5 days of atmospheric oxidation over the course of 40 minutes. We have added text to note this explicitly in Section 2.2

NOx and NOy measurements were not available in the mini chamber. Our previous draft discusses our estimations of NO, NO2, and HONO initial conditions at lines 196-197. We have moved this up to Section 2.2 for clarity.

2) There is little information given on the chamber auxiliary chemistry mechanism needed in order to the background reactivity of the chamber in the chamber specific box modelling. For example, processes that need to be taken into account include: introduction of free radicals from heterogeneous chamber wall reactions; adsorption/desorption of NOy species (including HONO) to/from the chamber walls; off-gassing of various reactive species from the chamber walls, which can contribute significantly to the radical budget of the system. Also, initial HONO concentration is important to know. Is a detailed chamber auxiliary mechanism available and used here? Formic and acetic acid are shown to be significant secondary product VOCs in the experiments (Line 288).These small oxygenates, as well as HCHO and HONO have significant wall sources in Teflon chambers. Have these sources been taken into account? (in the chamber auxiliary mechanism).

As mentioned in our summary of revisions, our intention in modeling the mini chamber is to understand the identities and processes contributing to the formation of NMOG measured by PTR-ToF-MS and I-CIMS. Therefore, we focus strictly on gas-phase oxidation processes leading to the formation of maleic anhydride and hydroxy furanones (i.e., furan oxidation). We agree that chamber surfaces could affect our measurements through gas-wall partitioning; however, the OH environment in the chamber is overwhelmingly controlled by ozone photolysis. Likewise, an auxiliary mechanism would be complicated by the mini chamber operation since the Teflon bag is continuously diluted with clean, humid air. Biomass burning emissions are notoriously semi-volatile (Bian et al. 2015, Hodshire et al. 2019), and accounting for wall-vapor interactions would be a modeling effort in itself and would mostly be useful for understanding SOA formation. Despite this impact, Lim et al. (2019) show that the primary VOCs measured in the mini chamber did not exhibit significant wall losses prior to photochemistry.

We agree with the reviewer that it is important to note that we are not considering these processes in the model, and have noted this in Section 2.4.

3) It is stated at line 238/239 that “radical reactions and NOx loss process are likely sensitive to initial NO/NO2 ratios”, have any model sensitivity analyses been done to look at this sensitivity?

We have varied the NO/NO2 ratio - changes in this ratio do not impact OH concentrations, and any NO is quickly converted to NO2 within seconds of initiating the model. The larger effect is mostly in estimating absolute NO concentrations, which impacts the initial RO2 pathways shortly after initiating the model. Higher NO leads to greater RO2 + NO, which can lead to sharp increases in first-generation NMOG, which are not observed in I-CIMS data. Since we do not have NOx measurements, our best assumption of the NO/NO2 ratio is based on modeling the evolution of NO + NO2 in the mini chamber, prior to photochemistry. Within the stated distribution (> 95% NO2), we do not see significant impacts on mini chamber results.

4) More chamber details are needed – mixing time, spectrum of the lamp used and how was the photon flux derived; how uniform throughout the chamber is the photon flux exposure?

   The mixing processes are captured by the evolution of acetonitrile, which is represented in the modeling. We also discuss the mixing procedure in Section 2.2. The UVC lights emit at a narrow wavelength at 254 nm (line 106). We cannot comment on the uniformity of the photon flux exposure; however, the Teflon chamber was enclosed in a reflective box. Therefore, we can only assume a uniform photon distribution.

5) As the other reviewer points out, information on the photolysis rates of some of the primary photo-labile VOCs, along with rate constants for other atmospherically important oxidants are given in the SI. However, little to no information has been given as to the sources of these important data are given. Also, how were the photolysis rates calculated? It is important to note that the MCM chemical mechanisms are designed for use in tropospheric chemistry models, where the cross-sections and quantum yield data used to derive the photolysis rates are mainly used at > 290 nm. Therefore, any primary and secondary MCM chemistry used here in the chamber modelling (but not in the BB plume models) needs to be adjusted to photolysis < 290 nm (mainly around254 nm). For example, the 1,4-dicarbonyl chemistry (mainly 2-butenedial and 4-oxo-2-pentenal, which are significant products from the atmospheric chemistry of aromatics and furans) in the MCM is mainly driven by photolysis (see Newland et al., 2019),where the main photolysis products are furanones and maleic anhydride (a main focus of this study). However, at 254 nm, the photolysis product distribution (quantum yields and photo-tautomer distributions) are different (Tang and Zhu 2005).

   We appreciate the reviewers careful critique of our discussion about photolysis. We refer the reviewer to our summary of revisions. We have included new tables into the SI that describe our assumptions about the photolysis frequencies used for mini chamber modeling.

We note that our mechanism development is limited towards including reactions relevant to ambient biomass burning plumes since our intention is to use this mechanism to understand ozone and secondary NMOG formation in ambient smoke (Section 3.2.4). We do appreciate that some of the important intermediates (e.g. butenedial) could have different photolysis pathways at 254 nm. However, when we estimate the photolysis frequency of butenedial at 254 nm (which we note is not well studied; the cross sections dramatically decrease between 230 - 260 nm and previous studies have investigated absorption at these wavelengths with limited resolution), we find that photolysis only contributes ~ 5% to the total loss of butenedial. In the mini chamber, OH concentrations are greatly elevated and OH + butenedial is the predominant loss pathway.

6) I agree with the other referee that given that a) monoterpenes contribute significantly to the calculated OH reactivity on the experiments and b) the MCM contains extensive chemical mechanism for the atmospheric degradation of both alpha and beta pinene,as well as limonene (and beta caryophellene), using a-pinene as a proxy is an over-simplification here (Line 394).

   We agree with both reviewers and have separated PTR-ToF-MS measurements to alpha pinene, beta pinene, and limonene to account for differences in reactivity associated with endocyclic and exocyclic double bonds. Please see comment (5) in our response to Reviewer 1, and also new text in Section 3.2.1.

7) Line 80 – define “0-D”

   We removed “0-D” since “box model” is descriptive enough.

8) Line 105 – define “semi-batch”

   We have removed “semi-batch” as a descriptor since we provide details for chamber operation.

9) Line 275 – why is an OH atmospheric concentration of 1.5E+6 cm-3 assumed?

   This atmospheric concentration is commonly used in OFR studies (Peng 2016, 2018).

10) Line 353 – “I-ToF-MS” should be I-CIMS?

   We have corrected I-ToF

11) Line484 – reference needed for the o-semiquinone chemistry

   We have included a reference to Finewax et al., 2018.

12) Line 501 – is this exhibiting a “bi-exponential” decay profile?

It is not clear to what degree this is exhibiting a bi-exponential decay. We argue that there is likely formation of a secondary species that is isomeric with furfural (Lines 505-510).

13) Line 515 – could the model be underpredicting the MA yield owing to increased MA and furanone yields from 1,4-dicarbonyl photolysis at 254 nm?

This is certainly possible; however, it seems unlikely because 1,4-dicarbonyl formation is not immediate, as is MA formation at the beginning of the experiment. We also note that the modeled losses of 1,4-dicarbonyls seem to be mostly due to OH rather than photolysis (see comment 5).

14) Line 537 and Figure 2 – under-prediction of small oxygenates – some of this could be coming from wall sources? (e.g. Zador et al., 2005)

We think that is also very likely. We lump wall sources into the “heterogeneous” processes. We’ve clarified that this could be aerosol or wall heterogeneous chemistry.

15) Line 560 – ozonolysis of other monoterpenes than a-pinene could be more important?

We have updated the model to include a more detailed speciation of monoterpenes (see comment 6). Most of the monoterpenes are still represented by alpha-pinene, and the fate by ozonolysis remains ~1%. We have updated the text to indicate that we are discussing the sum of monoterpenes.

16) Line 718 – “understudied NMOG OH chemistry” – this study really focuses on the OH chemistry

Thank you for catching this - we’ve qualified that this is OH chemistry.

17) Line 721 – what does “understory” mean?

Understory refers to a burn where smaller biomass beneath the canopy are burned (e.g. twigs, leaves, needles, etc).

18) Figure S6, S7 and S9 – J<41> (CH3OOH photolysis rate) – has this been adapted for 254 nm photolysis?

J<41> has been adapted for 254 nm photolysis (now clarified in text, and in Table S1).

19) Figure S10 – what is GUAIACOLPROD?

GUAIACOLPROD is a generic, non-reactive product that is included to account for the fraction of guaiacol that does not react to form nitroguaiacols. We note this now in the figure caption.

20) Figure S14 – give structure of HYDMEFURANO2 on plot.

Thank you for the suggestion - we have added HYDMEFURANO2 and HYDFURANO2 structures to the plot.

Reviewer 3 Comments

This paper provides some important insights into emissions from biomass burning. Biomaterial was burned and chemical measurements of the resulting emissions. The MCM chemical mechanism was used in simulations of the experiments. The authors added more chemical reactions to the MCM to improve its performance in simulating the experiments.

Much more data like this is needed for the continuing development chemical mechanisms for atmospheric chemistry modeling. Also the authors have used some quantum chemistry in the further development of the test reactions that were added to the MCM. Finally, they considered real biomass burning plumes.

All in all, this paper represents a good mix of laboratory measurements, mechanism development with evaluation and applications to the real world. It is an excellent template for future studies.

Minor: Lines 210 - 215 I commend the authors for using the correct term, photolysis frequencies in this section. However, they need to be consistent and state at the beginning: "Photolysis frequencies are calculated using literature cross-sections and quantum yields of relevant organic and inorganic species..."

We thank Dr. Stockwell for his kind words. We have corrected the terminology here, and at other points in the manuscript.

References

Hodshire, A. L., Bian, Q., Ramnarine, E., Lonsdale, C. R., Alvarado, M. J., Kreidenweis, S. M., et al. (2019). More than emissions and chemistry: Fire size, dilution, and background aerosol also greatly influence near-field biomass burning aerosol aging. *Journal of Geophysical Research: Atmospheres*, 124, 5589– 5611.

Bian, Q., May, A. A., Kreidenweis, S. M., Pierce, J. R. (2015). Investigation of particle and vapor wall-loss effects on controlled wood-smoke smog-chamber experiments, *Atmos. Chem. Phys.*, 15, 11027-11045.

Geron, C., Rasmussen, R., Arnts, RR, & Guenther, A. (2000). A review and synthesis of monoterpene speciation from forests in the United States. *Atmos. Env*, 34(11), 1761-1781.

Lim, C. Y., Hagan, D. H., Coggon, M. M., Koss, A. R., Sekimoto, K., de Gouw, J., Warneke, C., Cappa, C. D., and Kroll, J. H.: Secondary organic aerosol formation from the laboratory oxidation of biomass burning emissions, Atmos. Chem. Phys., 19, 12797–12809, https://doi.org/10.5194/acp-19-12797-2019, 2019.

OH-chemistry of non-methane organic gases (NMOG) emitted from laboratory and ambient biomass burning smoke: evaluating the influence of furans and oxygenated aromatics on ozone and secondary NMOG formation.

Matthew M. Coggon[1,2], Christopher Y. Lim[3], Abigail R. Koss[1,2,‡], Kanako Sekimoto[1,2,4], Bin Yuan[1,2,†], Jessica B Gilman[2], David H. Hagan[3], Vanessa Selimovic[5], Kyle J. Zarzana[1,2,§], Steven S. Brown[2], James M. Roberts[2], Markus Müller[6], Robert Yokelson[5], Armin Wisthaler[7,8], Jordan E. Krechmer[9], Jose L. Jimenez[1,10], Christopher Cappa[11], Jesse H. Kroll[3], Joost de Gouw[1,10], and Carsten Warneke[1,2]

[1]Cooperative Institute for Research in Environmental Sciences, University of Colorado, Boulder, CO, USA
[2]NOAA Earth Systems Research Laboratory Chemical Sciences Division, Boulder, CO, USA
[3]Department of Civil and Environmental Engineering, Massachusetts Institute of Technology, Cambridge, MA, USA
[4]Graduate School of Nanobioscience, Yokohama City University, Yokohama, Kanagawa, Japan
[5]Department of Chemistry and Biochemistry, University of Montana, Missoula, MT, USA
[6]Ionicon Analytik, Innsbruck, Austria
[7]Institute for Ion Physics and Applied Physics, University of Innsbruck, Innsbruck , Austria
[8]Department of Chemistry, University of Oslo, Oslo, Norway
[9]Aerodyne Research, Inc., Billerica, MA, USA
[10]Department of Chemistry, University of Colorado, Boulder, CO, USA
[11]Department of Civil and Environmental Engineering, University of California, Davis, CA, USA
[‡]now Tofwerk A.G., Boulder, CO, USA
[†]now at Institute for Environment and Climate Research, Jinan University, Guangzhou, China.
[§]now at Department of Chemistry, University of Colorado Boulder, Boulder, CO, USA

Correspondence: Matthew Coggon (matthew.m.coggon@noaa.gov), Carsten Warneke (carsten.warneke@noaa.gov)

Abstract.

Chamber oxidation experiments conducted at the Fire Sciences Laboratory in 2016 are evaluated to identify important chemical processes contributing to the OH chemistry of biomass burning non-methane organic gases (NMOG). Based on the decay of primary carbon measured by proton transfer reaction time-of-flight mass spectrometry (PTR-ToF-MS), it is confirmed that furans and oxygenated aromatics are among the NMOG emitted from western United States fuel types with the highest reactivities towards OH. The oxidation processes and formation of secondary NMOG masses measured by PTR-ToF-MS and iodide clustering time-of-flight chemical ionization mass spectrometry (I-CIMS) is interpreted using a box model employing a modified version of the Master Chemical Mechanism (v. 3.3.1) that includes the OH oxidation of furan, 2-methylfuran, 2,5-dimethylfuran, furfural, 5-methylfurfural, and guaiacol. The model supports the assignment of major PTR-ToF-MS and I-CIMS signals to a series of anhydrides and hydroxy furanones formed primarily through furan chemistry. This mechanism is applied to a Lagrangian box model used previously to model a real biomass burning plume. The customized mechanism reproduces the decay of furans and oxygenated aromatics and the formation of secondary NMOG, such as maleic anhydride.

Based on model simulations conducted with and without furans, it is estimated that furans contributed up to 10% of ozone and over 90% of maleic anhydride formed within the first 4 hours of oxidation. It is shown that maleic anhydride is present in a biomass burning plume transported over several days, which demonstrates the utility of anhydrides as markers for aged biomass burning plumes.

1 Introduction

Biomass burning is a significant source of atmospheric non-methane organic gases (NMOG). Once emitted, biomass burning NMOG may undergo photochemical reactions to form ozone and secondary organic aerosol (SOA) (Hobbs et al., 2003; Yokelson et al., 2009; Akagi et al., 2013). Wildfire smoke is believed to significantly contribute to summer-time ozone levels in fire-prone regions, such as the western United States (Jaffe et al., 2008, 2013, 2018). An assessment of historical ozone data from 1989 - 2004 has shown that daily mean ozone increases by 2 ppb for every 1 million acres of area burned (Jaffe et al., 2008). A warming, drier climate is likely to increase fire activity, which may lead to increased ozone and PM2.5 levels in susceptible regions (Westerling, 2006; Jaffe and Wigder, 2012; Brey and Fischer, 2016; Ford et al., 2018).

Despite its importance, the atmospheric chemistry of biomass burning smoke remains poorly-understood due to the complexity of smoke processing. Field observations have shown that ozone enhancement ratios ($\Delta O_3/\Delta CO$) may increase (e.g. 0.7 ppb/ppb, Andreae et al., 1988; Mauzerall et al., 1998), decrease (e.g. -0.07 ppb/ppb, Alvarado et al., 2010), or remain unchanged downwind of wildfires (Jaffe and Wigder, 2012). The extent of ozone production depends on multiple factors, including NMOG/NO_x ratios, downwind meteorology, and incident solar radiation (Akagi et al., 2013; Jaffe et al., 2018). Ozone production may also be slowed through peroxyacetyl nitrate formation (PAN), which is affected, in part, by NMOG functionality and total NO_x and NMOG emissions (Alvarado et al., 2010; Liu et al., 2016; Müller et al., 2016; Jaffe et al., 2018). Biomass burning emissions are produced by distillation and pyrolysis, as well as glowing and flaming combustion (Yokelson et al., 1996). Primary NMOG speciation is largely driven by pyrolysis temperatures and fuel composition (e.g., Sekimoto et al., 2018; Hatch et al., 2015), whereas NO_x emissions generally increase with increased flaming combustion and greater fuel nitrogen content (Burling et al., 2010).

Secondary NMOG may provide insights into the chemical processes that contribute to smoke oxidation. Several studies have identified important secondary NMOG formed from aging of biomass burning emissions (Yokelson et al., 2003; Müller et al., 2016; Bruns et al., 2017; Hartikainen et al., 2018); however, the mechanisms that lead to secondary NMOG formation remain unclear. For example, maleic anhydride has been identified as a significant secondary NMOG formed in smoke within hours of oxidation (Müller et al., 2016; Bruns et al., 2017; Hartikainen et al., 2018). Maleic anhydride is a known product of aromatic oxidation, but it also an end product of furan chemistry (Bierbach et al., 1995; Aschmann et al., 2011, 2014). Understanding the pathways leading to secondary NMOG formation may be useful in constraining smoke properties (e.g. plume age), or identifying significant ozone and SOA precursors.

Few studies have modeled the detailed chemical mechanisms leading to secondary NMOG formation (Mason et al., 2001; Alvarado et al., 2015; Müller et al., 2016; Liu et al., 2016). This work is challenging because a large fraction (22 - 56%)

of the identified reactive carbon is associated with compounds whose OH chemistry is unknown or has not been specified in atmospheric chemistry mechanisms (Hatch et al., 2017). These species could significantly contribute to ozone or SOA formation. For example, Alvarado et al. (2015) modeled the evolution of ozone and SOA formed downwind of a prescribed fire and found that O_3 production was strongly sensitive to the inclusion of unknown NMOG having OH rate constants of $\sim 10^{-11}$ $cm^3 molec^{-1} s^{-1}$. Müller et al. (2016) explicitly modeled the oxidation of 16 NMOG emitted from a small understory fire using the Master Chemical Mechanism (MCM v. 3.3.1, Jenkin et al., 1997, 2003, 2015; Saunders et al., 2003). The model captured the loss of important reactive primary NMOG and reproduced the formation of O_3 and PAN. The formation of maleic anhydride could not be explained by the model, which reflects the need for additional mechanism development.

The studies described above demonstrate that highly reactive organic compounds play an important role in the OH oxidation of young biomass burning plumes. Laboratory studies evaluating the reactivity of biomass burning NMOG have shown that furans, oxygenated aromatics, and aliphatic hydrocarbons (e.g. monoterpenes and cyclopentadiene) are major contributors to calculated or measured OH reactivity (Stockwell et al., 2015; Gilman et al., 2015; Hatch et al., 2015; Bruns et al., 2017; Hartikainen et al., 2018). Hartikainen et al. (2018), for example, found that furans and phenolic compounds were among the most reactive NMOG emitted from logwood emissions. The detailed chemical mechanisms of these compounds have been studied in single-component systems (Bierbach et al., 1995; Alvarez et al., 2009; Aschmann et al., 2011, 2014; Zhao and Wang, 2017; Yee et al., 2013; Lauraguais et al., 2014; Finewax et al., 2018); however, these mechanisms have not been widely implemented into models of biomass burning smoke. Müller et al. (2016) included simple mechanisms for furan and furfural; however, other major furan species, such as 2-methylfuran, 2,5-dimethylfuran, and 5-methylfurfural, were omitted.

A few studies have evaluated biomass burning OH oxidation using proton-transfer-reaction time-of-flight mass spectrometry (PTR-ToF-MS). PTR-ToF-MS is capable of measuring 50-80% of the primary NMOG mass emitted from biomass burning, including oxygenates, aromatics, and heterocyclic compounds (Hatch et al., 2017). The remaining mass includes compounds that are that are difficult to quantify by proton transfer, such as alkanes and small alkenes. The PTR-ToF-MS is effective in monitoring the evolution of some secondary NMOG, such as maleic anhydride (Müller et al., 2016). Nonetheless, limitations on isomeric specificity (Hatch et al., 2017), fragmentation, and sensitivity may hinder the ability of the PTR-ToF-MS to measure other secondary oxygenates or multi-functionalized organics (Yuan et al., 2017). The iodide clustering time-of-flight chemical ionization mass spectrometer (I^--ToF-CIMS, herinafter I-CIMS for brevity) is well-suited to measure oxygenated NMOG. The I-CIMS is sensitive to acids and multi-functional oxygenates (Lee et al., 2014), which are likely to form as secondary NMOG in biomass burning plumes. I-CIMS has been used to evaluate primary NMOG emissions (e.g., Priestley et al., 2018; Reyes-Villegas et al., 2018; Tomaz et al., 2018), biomass burning emissions aged by nocturnal processes (Ahern et al., 2018; Reyes-Villegas et al., 2018), and primary particle-phase components (Gaston et al., 2016). I-CIMS spectra of the NMOG resulting from the OH oxidation of biomass burning smoke have yet to be reported.

Presented here are PTR-ToF-MS and I-CIMS measurements from chamber experiments conducted during the 2016 laboratory component of the Fire Influence on Regional to Global Environments and Air Quality Experiment (FIREX-AQ) conducted at the Fires Sciences Laboratory in Missoula, MT. Based on these data, modifications are made to the MCM (v.3.3.1) to include the reactions of highly reactive NMOG, including furan, furfural, 2-methylfuran, 2,5-dimethylfuran, 5-methylfurfural,

and guaiacol. This mechanism is applied to a box model to interpret observed increases in secondary NMOG measured by the PTR-ToF-MS and I-CIMS. The chemical mechanism is also applied to a Lagrangian model previously used to evaluate the OH chemistry of an ambient biomass burning plume (Müller et al., 2016). The model output is compared to measured secondary NMOG and O_3 production to evaluate the influence of furans and oxygenated aromatics on the chemistry of a real biomass burning plume.

2 Methods

2.1 Campaign description

The laboratory component of the FIREX-AQ intensive was conducted at the U.S. Forest Service Fire Sciences Laboratory in Missoula, MT during October - November 2016. The purpose of this study was to simulate the emissions and atmospheric oxidation of biomass burning smoke resulting from the combustion of western U.S. fuels. A full description of the campaign, experimental setup, types of fuels burned, and resulting emissions of key NMOG is provided elsewhere (Selimovic et al., 2018; Koss et al., 2018).

Burn experiments were conducted in a large, indoor combustion room as described by Selimovic et al. (2018). Inside the room, fuels were assembled on a bed centered below a 20 m (L) $\times$ 1.6 m (ID) exhaust stack. The fuels were ignited by a heating plate, and the resulting smoke was vented through the stack at a constant velocity of $\sim$ 3 m s^{-1}. Smoke was sampled by instrumentation on a platform located $\sim$17 m above of the fuel bed or directed to other areas of the laboratory through tubing and ductwork.

The fuels were chosen to represent ecosystems prone to wildfires in the western U.S and included components (i.e, leaves, stems, trunks, and duff) of the following species: ponderosa pine (*Pinus ponderosa*), lodegepole pine (*Pinus contorta*), Engelmann spruce (*Picea engelmanii*), Douglas fir (*Pseudotsuga menziesii*), subalpine fir (*Abies lasiocarpa*), manzanita (*Arctostaphylos*) and chamise (*Adenostoma fasciculatum*). The components of each fuel type were burned individually and in mixtures designed to mimic a real forested ecosystem. A full description of these fuels, including harvesting location, composition, and dry weight are provided elsewhere (Selimovic et al., 2018).

2.2 Chamber OH Oxidation Experiments

Oxidation experiments were performed using an OH-oxidation chamber. The apparatus, subsequently referred to as the "mini chamber", consists of a 150 L Teflon bag centrally located between two UVC lamps (narrow peak emission 254 nm, Ultra-Violet Products, Inc.). A full description of the instrumentation and operation of the mini chamber is provided by Lim et al. (2019). OH is produced by the photolysis of ozone in the presence of water according to reactions R1 – R2.

$$O_3 + h\nu \rightarrow O^1D \quad \text{(R1)}$$

$$O^1D + H_2O \rightarrow 2OH \quad \text{(R2)}$$

Other sources of OH, such as HONO and aldehydes, were also introduced into the chamber via injection of biomass burning smoke. The relative humidity and ozone mixing ratios in the mini chamber were adjusted to maintain OH exposures equivalent to 1 - 5 days of atmospheric oxidation. The UVC lamps initiated photochemistry, and the photon flux at the center of the chamber was measured to be $\sim 3\times10^{15}$ photons cm^{-2} s^{-1} using a photodiode sensor (Thorlabs S120VC). Previous studies using oxidation flow reactors have investigated the radical chemistry under 254 nm irradiation to quantify non-OH losses and RO_2 pathways (Peng et al., 2016; Peng and Jimenez, 2017; Peng et al., 2019). For most primary NMOG, losses were dominated by OH oxidation. For some species, photolysis played a significant role. Non-OH loss processes affecting important NMOG are discussed in Section 3.2.3.

A suite of particle and gas-phase instruments sampled from the bag through stainless-steel and Teflon tubing, respectively. This study focuses on NMOG measurements (described in Section 2.3.1), but a complete description of aerosol measurements is provided by Lim et al. (2019). NO_x and NO_y were not measured from the mini chamber. Initial NO_x mixing ratios are estimated based on the integrated NO_x/acetonitrile ratios measured from the stack during mini chamber filling. HONO, an important source of NO_x and OH, is estimated similarly.

The mini chamber was located in a room $\sim$ 30 m from the top of the stack. To quickly deliver smoke to the chamber, stack air was drawn through a 30 m L $\times$ 20 cm D aluminum duct. The residence time within the duct was $<$ 2 s and particle losses were minor (Lim et al., 2019). Gas-phase species have a high affinity to metal surfaces and losses to the aluminum ductwork are possible (Deming et al., 2019). It is difficult to assess these losses quantitatively; however, the average NMOG/acetonitrile ratio measured in the mini chamber was $\sim$ 15 – 20 % lower than that measured from the stack (see Supplemental Information for more details). While these differences likely indicate that NMOG were lost to ductwork, the relative distribution of NMOG was not significantly different between the stack and mini chamber.

Mini chamber experiments were conducted in the following manner: (1) Prior to each burn, the bag was flushed with clean humidified air for $\sim$ 45 min. (2) Immediately following fuel ignition, smoke diluted with clean air was injected into the bag at a $\sim$ 1:10 ratio. Injection proceeded until the burn finished, or until particle concentrations maximized inside the mini chamber. For most experiments, the distribution of NMOG and particles represented an integrated sample of all phases of the burn. (3) 40 ppb of deuterated butanol (butanol-d9, added to monitor OH exposure) was injected into the chamber and the particle and gas mixture was allowed to mix for $\sim$ 5-10 min. (4) A stream of clean, humidified air (RH $\sim$ 30 %) doped with $\sim$ 70 ppb ozone was continuously added to the mini chamber to match instrumentation sampling flows ($\sim$ 6 L min^{-1}) and maintain a high-OH environment. (5) Once aerosol and gas-phase concentrations stabilized, the UVC lamps were turned on and photochemistry proceeded for $\sim$ 30-45 min. (6) At the end of the experiment, the bag was flushed with clean dilution air in preparation for subsequent experiments.

Gas and particle-phase concentrations were corrected for dilution by monitoring the decay of acetonitrile, which is present at high concentrations in biomass burning smoke, is slow to react with OH (lifetime $\sim$335 d at OH = 1.5×10^6 molec cm^{-3}),

and is not significantly lost to Teflon surfaces (Krechmer et al., 2016; Pagonis et al., 2017). CO was not used as a dilution tracer due to observed CO production following the initiation of photochemistry. The dilution rate estimated by acetonitrile decay agreed well with flow rate calculations (Lim et al., 2019). OH exposures in the mini chamber were estimated based on the dilution-corrected loss of butanol-d9 (k_{OH} = 3.4×10^{-12} cm^3 $molec^{-1}$ s^{-1}, Barmet et al., 2012).

2.3 Instrumentation

2.3.1 NMOG Measurements

NMOG measurements were conducted using a high-resolution proton transfer reaction time-of-flight mass spectrometer (PTR-ToF-MS, Yuan et al., 2016) and an iodide clustering time-of-flight chemical ionization mass spectrometer (I-CIMS, Aerodyne/Tofwerk, AG). The instruments were deployed to measure primary smoke emissions from the stack and room, as well as aged emissions from the mini chamber. During a burn (and while the mini chamber was filling with smoke), both instruments sampled from the stack to characterize primary NMOG emissions. At the end of a burn, the sampling lines were switched and the instruments sampled from the mini chamber through a 10 m long x 3 mm OD PFA inlet at a total flow rate of $\sim$ 3 L min^{-1}. A full description of the primary NMOG measurements is provided elsewhere and only a brief description of these measurements are provided here (Koss et al., 2018).

The PTR-ToF-MS measured at 1 Hz to capture the decay of primary NMOG and formation of secondary species, respectively. The drift tube was operated with an electric field to number density ratio (*E/N*) of 120 Td, and the high-resolution mass spectrometer (max resolution $\sim$ 4500) scanned ions with *m/z* 12 - 500 Th. The mass spectrometer resolves the molecular formulae of isobaric species, but cannot distinguish isomers. This presents challenges in reacting systems as secondary NMOG formed by OH oxidation could have the same molecular formula as primary NMOG. Koss et al. (2018) identified the distribution of primary NMOG during FIREX-AQ using gas chromatography pre-separation to measure isomer contributions. For most fuel types, over 90% of the PTR-ToF-MS signal could be assigned. The primary groups detected by PTR-ToF-MS were small oxygenates ($\sim$ 50% v/v, dominated by acetic acid, formaldehyde, methanol, and acetaldehyde), aromatics ($\sim$ 10%, dominated by catechol, phenol, methoxy phenols, benzene, and toluene), furans ($\sim$ 10%, dominated by 5-methylfurfural, 2-furfural, furanone, furan, and methyl + dimethyl furans) and a broad range of hydrocarbons ($\sim$ 15%, dominated by ethene, propene, butene, and 1,3-butadiene). The same NMOG assignments and sensitivities are applied here to masses observed to be enhanced prior to NMOG oxidation. The temporal profile of some larger primary oxygenates ($C > 5$) were also influenced by the formation of secondary isomers or unidentified primary species (see Section 3.2.2). Calibration factors for primary species are calculated from measured or estimated proton-transfer rate constants (uncertainty $<$ 50%, Sekimoto et al., 2017).

Masses detected after the initiation of photochemistry are assigned based on previous literature observations and modeling evidence (see Section 3.2.2). A number of laboratory and field studies employing PTR-ToF-MS and OP-FTIR have observed formation of formic acid ($CH_2O_2{-}H^+$, *m/z* 47), acetic acid ($C_2H_4O_2{-}H^+$, *m/z* 61), maleic anhydride ($C_4H_2O_3{-}H^+$, *m/z* 99), and phthalic anhydride ($C_8H_4O_4{-}H^+$, *m/z* 149) in aged smoke (Yokelson et al., 2003, 2009; Akagi et al., 2012; Müller et al., 2016; Bruns et al., 2017; Hartikainen et al., 2018). Calibration factors for these species are calculated from measured

or estimated proton-transfer rate constants. In this study, substantial increases in $C_4H_4O_3{-}H^+$ (*m/z* 101) and $C_4H_8O_2{-}H^+$ (*m/z* 89) are also observed. $C_4H_4O_3{-}H^+$ could be 5-hydroxy-2(5H)-furanone (or simply hydroxy furanone), its tautomer malealdehydic acid, or succinic anhydride, whereas $C_4H_8O_2{-}H^+$ is likely a C_4 hydroxy carbonyl (see Sections 3.1 and) Liu et al., 1999; Bierbach et al., 1994, 1995; Alvarez et al., 2009; Aschmann et al., 2011, 2014; Strollo and Ziemann, 2013; Zhao and Wang, 2017). Due to uncertainties in these assignments, calibration factors for these species are calculated using estimated proton-transfer rate constants derived from molecular formula relationships (uncertainty to within a factor of 2, Sekimoto et al., 2017).

The I-CIMS utilizes a "soft" chemical ionization source that forms iodide clusters with polarizable analyte molecules (Huey et al., 1995; Lee et al., 2014). The instrument used here was operated in a similar configuration to that described in Krechmer et al. (2016). To generate reagent ions, 2 SLPM of clean N_2 from dewar blow-off was run over a methyl iodide permeation tube and ionized using a Polonium-210 ionizer and into an ion molecule reaction region (IMR). The I-CIMS measured gas-phase signals from the mini chamber at 1 Hz time resolution. Smoke was diluted with 4 L min^{-1} of clean, humidified air at a 4:1 ratio to minimize reagent ion depletion. A constant flow of isotopically labeled formic acid was delivered to the instrument to measure consistency of response. Reported here are I-CIMS measurements normalized to $1{\times}10^6$ counts per second of the reagent ion signal at m/z 126.905 (normalized counts per second, ncps). Due to unavailability of standards, I-CIMS data are not reported in mixing ratios. Secondary NMOG measured by I-CIMS are assigned identifications based on modeling results and previous literature.

2.3.2 NO_x Measurements

NO, NO_2, and HONO were measured by an open-path Fourier transform infrared spectrometer (OP-FTIR) as described by Selimovic et al. (2018). The OP-FTIR was located on the platform and sampled smoke across the diameter of the stack. The OP-FTIR provides fast measurements and avoids potential sampling artifacts due to sample line losses. OP-FTIR measurements were used for most experiments. NO_2 and HONO were also measured by the NOAA Airborne Cavity Enhanced Spectrometer (ACES) as described by Zarzana et al. (2018). ACES was located on the platform and sampled smoke through a 1 m Teflon inlet. These data were used when OP-FTIR data were unavailable, or when NO_x emissions were below OP-FTIR detection limits. Supplementary NO measurements were provided by a custom-built chemiluminescence instrument located in a room on the burn chamber floor. A full description of that instrument is provided by (Stockwell et al., 2018).

2.4 Box Model Implementation and Evaluation

NMOG oxidation processes were simulated using the Framework for 0-D Atmospheric Modeling (F0AM v 3.1, https://sites.google.com/site/wolfegm/models, Wolfe et al., 2016). A modified NMOG oxidation mechanism is applied based on the Master Chemical Mechanism (MCM v. 3.3.1, Jenkin et al., 1997, 2003, 2015; Saunders et al., 2003). As described below and in Section 3.2.1, the box model is used to evaluate NMOG formation in the mini chamber, as well a for the daytime oxidation of an ambient biomass burning plume (Müller et al., 2016). Non-atmospheric photolysis played a role in the evolution of organics in the mini chamber owing to the use of UVC lamps; consequently, interpretation of the mini chamber measurements is limited

to evaluating the link between OH oxidation of furan and oxygenated aromatics with the formation of several key secondary NMOG measured by I-CIMS and PTR-ToF-MS. The ambient model is used to quantitatively evaluate the impact of furan and oxygenated aromatic chemistry on secondary NMOG and ozone formation in real biomass burning plumes.

NMOG chemistry and dilution are assumed to follow the first-order differential equation described by Eqn 1.

$$\frac{dC_i}{dt} = \sum_{m}^{n} P_m r_m - \sum_{m}^{n} R_m r_m - k_i C_i \quad (1)$$

Where C_i is the concentration of species i, P_m is the stoichiometric coefficient of reaction m leading to the formation of species i, R_m is the stoichiometric coefficient of reaction m leading to the loss of species i, r is the elementary rate of reaction m, and k_i is a first-order dilution rate constant. A constant dilution term is applied to all species based on the measured loss rate of acetonitrile. Vapor-wall interactions are not considered in this model, and these processes may impact the evolution of intermediate and semi-volatile gases. Lim et al. (2019) did not observe significant wall losses of primary VOCs during chamber experiments. Vapor-wall interactions have been shown to play a role in the SOA evolution of biomass burning smoke, and partitioning to the gas-phase is greater in diluting systems (Bian et al., 2015; Hodshire et al., 2019).

The MCM treats the photolysis of organic and inorganic species through parameterizations relevant to atmospheric wavelengths. To account for photolysis in the mini chamber, MCM photolysis frequencies were calculated using literature cross-sections and quantum yields of relevant organic and inorganic species (Atkinson et al., 2006; Burkholder et al., 2015; Keller-Rudek et al., 2013). Tables S1 and S2 summarize the reactions and databases used to estimate photolysis frequencies in the mini chamber. For some primary species and NO_x reservoirs (e.g., acetone, acetaldehyde, benzaldehyde, PAN), additional reactions were added to account for photolysis pathways at 254 nm (Table S2).

Photolysis frequencies are calculated as the product of the absorption cross section, quantum yield, and photon flux at 254 nm. The measured 254 nm photon flux (3×10^{15} photons cm^{-2} s^{-1}) is scaled by a factor of 1.5 in order to reproduce the measured OH-loss of butanol-d9. No other changes are applied to the rate constants or reactions of MCM v. 3.3.1. To account for other reactive NMOG, literature mechanisms for furan, 2-methylfuran, 2,5-dimethylfuran, furfural, 5-methylfurfural, and guaiacol are included. A full description of these modifications are provided in Section 3.2.1. Table S3 summarizes the photolysis frequencies and OH, O_3, and NO_3 rate constants for the primary NMOG species modeled here.

The mini chamber model is evaluated against two fires - F26 (Engelmann spruce duff) and F38 (ponderosa pine litter). These two fires represent different extreme cases in NO_x and NMOG composition and were chosen in order to assess the extent to which the variability of primary NMOG influences secondary NMOG formation. Figure S2 illustrates how F38 and F26 compare to other fires measured in this study. F26 was a unique burn characterized by low-temperature smoldering combustion, which resulted in low NO_x emissions (NO_x/NMOG $\sim$ 0.02 mol/mol) and a NMOG profile with high contributions from oxygenated aromatics such as phenol, cresol, and guaiacol. F38 was representative of many of the burns presented here and was characterized by a mixture of high-temperature flaming combustion and low-temperature smoldering. NO_x emissions were substantially higher than those of F26 (NO_x/NMOG $\sim$ 0.32).

The mini chamber model is initialized with the concentration of 47 primary NMOG species measured by PTR-ToF-MS (Table S3). NO, NO_2, and HONO were initialized based on stack measurements as described in Section 2.3.2. Ozone measurements were conducted using a 2B Technologies ozone monitor (model 202), which exhibited significant interferences upon the addition of smoke or hexafluorobenzene (added as a supplemental dilution tracer). The monitor measures the absorption of O_3 at wavelengths that are also absorbed by many primary NMOG. Here, ozone measurements are only used to initialize the model with initial O_3 mixing ratios. These initial conditions are based on the signal measured prior to smoke injection and ranged between 5 - 10 ppb.

Ozone is continuously added to the chamber over the course of an experiment. This input of ozone is included in the model by applying a constant ozone concentration to the dilution term of Eqn. 1. It is estimated that the dilution stream contained $\sim$ 70 ppb of ozone based on the expected output from the ozone generator ($\sim$1 ppm) and the measured dilution rate. This input of ozone reproduces the ozone signal measured during dark control experiments to within 20% (Fig. S1).

NO and NO_2 are both emitted from fires. Once injected into the chamber, NO will react with O_3 to generate NO_2. In the atmosphere, NO and NO_2 will rapidly cycle owing to NO_2 photolysis. In the mini chamber, NO_2 photolysis is reduced since NO_2 does not strongly absorb at 254 nm (the absorption cross-section at 254 nm is a factor of 64 smaller than the peak absorption at 400 nm, Burkholder et al., 2015). Consequently, radical reactions (e.g., RO_2 + NO) and NO_x loss processes (e.g. PAN formation) are likely to be sensitive to the initial NO/NO_2 ratio. The initial NO/NO_2 ratio is estimated assuming that the NO_x mixture measured from the stack reacts with a constant mixing ratio of ozone (10 ppb) for 10 minutes (the approximate mixing periods for F26 and F38). This analysis yields a NO_x distribution that is $\geq$ 95% NO_2. This NO_x distribution is applied to the mini chamber model as an initial condition.

The ambient Lagrangian box model is the same used by Müller et al. (2016) to evaluate ozone and NMOG formation from aircraft measurements of a small biomass burning plume during the 2013 DISCOVER-AQ campaign. The mechanism employed by Müller et al. (2016) was based on MCM v 3.3.1 and included a simplified scheme to represent furfural and furan chemistry. Only the decay of furfural was modeled, whereas furan oxidation was assumed to form butenedial. The same model used by Müller et al. (2016) is employed here, except that the mechanism includes the reactions of furan, 2-methylfuran, 2,5-dimethylfuran, furfural, 5-methylfurfural, and guaiacol (Section 3.2.1). The same initial conditions used by Müller et al. (2016) are applied here, but with the inclusion of furan, 2-methylfuran, 2,5-dimethylfuran, furfural, 5-methylfurfural, and guaiacol, phenol, cresol, and catechol. Photolysis in the ambient box model is represented by MCM parameterizations, and dilution rates are calculated based on the observed decay of CO.

3 Results and Discussion

3.1 Oxidation Product Measurements

Figure S2 summarizes the initial NO_x and NMOG concentrations, NO_x/NMOG ratio, and NMOG composition for all the mini chamber experiments sampled by PTR-ToF-MS and I-CIMS. NMOG composition is reported as the fraction of NMOG signal attributed to high temperature, low temperature, and duff pyrolysis as described by Sekimoto et al. (2018). High temper-

ature pyrolysis results in higher emissions non-functionalized hydrocarbons, such as benzene, while low temperature pyrolysis results in higher emissions of oxygenated species, such as methoxy phenols. Duff pyrolysis generates a NMOG distribution that is similar to the distribution from low temperature pyrolysis, except that the unique composition of duff results in higher emissions of nitrogen-containing compounds.

The initial conditions for mini chamber experiments varied drastically depending on chamber dilution, fuel type, and burn conditions (Fig. S2). The NO_x/NMOG ratio varied over several orders of magnitude (0.01 – 1.2) with NMOG loadings ranging from 90 – 900 ppb. Fires produced varying distributions of NMOG owing to the extent of high and low temperature pyrolysis, while NO_x concentrations varied depending on fuel nitrogen content (Burling et al., 2010) and the extent of flaming combustion (Sekimoto et al., 2018). For the remaining discussion, only experiments with NMOG loadings < 300 ppb (12 total) are analyzed in order to evaluate biomass burning chemistry at the lowest calculated primary OH reactivities (OHR), since high OHR values can lead to significant OH suppression (Peng et al., 2016, 2019). The experiments reported here have estimated OHR between 18 - 70 s^{-1}, which are within range of the OHR recommended by Peng et al. (2016) when using 254 nm lights (50 – 100 s^{-1}).

Figure 1 shows the temporal evolution of select NMOG measured by PTR-ToF-MS and I-CIMS during F38 (Ponderosa Pine). The left column shows the decay of primary NMOG, while other columns show the temporal profiles of secondary NMOG exhibiting significant enhancements in PTR-ToF-MS and I-CIMS spectra. Secondary NMOG are classified based on temporal profile - those exhibiting a relatively fast increase in signal are classified as "fast-forming" products, while those formed more gradually over the course of an experiment are classified as "slow-forming" products. These designations are chosen based on the oxidation time scales that are likely to be observed in ambient biomass burning plumes. Here, OH exposures are estimated by the decay of butanol-d9, then converted to atmospheric-equivalent timescales assuming and atmospheric OH concentration of 1.5×10^6 molecules cm^{-3}. Fast-forming products generally peaked within 10-20 hrs of atmospheric-equivalent oxidation, while slow-forming products exhibited no maxima.

The loss of reactive primary species occurs quickly ($<$ 20 hrs of atmospheric-equivalent oxidation). Most species (e.g. dimethylfuran and guaiacol) follow an exponential decay consistent with radical loss pathways; however, some species, such as furfural and 5-methylfurfural, show faster decay immediately following the initiation of lights. The lights employed in these experiments (Ultra-Violet Products, Inc.) emit a narrow band at 254 nm, which is capable of photolyzing furanaldehydes and other absorbing species (Hiraoka and Srinivasan, 1968; Gandini et al., 1976). The furfural photolysis frequency in the mini chamber is estimated to be 0.13 s^{-1} (Table S2), which is orders of magnitude greater than the photolysis frequency expected under ambient, summer-time conditions (7.2×10^{-4} s^{-1}, Colmenar et al., 2015). Furfural photolysis leads to the formation of other highly reactive furans (e.g. furan) at modest yield (<0.3, Gandini et al., 1976)), and these products may contribute to the OH reactivity early on during each experiment.

The majority of secondary NMOG observed by the PTR-ToF-MS are formed slowly as "slow-forming" products. Previous studies employing PTR-ToF-MS have identified acetic acid, formic acid, and maleic anhydride as major products (Müller et al., 2016; Bruns et al., 2017; Hartikainen et al., 2018). Formic and acetic acid are primary species, but also form from OH oxidation of alkene and aromatic species (e.g., Jenkin et al., 1997, 2003, 2015; Saunders et al., 2003; Millet et al., 2015). Maleic anhydride is known to form from the oxidation of aromatics, but it has also been observed to form from the oxidation of furans

(Bierbach et al., 1995). The formation of slow-forming products occurs over timescales $>$ 20 hrs, which is significantly longer than the evolution of fast-forming (e.g. $C_5H_6O_3$, $\sim$ 4 hrs) and losses of the most reactive primary NMOG (e.g. 2-methylfuran and guaiacol, $\sim$ 4-10 hrs). This may be an indication of multi-generational oxidation, or early-generation formation via slowly-reacting primary species.

Figure 2 shows the resulting changes in NMOG composition measured by the PTR-ToF-MS after $\sim$ 12 hrs of atmospheric-equivalent oxidation. Data are shown in terms of primary carbon changes (Δ_CNMOG, %), which is the fraction of initial NMOG carbon measured by the PTR-ToF-MS that was consumed (reactant) or formed (product) for a given species or group of species. "Reactant" and "product" classifications were determined based on whether a detected mass exhibited an increase or decrease in dilution-corrected signal after 12 hours of atmospheric-equivalent oxidation. The bars in panel B represent species-aggregate measurements for each of the 12 fires highlighted in Fig. S2. Panel A shows an average of all secondary NMOG formed after 12 hrs of atmospheric-equivalent oxidation. Across most experiments, furans and oxygenated aromatics were the primary NMOG with the greatest carbon losses. Decreases in oxygenated aromatics were mostly driven by losses of guaiacol, methyl guaiacol, and catechol. Losses of furans were primarily due to decreases in furan, 2-methylfuran, 2,5-dimethylfuran, furfural, and 5-methylfurfural. These observations are consistent with previous PTR-ToF-MS measurements of aged wood burning smoke (Bruns et al., 2017; Hartikainen et al., 2018). The contribution from biogenic species in this study was variable, and largely dependent on composition (Hatch et al., 2015, 2017) and the extent to which monoterpenes were emitted from the distillation phase of combustion (Koss et al., 2018; Sekimoto et al., 2018). The detected masses associated with the alkene category exhibited both apparent formation and consumption across various experiments. Alkenes are expected to react quickly with OH; thus, observed increases likely point to a species misassignment. It is likely that this increase in signal is the result of PTR-ToF-MS fragmentation of oxygenated NMOG. For example, some alcohols, acids, and certain aldehydes may fragment in the PTR-ToF-MS to masses that are typically associated with alkenes (e.g. *m/z* 69, Buhr et al., 2002; Pagonis et al., 2019). These species are likely formed from the oxidation of biomass burning precursors and potentially interfere with alkene detection.

Across most experiments, small oxygenates and acids (C$<$5) were the predominant secondary NMOG detected by PTR-ToF-MS (Fig. 2B). As mentioned previously, formic acid, acetic acid, and maleic anhydride are several species with the largest relative increase at longer oxidation time scales (Fig. 2A); however, formaldehyde, acetaldehyde, acetone, and several $C_4O_xH_y$ species increased significantly. The formation of $C_4O_xH_y$ species follows a similar temporal pattern as maleic anhydride, which may point to similarities in species functionality or formation pathways.

In contrast to the PTR-ToF-MS measurements, the I-CIMS measured a mix of fast- and slow-forming products (Fig. 1). The I-CIMS measured a small fraction of the primary NMOG, so only secondary NMOG are discussed here. Fast-forming products included pyruvic acid ($C_3H_4O_3$), $C_xO_3H_y$ compounds, and masses likely corresponding to nitroaromatics. Previous studies have reported the formation of nitroaromatics from OH oxidation of catechol and guaiacol in the presence of NO_2 (Lauraguais et al., 2014; Finewax et al., 2018). $C_7H_7NO_4$ is consistent with the formation of nitroguaiacol, which has been observed in the gas and particle phase from guaiacol + OH (+NO_2) chemistry (Lauraguais et al., 2014). Finewax et al. (2018) studied the OH oxidation of catechol and observed the formation of nitrocatechol with a molar yield of 0.3. Very little nitrocatechol was

observed by the PTR-ToF-MS and I-CIMS, which is likely due to the high aerosol loadings in the chamber (> 50 μg m^{-3}) and high affinity of nitrocatechol to partition to aerosols and surfaces (Finewax et al., 2018).

Figure 3 summarizes the changes in I-CIMS product spectra relative to the total signal measured prior to photochemistry. Shown are the product distributions for short (4 hr), medium (12 hr), and longer (24 hr) atmospheric time scales. Because not all masses could be calibrated, normalized difference spectra (oxidized minus primary) are presented in order to illustrate the ions with the largest relative increases. In general, the secondary NMOG measured by I-CIMS tend to be multi-functional. The smallest observed oxygenate is formic acid (CH_2O_2), while larger molecules tend to be $C_{2-5}H_xO_3$ and $C_{4-5}H_xO_4$ compounds. After 4 hrs of oxidation, the largest enhancements are due to fast-forming products such as $C_3H_4O_3$, $C_4H_4O_3$, and $C_5H_6O_3$. The relative importance of these masses decreases at longer time scales, whereas the relative abundance of smaller oxygenates increases (e.g. CH_2O_2 and $C_2H_4O_3$).

The signal intensity of the fast-forming products (specifically $C_4H_4O_3$ and $C_5H_6O_3$) suggests that these species result from the oxidation of abundant, fast-reacting NMOG precursors with carbon number ≥ 4. Modeling results presented in Section 3.2 support the assignment of these products as hydroxy furanone ($C_4H_4O_3$) and methyl hydroxy furanone ($C_5H_6O_3$). Based on the loss of primary NMOG (Fig. 2), it is likely that these species are formed from the oxidation of furans, oxygenated aromatics, or other fast reacting NMOG with C$\geq$4. Several studies have investigated the oxidation of furan species and shown that hydroxy furanone + tautomer ($C_4H_4O_3$) and methyl hydroxy furanone + tautomer ($C_5H_6O_3$) are major products formed from the oxidation of furfural, furan, 2-methylfuran, and 2,5-dimethylfuran (e.g. Bierbach et al., 1994, 1995; Alvarez et al., 2009; Aschmann et al., 2011, 2014; Strollo and Ziemann, 2013; Zhao and Wang, 2017). Secondary NMOG measured from the OH chemistry of oxygenated aromatic species are largely carbon-retaining (C $\geq$ 6), though $C_4H_4O_4$ ring fragments have been measured in low-NO_2 catechol oxidation (Yee et al., 2013).

Notably, inspection of Figures 2A and 3 shows that there is little overlap in the species measured by PTR-ToF-MS and I-CIMS. The only masses that exhibit significant enhancements in both spectra are formic acid (CH_2O_2) and $C_4H_4O_3$. Moreover, there are significant differences in the temporal evolution of $C_4H_4O_3$. As discussed above, $C_4H_4O_3$ measured by I-CIMS most likely corresponds to hydroxy furanone, a fast-forming product (Fig. 1). In contrast, $C_4H_4O_3$ as measured by the PTR-ToF-MS exhibits a temporal profile resembling that of a slow-forming product. This mass is likely succinic anhydride, which is structurally similar to maleic anhydride and could be formed from multi-generation chemistry. The differences in these profiles suggests that the there are at least two different $C_4H_4O_3$ species present, that PTR-ToF-MS and I-CIMS are sensitive to different biomass burning oxidation products, and that both instruments are needed in order to measure important secondary NMOG.

Previous studies and the mass spectra in Figures 2 and 3 show that furan chemistry plays a significant role in the OH chemistry of biomass burning plumes (Bruns et al., 2017; Hartikainen et al., 2018; Gilman et al., 2015; Hatch et al., 2015). In Section 3.2, furan chemistry is incorporated into a box model to help interpret the observed small-chamber measurements and previously measured ambient biomass burning plumes.

3.2 NMOG Box Modeling

3.2.1 Mechanism Incorporation

The box model described in Section 2.4 employs NMOG chemistry based on the Master Chemical Mechanism (MCM v. 3.3.1, Jenkin et al., 1997, 2003, 2015; Saunders et al., 2003). The MCM explicitly represents the chemistry of biogenic, alkyl, aromatic, and oxygenated aromatic species. The laboratory measurements described in Section 3.1 demonstrate that heterocyclic hydrocarbons, such as the furans, could significantly contribute to secondary NMOG formation. The following discussion motivates and describes mechanism development aimed at expanding the MCM representation of biomass burning OH chemistry.

Figure 4 shows the breakdown in OH reactivity of the primary NMOG measured by PTR-ToF-MS during the Firelab study (Koss et al., 2018). Each bar represents a fraction of the total calculated OH reactivity, as represented by Equation 2.

$$f_{OHR,i} = \frac{k_i \times C_i}{\sum_i^n k_i \times C_i} \tag{2}$$

Where *i* is the species of interest, *n* is the number of species measured by the PTR-ToF-MS, *k* is the OH rate constant, and *C* is the average concentration measured during a burn. Shown are median, average, 25^{th}, and 75^{th} percentiles for all the burns reported by Koss et al. (2018). The color of each bar indicates if a compound is included or missing from the MCM. Species identifications, and the isomer contributions to each detected mass, were determined by Koss et al. (2018) for four fuel types (Douglas fir, Engelmann spruce duff, subalpine fir, and sage) using gas-chromatography pre-separation (GC-PTR-ToF-MS). Additional evidence for species identification was provided by other measurement techniques (e.g., I-CIMS, gas-chromatography electron-impact mass spectrometry, and OP-FTIR). On average, the isomer contribution to a given mass measured by PTR-ToF-MS varied by only 11%. To be consistent with Koss et al. (2018), it is assumed that the NMOG contribution to each mass detected by PTR-ToF-MS follows the average distribution measured by GC-PTR-ToF-MS.

For most NMOG measured by PTR-ToF-MS, the contribution to total primary OH reactivity varied by only 25%. Notably, the contribution from the sum of monoterpenes varied by a factor > 2. Monoterpenes, as well as isoprene and sesquiterpenes, were primarily emitted at the beginning of an experiment, prior to combustion, due to distillation processes associated with fuel heating (Sekimoto et al., 2018). This "distillation phase" was most pronounced in fires containing greater amounts of canopy material, or fuel types known to be strong monoterpene emitters (e.g. pines). Other NMOG were primarily emitted due to pyrolysis processes. For example, Sekimoto et al. (2018) found that the proportions of NMOG emitted during low- and high-temperature pyrolysis did not strongly vary by fuel type. In ambient fires, the contribution of monoterpenes to the total OH reactivity will likely differ from the contributions reported here, owing to the different burning process by which monoterpenes and other NMOG are emitted. In this study, the primary monoterpene isomers measured by GC-PTR-ToF-MS for Engelmann spruce, Douglas fir, and subalpine fir were camphene, α-pinene, β-pinene, 3-carene, and limonene followed by smaller amounts of tricyclene and α-terpinene (Fig. S3). No other NMOG detected by the GC-PTR-ToF-MS produced signals at *m/z* 137, which is the primary ion used to quantify monoterpene emissions (Fig. S3 and Koss et al., 2018).

The monoterpene distribution for Engelmann spruce (F26) was explicitly measured by GC-PTR-ToF-MS, but not for ponderosa pine (F38). To account for differences in monoterpene reactivity, the sum of monoterpenes for F26 is speciated using the distribution reported in Figure S3A. For F38, monoterpenes are speciated using the ponderosa pine distribution reported by Hatch et al. (2015) . Engelmann spruce smoke measured by GC-PTR-ToF-MS had a monoterpene distribution that was 25% α-pinene, 21% β-pinene, 25% 3-carene, 15% α-terpinene, and $\sim$ 5% each of limonene and camphene. Hatch et al. (2015) reports that the monoterpenes from ponderosa pine smoke are 10% α-pinene and 20% each for β-pinene, 3-carene, myrcene, and limonene. The MCM represents the chemistry of α-pinene, β-pinene, and limonene, but does not explicitly describe other important monoterpenes (e.g. 3-carene or camphene). For the mini chamber model, the fraction attributed to α-pinene, β-pinene, and limonene are explicitly prescribed. The fraction of 3-carene, α-terpinene, and smaller monoterepenes are lumped to α-pinene (endocyclic double bond) and the fractions associated with myrcene + camphene are lumped to β-pinene (exocyclic double bond).

On average, the MCM v 3.3.1 captures only $\sim$ 60% of the primary OH reactivity measured by the PTR-ToF-MS. The MCM generally lacks information about furan species and substituted aromatics, such as guaiacol and methyl guaiacol. Previous work has shown that furans constitute a significant fraction of the total primary OH reactivity (e.g. Gilman et al., 2015; Hatch et al., 2015, 2017; Koss et al., 2018); however, no studies have included the known mechanisms of these species when modeling biomass burning smoke chemistry. 5-methylfurfural and 2,5-dimethylfuran are the two largest contributors to this "missing reactivity" and account for nearly 10% of the calculated total reactivity. Up to 75% of the calculated primary OH reactivity can be accounted for by including the chemistry of furan, 2-methylfuran, 2,5-dimethylfuran, furfural, 5-methylfurfural, and guaiacol, along with the known species represented in the MCM. Much of the remaining reactivity is tied into species whose chemistry has not been extensively studied, including lesser abundant furans and oxygenated aromatics.

The mechanisms of select furan and oxygenated species are incorporated to the MCM based on previous work summarized in Figures S4 - S9 (Bierbach et al., 1995; Alvarez et al., 2009; Aschmann et al., 2011, 2014; Strollo and Ziemann, 2013; Zhao and Wang, 2017). In total, 65 reactions are added. The products resulting from the OH oxidation of furan and 2-methylfuran were first investigated by Bierbach et al. (1995) and later generalized to 3-methylfuran, 2,3-dimethylfuran, and 2,5-dimethylfuran by Aschmann et al. (2014) and Strollo and Ziemann (2013). Figure 5 shows the generalized furan oxidation scheme. Furan oxidation is initiated by an OH addition to the 2, 5, or 3-position. Addition to the 2 or 5-position is most favorable and results in pathways where substituents are either retained or lost (henceforth referred to as the loss and retention pathways). The retention pathway (path A in Fig. 5) leads to reactive unsaturated 1,4-dicarbonyls (e.g. 1,4-butenedial from furan oxidation), whereas the loss pathway (paths B1 and B2 in Fig. 5) results in the formation of hydroxy furanones and unsaturated carbonyl-acids (Aschmann et al., 2014; Strollo and Ziemann, 2013). The loss pathway becomes more dominant with higher number of substituted methyl groups.This study assumes branching ratios of [0.7 (A), 0.3 (B1)] for furan, [0.31 (A), 0.39 (B1), 0.31 (B2)] for 2-methylfuran, and [0.27 (A), 0.73 (B1)] for 2,5-dimethylfuran (Aschmann et al., 2014).

RO_2 reactions leading to the formation of carbonyls are implemented based on the mechanisms proposed by Aschmann et al. (2014) and Bierbach et al. (1994) (Figures S4 - S6). It is assumed that RO_2 species undergo reactions with HO_2, NO, and other RO_2 radicals. Other pathways, such as RO_2 + NO_2 and RO_2 + NO_3, are not included; however, these reactions could be

important for acyl RO_2 species (Orlando and Tyndall, 2012; Peng et al., 2019). For RO_2 + NO reactions, it is assumed that the alkoxy radical quickly decays (either by thermal degradation or reaction with O_2) to form carbonyls. Aschmann et al. (2014) did not report species consistent with alkoxy isomerization; thus, these reactions are ignored. Similarly, RO_2 + RO_2 reactions are assumed to only form alkoxy radicals, which may subsequently degrade to from carbonyls. Peroxides are assumed to be the only products of RO_2 + HO_2 reactions. These species are assumed to undergo photolysis to form carbonyls. Peroxides may also react with OH, and the resulting products differ depending on structure. For structures with an alpha hydrogen, it is assumed that OH abstracts at the alpha position, and that the resulting radical quickly decomposes to form a carbonyl + OH (e.g. HYDFURANOOH, Figure S4). For other structures, it is assumed that the hydrogen of the peroxide group is abstracted to regenerate the RO_2 radical.

The generic MCM rate constants are applied for RO_2 + HO_2 and RO_2 + NO reactions (k_{RO2NO} = 2.7 $\times 10^{-12}$ exp(360/T) cm^3 molec $^{-1}$ s^{-1}, k_{RO2HO2} = 2.91 $\times 10^{-13}$ exp(1300/T)[1 – exp(-0.245*n*)] cm^3 molec $^{-1}$ s^{-1}). The RO_2 + HO_2 rate constant is adjusted for the RO_2 carbon number, *n*, as recommended by Saunders et al. (2003). Photolysis frequencies for peroxides are assumed to be the same as for methyl hydroperoxide (J_{41} in the MCM), and peroxide + OH reactions are assumed to have a rate constant of 4×10^{-11} cm^3 molec $^{-1}$ s^{-1}. The assumed rate constants for RO_2 + RO_2 reactions are chosen based on those of structurally similar RO_2 radicals reported in the MCM. RO_2 H-shift isomerization (autoxidation) is not broadly represented in MCM v. 3.3.1, aside for isoprene oxidation (Jenkin et al., 2015). RO_2 isomerization becomes competitive when the bimolecular lifetime of RO_2 is on the order of 10s (Crounse et al., 2013; Praske et al., 2018). Based on the modeled concentrations of HO_2, NO, and RO_2, the bimolecular lifetime of RO_2 radicals from furan oxidation is estimated to be $\sim$ 10s; consequently, RO_2 isomerization could play a role for certain species.

Following RO_2 reaction, it is assumed that the second-generation products continue through the chemistry prescribed by MCM v 3.3.1. Unsaturated dicarbonyls, such as 1,4-butenedial, and the tautomers of hydroxy furanones are represented in the MCM (Figures S4 - S6). Here, it is assumed that hydroxy furanones undergo the same reactions as the corresponding tautomer, which ultimately leads to anhydride formation. Maleic anhydride is a multi-generational product in the OH oxidation of furan (Bierbach et al., 1995) and is considered to be a significant product of hydroxy furanone oxidation (Bierbach et al., 1994).

No experimental studies have evaluated the OH oxidation mechanism of furfural or 5-methylfurfural. Zhao and Wang (2017) found via theoretical quantum chemistry calculations that OH likely adds to the 2 or 5-position or abstracts a hydrogen from the aldehyde. The resulting reactions follow loss and retention pathways similar to the general mechanism for methyl-substituted furans (Fig. 6). When OH adds to the 2-position, the ring most likely opens to form an unsaturated tri-carbonyl (retention, path A). When OH adds to the 5-position, the resulting peroxy radical may react with HO_2, NO, or other other RO_2 species to form a hydroxy furanone / carbonyl acid mixture (loss, path B). Hydrogen abstraction from the aldehyde group is believed to ultimately result in the formation of maleic anhdyride (loss, path C). Zhao and Wang (2017) estimate furfural + OH branching ratios of 0.37 for channel A, 0.6 for channel B, and 0.03 for channel C. The same branching ratios are applied here, but a discussion of secondary NMOG sensitivity to the assumed furfural mechanism is provided in the supplemental information. The 5-methylfurfural + OH mechanism has not been studied and is assumed to have branching ratios similar to furfural. RO_2 reactions are implemented based on the mechanisms proposed by Zhao and Wang (2017) (see Figures S7 - S9).

Furfural strongly absorbs at 185 and 254 nm (Gandini et al., 1976; Hiraoka and Srinivasan, 1968; Ferreira da Silva et al., 2015). Smaller amounts may be lost by photolysis at wavelengths > 300 nm (Colmenar et al., 2015). Approximately 15% of furfural photolysis leads to the formation of furan and CO, while the remaining results in the formation of propyne, CO, and other C_3 compounds (Gandini et al., 1976). The photolysis frequency is calculated based on the cross sections reported by Ferreira da Silva et al. (2015) and quantum yield of 0.6 (V. Papadimitriou, personal communication).

Few studies have evaluated the OH oxidation mechanism of guaiacol. Yee et al. (2013) identified products from low-NO_x guaiacol oxidation, but did not calculate product yields. Lauraguais et al. (2014) studied guiacol oxidation in the presence of NO_x and observed substantial SOA formation. The only reported gas-phase species were a suite of nitroguaiacols composed primarily of 3- and 6-nitroguaiacol (6% yield) and 4-nitroguaiacol (10% yield). The mechanism proposed by Lauraguais et al. (2014) is applied here assuming a 16% yield of nitroguaiacol species (Fig. S10).

The OH loss of butanol-d9 is also included in the model to validate OH concentrations in the chamber. The OH oxidation of butanol-d9 is assumed to form a single, non-reactive species.

3.2.2 Model/Measurement Evaluation

Figure 7 shows the model comparison with PTR-ToF-MS measurements of butanol-d9 and select primary NMOG for F38. Overall, there is good agreement between the measurements and model output for most NMOG (exceptions include some primary species and small secondary oxygenates, discussed below). The excellent agreement between the measured and modeled loss of butanol-d9 demonstrates that OH concentrations in the chamber are well-represented by the model. Similar agreement is observed for F26, which had an initial NO_x/NMOG ratio that was an order of magnitude lower than that of F38 (Figure S11). Figure 8 shows the model output compared to the observed profiles of secondary NMOG measured during F38. The equivalent for F26 is presented in Figure S12. Panel A shows measurements of $C_4H_2O_3$ (maleic anhydride) as measured by PTR-ToF-MS, whereas panels B and C show I-CIMS measurements of $C_5H_6O_3$ and $C_4H_4O_3$, respectively. The measured secondary NMOG are compared to model outputs of total $C_4H_2O_3$ (i.e., the sum of all species with molecular formula $C_4H_2O_3$), total $C_5H_6O_3$, total $C_4H_4O_3$, and individual NMOG. Figure 8 also show model runs with the initial conditions of furan, 2-methylfuran, 2,5-dimethylfuran, furfural, 5-methylfurfural, and furanone set to zero. The PTR-ToF-MS measurements of $C_4H_2O_3$ are reported in units of ppb and can therefore be quantitatively compared to model output. I-CIMS measurements are reported as ncps; consequently, only qualitative comparisons are drawn based on similarities in model/measurement temporal profiles.

$C_4H_2O_3$, $C_5H_6O_3$, and $C_4H_4O_3$ were shown in Section 3.1 to constitute some of the most abundant photochemical products observed by PTR-ToF-MS and I-CIMS. The model runs in Figures 8 and S12 demonstrate that furan chemistry significantly contributes to the modeled formation of these secondary NMOG. The model also supports the inference that these masses correspond to measurements of maleic anhydride, methyl hydroxy furanone, and hydroxy furanone, respectively. This is most evident by comparing the shape of the temporal profiles between the measurements and modeled output. Maleic anhydride is the only species in the MCM with chemical formula $C_4H_4O_3$, and the model generally captures the peak $C_4H_4O_3$ signal after $\sim$ 20 min of oxidation to within the uncertainty of the measurement ($\sim$ 50%). Several species with chemical formula $C_5H_6O_3$ are represented in the MCM. Here, the modeling output is dominated by methyl hydroxy furanone and its tautomer,

β-acetylacrylic acid. Finally, I-CIMS measurements of $C_4H_4O_3$ are best captured by the model output of hydroxy furanone and its tautomer, malealdehydic acid.

The temporal profile of $C_7H_7NO_4$ is also well described by model output of nitroguaiacol (Fig. S13). Nitroaromatics are formed by the reaction of NO_2 with the o-semiquinone radical resulting from OH abstraction of the phenolic hydrogen Finewax et al. (2018). NO_2 was abundant at the beginning of mini chamber experiments performed on flaming emissions (Fig. S2); thus, nitroaromatics are expected to be present in many burns studied here. Note that only the results from F38 are shown. Very little formation of nitroguaiacol was observed in F26, owing to the relatively low amount of NO_x emitted from the smoldering combustion of Engelmann spruce duff.

The model provides insights into the formation pathways of important secondary NMOG, which could be used to place constraints on plume properties. For example, measurements of maleic anhydride, hydroxy furanone, and methyl hydroxy furanone could be used as proxies to estimate plume age since the furanones will likely be enhanced in younger plumes, whereas maleic anhydride will likely be enhanced in aged plumes. In plumes containing high proportions of furans, it could be feasible to evaluate furan chemistry to derive important modeling constraints, such as OH exposures.

Despite the success of the model in reproducing a number of observations, several differences exist as described below. First, the model output exhibits a faster decay of furans than what is observed by PTR-ToF-MS (Figure 7). This likely reflects the uncertainty associated with the mass assignment of furan species. Using GC-PTR-ToF-MS, Koss et al. (2018) showed that nearly 50% of the primary signal at $C_5H_6O-H^+$ (mass of 2-methylfuran) and $C_6H_8O-H^+$ (mass of 2,5-dimethylfuran) is associated with unidentified oxygenates. These unidentified species likely have different reactivities towards OH which may lead to model/observation disagreement. Likewise, secondary NMOG isomers could also form at these masses, further confounding model predictions of furans.

The decay of furfural is distinct from other furans because several processes contribute to temporal profile of $C_5H_4O_4-H^+$. Notable, there appears to be a fast decay of $C_5H_4O_4-H^+$, followed by a slower decay after 10s of oxidation. The model generally captures the fast decay of $C_5H_4O_4-H^+$, which is almost entirely due to photolysis of furfural. This degree of photolysis is different from the real atmosphere and results from furfural's exceptionally large cross section at 254 nm ($>$ 5×10^{-17} cm^2, Ferreira da Silva et al., 2015). The slower decay appears to result from an interference of another NMOG. This is supported by the I-CIMS which measured the formation of a mass with formula $C_5H_4O_4-I^-$. The I-CIMS is not sensitive to primary furan species, therefore this species is likely to be a secondary NMOG that is isomeric with furfural. This may explain why PTR-ToF-MS measurements of $C_5H_4O_4-H^+$ do not quickly decay to zero, as suggested by the model. It is notable that the formation of this secondary species is significant ($\sim$ 50% of the signal of primary furfural), which indicates that this is likely a secondary product formed from an abundant primary NMOG.

Despite the complications imposed by furfural photolysis, other furans and oxygenated aromatics do not exhibit strong absorption and are expected to be lost mostly by reaction with OH. Other absorbing species, such as methyl ethyl ketone and benzaldehyde, exhibit modeled photolysis losses on the order of 30%, which is likely a more typical fraction for other photo-active species. More details comparing the chamber results to chemistry of ambient biomass burning plumes are provided in Section 3.2.3.

At the beginning of each experiment, PTR-ToF-MS measurements show a sharp increase in $C_4H_2O_3$ that is not readily captured by the model (Figure 8). This increase could result from fast formation of maleic anhydride, or is possibly another species with molecular formula $C_4H_2O_3$. The model underpredicts maleic anhydride concentrations towards the end of the experiment, which likely points to additional sources of maleic anhydride that are not included in the model. The model reproduces peak maleic anhydride concentrations in F38 (Fig. 8A), but over predicts peak maleic anhydride concentrations by a factor of 1.6 in F26 (Fig. S12A).

After $\sim$ 30 min of oxidation, the model sum of $C_4H_4O_3$ approaches zero, yet the I-CIMS signal remains elevated (Figures 8C). This may indicate that a slow-forming product is detected by I-CIMS, or that the OH rate constant of hydroxy furanone is overestimated. As discussed in Section 3.1, the PTR-ToF-MS detects a slow-forming product that likely corresponds to succinic anhydride (Fig. 1).The I-CIMS is sensitive to anhydrides; thus, it is possible that the elevated signal at longer oxidation timescales corresponds to the measurement of succinic anhydride. Succinic anhydride is not represented in the customized mechanism; consequently, no model output is available for comparison.

Figure 2 shows that small oxygenates are also abundant secondary NMOG (i.e. acetaldehyde and formaldehyde); however, these species are underpredicted by the model by a factor of 10 or more (Fig. S13). This likely reflects additional chemical precursors or chemical pathways that are unaccounted for within the mini chamber model. Furthermore, heterogeneous reactions, such as those on aerosol particles or Teflon surfaces (e.g., Zádor et al., 2006; Chapleski et al., 2016), or photolysis at 254 nm may contribute to the formation of these small oxygenates.

It is noted that without calibrated I-CIMS data, it is difficult to assess whether the budget of these secondary NMOG is fully represented by the model. Although it is expected that furans will be a primary precursor of $C_4H_4O_3$ and $C_5H_6O_3$ in real biomass burning plumes, the model indicates that other highly reactive species may also contribute to these masses. In F38, furans account for $\sim$ 80% of the modeled production of $C_4H_4O_3$ and $\sim$ 90% of the modeled production of $C_5H_6O_3$. In contrast, furans account for $\sim$ 60% of the modeled production of $C_5H_6O_3$ and $\sim$ 85% of the modeled production of $C_4H_4O_3$ during F26. The remaining production in the model is attributed to the OH oxidation of oxygenated aromatics - specifically, phenol and cresol. These oxygenated aromatics are more abundant during F26 due to the higher degree of smoldering combustion. These differences highlight the variability of secondary NMOG production and also imply that there could be remaining precursors of $C_4H_4O_3$ and $C_5H_6O_3$. These precursors would have to be highly reactive molecules with carbon number ≥ 4. There are a number of furans and oxygenated aromatics that could possibly contribute to the formation of these secondary NMOG (e.g. hydroxymethylfurfural, Fig. 4), but whose chemical mechanism remains unknown.

3.2.3 Comparison of Chamber Chemistry to Atmospheric Conditions

The high-OH environment in the mini chamber is similar to those produced in oxidation flow reactors. Peng et al. (2016, 2019) showed that oxidation flow reactors can be operated under conditions that approximate the chemistry of the atmosphere; however, the use of 254 nm light can lead to non-atmospheric reactions. For example, furfural photolysis is unlikely to play a significant role in the chemistry of real smoke, and NO_x cycling is faster under ambient photolysis. Furthermore, high OH environments may lead to RO_2 fates that differ from ambient systems. In the atmosphere, the predominant fate of RO_2 is

reaction with NO or HO_2. In wildfires, RO_2 reactions with NO_2 are also important in forming PAN and other peroxy nitrates (Alvarado et al., 2010). In low NO_x environments, RO_2 + RO_2 and RO_2 isomerization may also play a role (Crounse et al., 2013; Praske et al., 2018). RO_2 isomerization was not included in the mechanism described here. The following discussion compares the modeled chemistry in the chamber to that expected for an ambient biomass burning plume.

In the atmosphere, primary NMOG are mostly consumed by reaction with OH or via photolysis during the daytime, and reaction with O_3 or NO_3 at night. Table S4 shows the estimated contribution of each process to the primary NMOG consumed for F26 and F38. Also shown are the NMOG losses calculated from simulations of the ambient biomass burning plume described by Müller et al. (2016) (see Section 3.2.4 for details of this modeling). For most species, the predominant loss pathway is reaction with OH. Ozonolysis is negligible for most species, except for a small fraction of the monoterpenes ($\sim 1\%$). On the other hand, significant losses of NMOG occur by photolysis, and to a lesser extent, reaction by NO_3. Aside from furfural, loss by photolysis was dominant for acetone and 2,3-butanedione ($> 50\%$), significant for methyl ethyl ketone and benzaldehyde ($\sim$30%), and moderate for hydroxyacetone, glyoxal, methyl glyoxal, formaldehyde, and acetaldehyde ($< 10\%$). In general, photolysis losses were dependent on the relative ratio between the OH rate constant and photolysis frequency at 254 nm (Table S3). Photolysis losses were greatest for conjugated aldehydes and species with low OH rate constants and high absorption cross-sections. (e.g., acetone, Table S3). Conjugated aldehydes such as furfural are highly reactive towards OH; consequently, losses due to photolysis are notable since these processes represent unintended sinks of potentially important SOA and ozone precursors. In contrast, photolysis losses of other species, such as acetone, is likely less important since these species are less reactive towards OH. It is noted that other species reported here are likely to photolyze, but whose absorption cross-sections at 254 nm have not been measured (e.g. 5-methylfurfural, Colmenar et al., 2015).

Because numerous species absorb across a wide wavelength spectrum (e.g. acetaldehyde and hydroxyacetone Burkholder et al., 2015), there is some agreement between the photolysis losses estimated in the mini chamber with those expected under ambient conditions. For hydroxyacetone, 2,3-butanedione, and acetaldehyde, reaction by photolysis was comparable to what was estimated for the ambient biomass burning plume described by Müller et al. (2016). In contrast, conjugated aldehydes, such as furfural and benzaldehyde, are characterized with absorption cross sections that favor shorter wavelengths; consequently, photolysis losses in the mini chamber greatly exceed those expected in ambient plumes. These results highlight the challenges associated with studying multi-day oxidation of biomass burning smoke in environmental chambers. Biomass burning emissions contain a myriad of functionalized NMOG that readily photolyze at wavelengths required to generate high OH environments. Experimental setups employing UVC lights must weigh the option between operating at high OH exposures (and thus progressing through chemistry quickly) with operating at gradual OH exposures that allow for longer sampling, but higher exposures to UVC light. Similar considerations are made for oxidation flow reactors, although nearly all experiments are conducted at high OH exposures since sampling is conducted at pseudo steady-state (Peng et al., 2016). To avoid high photolysis exposures, future experiments employing 254 nm light may consider operating with higher ozone concentrations to increase the losses due to reaction by OH. Alternatively, chamber experiments operated at high relative humidity may employ 185 nm light to generate high OH environments (Peng et al., 2016). In both cases, the chemistry will progress quickly, which may be undesirable for chamber experiments using low time-resolution instrumentation. Another approach may be to use UVB

or UVA lights and photolyze HONO to generate OH. This approach will reduce photolysis exposures, but may only access 1-2 days of atmospheric-equivalent oxidation.

Unlike primary emissions which are dependent on the balance between photolysis and oxidant concentrations, the formation of secondary NMOG largely depends on the fate of the RO_2 radical. Figure 9 A and B shows a breakdown of the modeled RO_2 pathways that contributed to the chemistry of the mini chamber. The bars show the fraction RO_2 radicals, separated by carbon number, that reacted through RO_2 + NO, RO_2 + HO_2, RO_2 + NO_2, and RO_2 + RO_2 pathways. Panel C shows the breakdown of RO_2 pathways for simulations of the ambient biomass burning plume.

RO_2 radicals in F38 largely reacted through two pathways - RO_2 + HO_2 and RO_2 + NO_2. The RO_2 + NO_2 pathway primarily influenced the fate of smaller RO_2 radicals (C$\leq$3), leading to the formation of peroxy nitrates (specifically, PAN). For larger RO_2 radicals (C$\geq$4), the dominant pathway was RO_2 + HO_2. On the other hand, the model suggests that the RO_2 + RO_2 pathway played a significant role in the chemistry of F26. This results, in part, from the higher initial NMOG loading for F26 ($\sim$ 280 ppb) compared to that of F38 ($\sim$ 180 ppb), which enhanced the rate of RO_2 production. The model suggests that the relative contribution of RO_2 cross-reactions was lower for higher carbon species; however, it is possible that these reactions produced accretion products unlikely to be found under ambient conditions. As discussed in Section 2.3.2 and shown in Figure S2, F26 was not representative of most fires studied here. For the majority of fires presented in Figures 2 and 3, the secondary NMOG were likely formed through the pathways consistent with F38.

In general, most of the higher carbon species in F38 followed atmospherically-relevant pathways. For some species, RO_2 + RO_2 reactions were also observed. While initial NMOG loadings may explain part of the enhanced RO_2 + RO_2 rate, some fraction may also be attributed to the limited degree of NO_x cycling in the mini chamber. Under ambient conditions, NO_2 is photolyzed to NO, which then reacts with RO_2 (and HO_2) radicals. Consequently, the RO_2 + NO pathway may act to lower the fraction of radicals that follow the RO_2 + RO_2 pathway. This is evidenced by the biomass burning plume described by Müller et al. (2016) which shows that the RO_2 + NO pathway is the dominant fate for most RO_2 species under ambient photolysis. In the mini chamber, NO_2 does not strongly absorb at 254 nm and is quickly lost to PAN or HNO_3; consequently, NO_x does not play a significant role in the chemistry of higher carbon RO_2 radicals.

The primary focus of this study is to understand the formation of major secondary NMOG measured by I-CIMS; thus, it is instructive to identify the modeled radical pathways that contribute to these formation rates. Figure S14 shows the pathways for the radicals that lead to the formation of hydroxy furanone and methyl hydroxy furanone. For both experiments, the hydroxy furanone radicals predominantly react through RO_2 + HO_2 pathways. For F26, $\sim$ 15% of the RO_2 radicals react through the RO_2 + RO_2 pathways whereas $\sim$ 8% follow this pathway for F38. These results suggest that the RO_2 + RO_2 pathway played some role in both experiments, but that the formation of hydroxy furanones in F38 predominantly followed atmospherically-relevant pathways. It is noted that as with other RO_2 radicals, these species are expected to mostly react with NO under ambient conditions (Fig. S14). Despite this difference, the RO_2 + HO_2 pathway and the RO_2 + NO pathway are both expected to lead to hydroxy furanone formation (Figures S4 and S5).

3.2.4 Observations and box modeling of secondary NMOG in real biomass burning plumes

Section 3.2.3 shows that the radical pathways in the mini chamber exhibited similarities, as well as differences, to those expected under atmospheric photolysis. In order to evaluate the impact of furan chemistry under ambient conditions, this work builds upon the model described by Müller et al. (2016) to evaluate the customized MCM mechanism with measurements from a real biomass burning plume.

During the 2013 DISCOVER-AQ aircraft campaign, the NASA P-3B conducted several plume intercepts downwind of a controlled burn conducted in a mixed-forested ecosystem. NMOG were monitored by a PTR-ToF-MS, meteorological parameters (temperature, pressure, and relative humidity) were monitored by a suite of aircraft instrumentation, and NO_x and O_3 were monitored by chemiluminescence. Müller et al. (2016) modeled the chemical evolution NMOG using a semi-Lagrangian box model with a modified-MCM mechanism that included a basic oxidation scheme for furan and furfural. The authors successfully modeled the loss of primary NMOG, including furan and furfural, and captured trends in ozone, NO_x, and peroxyacetyl nitrate (PAN). Downwind of the fire, the authors observed the formation of NMOG, such as maleic anhydride, that could not be explained by the model.

The authors initialized the chemistry with measurements of NMOG, NO_x, and O_3 sampled in close proximity of the fire. Plume dilution was constrained based on the temporal evolution of CO. Background NMOG, NO_x, and O_3 concentrations were prescribed based on aircraft measurements conducted outside of the plume. The plume was simulated for 1 hr, and meteorological parameters were constrained based on measurements conducted at each plume crossing. Photolysis was prescribed based on observed NO_2 photolysis frequencies.

The analysis described Müller et al. (2016) is recreated here, but with the full mechanisms of furan, furfural, 2,-methylfuran, 2,5-dimethylfuran, and 5-methylfurfural incorporated into the MCM. Other mechanisms that were not previously analyzed by Müller et al. (2016) are also considered, including phenol, cresol, and catechol. These species have important contributions to the primary OH reactivity of biomass burning smoke and are explicitly represented in MCM v 3.3.1 (Fig. 4). The initial conditions of furan and furfural are prescribed based on the observed concentrations reported by Müller et al. (2016). 2-methylfuran, phenol, and cresol are constrained based on the signals measured at *m/z* 83.05 ($C_5H_6O{-}H^+$), *m/z* 95.045 ($C_6H_6O{-}H^+$), and *m/z* 109.066 ($C_7H_8O{-}H^+$), respectively. 2,5-dimethylfuran is isobaric with furfural and was not fully resolved by PTR-ToF-MS due to the overwhelming signal of furfural ($\sim$ 10 times greater than the signal of other furan species). 2,5-dimethylfuran is expected to significantly contribute to total NMOG concentrations and OH reactivity (Fig. 4); therefore, the initial concentration of 2,5-dimethylfuran is constrained based on the dimethylfuran/methylfuran ratio reported elsewhere ($\sim$ 0.5, Koss et al., 2018). Finally, methylfurfural and catechol are included based on the signal at *m/z* 111.049 ($C_6H_6O_2{-}H^+$), and it is assumed that 50% of the signal can be attributed to each compound as recommended by Koss et al. (2018). The initial concentrations of methylfurfural + catechol and cresol are adjusted to best match the decay of $C_6H_6O_2{-}H^+$ and $C_7H_8O{-}H^+$, respectively.

Figure 10 compares the model output to the dilution corrected concentrations of furans, oxygenated aromatics, maleic anhydride, and ozone. The model output of hydroxy furanone is also shown, but not compared to measurements since an I-

CIMS was not onboard the P-3B. Red lines show the model output with furan chemistry included in the model. Blue dotted lines show model output with initial furan concentrations set to zero.

The model satisfactorily reproduces the temporal profiles of furans, oxygenated aromatic species, maleic anhydride, and ozone. The model also predicts significant formation of hydroxy furanone. Similar to the mini chamber observations (Fig. 1), maleic anhydride exhibits a temporal profile that is consistent with a slow-forming product. The model output of hydroxy furanone exhibits a fast-forming temporal profile as expected from the mini chamber experiments (Fig. 1).

The production of maleic anhydride and hydroxy furanone is negligible when the initial concentrations of furan species are set to zero. For both species, furfural oxidation accounts for more than 50% of the total production. As discussed in Section 3.2.1, the furfural mechanism is based on theoretical calculations and the exact branching ratios may differ from those estimated by Zhao and Wang (2017). The assumed branching ratios weakly impact the formation of maleic anhyride, whereas hydroxy furanone is most impacted by the assumed branching ratio of the ring-retaining pathway (channel B, Fig S16). I-CIMS measurements of hydroxy furanone may provide better constraints on the relative importance of each pathway.

Good agreement between ozone measurements and model output was also observed by Müller et al. (2016). Most of the ozone production results from reactions involving HO_2 (formed primarily from OH + formaldehyde, CO, and furfural reactions), CH_3O_2 radicals (formed primarily from reactions involving acetaldehyde, 2,3-butanedione, and methylglyoxal), and NO. When furans are removed from the model, predicted ozone concentrations decrease by 12%. It is estimated that $\sim$ 5 ppb of ozone was produced from furan chemistry after 60 minutes of oxidation. Notably, ozone formation was not sensitive to the assumed furfural branching ratios (Fig. S16). It is noted that the contribution of ozone from furan chemistry will vary depending on NO_x conditions and that this estimate is not equivalent to a generalized ozone formation potential.

The products of furan chemistry are also reactive (e.g., hydroxy furanone, 1,4-butenedial, methyl hydroxy furanone, Figs S4-S9) and 1 hr of oxidation is too short to capture the total potential ozone produced from the oxidation of furan precursors. Figure 11 extrapolates the model forward to evaluate multi-generational oxidation processes on ozone formation. The model is extrapolated assuming that the dilution rate continues to follow an exponential decay (calculated based on the measured CO loss). The solar zenith angle and j_{NO2} are calculated based on time of day. Relative humidity, temperature, and pressure are assumed to remain constant following the last measured plume intercept.

Figure 11 shows the extrapolated modeling results of ozone, hydroxy furanone, and maleic anhydride until 5:30 PM local time when the solar zenith angle approaches 70° ($\sim$ 1.5 hr before sunset). Hydroxy furanone production maximizes after 1 hr of oxidation, and subsequently decays due to OH oxidation. In contrast, maleic anhydride continues to increase. Figure 11A shows the estimated ozone produced from furan chemistry (calculated as the difference between model runs initialized with and without furan species). Ozone production from furan oxidation continues to rise after 1 hr of aging, in part because of the oxidation of reactive secondary NMOG such as hydroxy furanone. After 4.5 hr of oxidation, the total ozone produced from furan chemistry is $\sim$ 8 ppb.

Figure 11 demonstrates that furan chemistry contributed to the evolution of ozone within 4 hours of emission. After 2 hr of aging, most furans have reacted ($<$ 20% remain), and their contribution to ozone production via reactions of secondary NMOG diminishes. It is important to note that ozone production will vary depending on NO_x availability, NO_x/NMOG ratios,

the chemical composition of the NMOG mixture, and meteorological conditions. Despite these factors, furan chemistry will likely play a role in ozone production for many biomass burning plumes due to the ubiquitous presence of furans in smoke (Stockwell et al., 2014, 2015; Gilman et al., 2015; Hatch et al., 2015; Bruns et al., 2017; Hartikainen et al., 2018; Koss et al., 2018; Sekimoto et al., 2018).

The plume described above is relatively young; however, observations from the mini chamber (Fig 1) and the continued formation of maleic anhydride in the extrapolated model suggests that this compound could be present in highly aged plumes. During the NOAA Shale Oil and Natural Gas Nexus (SONGNEX https://www.esrl.noaa.gov/csd/projects/songnex/) field campaign, the NOAA WP-3D aircraft intercepted a large biomass burning plume in the free troposphere above Montana, U.S. on April 21, 2015 (Baylon et al., 2017). The plume had been transported at least 4 days from wildfires in Siberia and affected large portions of the western U.S. The PTR-ToF-MS described in this study was also deployed on the WP-3B and the resulting measurements are presented in Fig 12. The aged plume (indicted by elevated mixing ratios of acetonitrile and acetic acid) exhibited clear enhancements in maleic anhydride and $C_4H_4O_3$, which is attributed to succinic anhydride. In contrast, furan mixing ratios did not increase above background levels, indicating that these species completely reacted before sampling by the P-3.

The lifetimes of maleic and succinic anhydride are long ($>$ 5 d at OH concentrations of $1.5\times$ 10^6 molecules cm^{-3}); consequently, these species may have formed from the OH oxidation of furans and oxygenated aromatics shortly down wind of the fire and survived transport to the western U.S. These species may have also formed during transit from the oxidation of slow-reacting aromatics, such as benzene. The detection of anhydrides in highly-aged plumes is consistent with the behavior of the mini chamber (Fig 1) and demonstrates the relevance of furans and aromatic oxidation on plume chemistry far downwind of fire sources.

4 Conclusions

This study evaluates the influence of understudied NMOG chemistry on the chemical evolution of laboratory and ambient biomass burning smoke. Smoke reacted with OH radicals exhibits fast decay of highly reactive organic species, such as furans and oxygenated aromatics, and significant formation of C_4 and C_5 oxygenates. A model incorporating furan chemistry into the MCM (v. 3.3.1) indicates that furan and oxygenated aromatic species are significant precursors of the secondary NMOG measured by PTR-ToF-MS and I-CIMS. Similar results are observed from modeling of a small understory fire (Müller et al., 2016), which demonstrates the importance of furan chemistry in real biomass burning plumes.

Maleic anhydride ($C_4H_2O_3$) and succinic anhydride ($C_4H_4O_3$) are identified as important secondary NMOG measured by PTR-ToF-MS. Those measured by I-CIMS are identified as methyl hydroxy furanone ($C_5H_6O_3$) and a mixture of hydroxy furanone and succinic anhydride ($C_4H_4O_3$). The link between these species and furan precursors may be useful in constraining OH exposures for biomass burning plumes measured in the ambient.

Previous studies have suggested that furan chemistry could play a significant role in ozone or SOA formation (Bruns et al., 2017; Hartikainen et al., 2018; Gilman et al., 2015; Hatch et al., 2015). For the biomass burning plume described by Müller

et al. (2016), furan species likely contributed up to ∼10% of total ozone production. The extent to which furans contribute to ozone formation will vary depending on burn conditions and models should include these species in order to improve ozone predictions, especially for young biomass burning plumes. Other major biomass burning oxidation products, such as formaldehyde and acetaldehyde, were not resolved by this work owing, in part, to the complexity of chemistry leading to small oxygenate formation. The unknown precursors or chemical processes leading to the formation of these species should be investigated in future work.

Author contributions. Firelab data were measured and processed by the following people: PTR-ToF-MS (MMC, ARK, KS, JdG, and CW); ACES (KZ,SSB); I-CIMS (BY, JEK, and JLZ); OP-FTIR (VS, RY); GC/PTR-ToF-MS (ARK, JBG); NO (JMR). JK and CC designed the mini chamber experiments. CY and DHH operated the mini chamber. Ambient VOC measurements from the 2013 DISCOVER-AQ campaign were provided by MM and AW. MMC customized the MCM and conducted the model runs. MMC prepared the manuscript with contributions from all co-authors.

Competing interests. The authors declare no competing interests

Acknowledgements. This work was supported by the National Oceanic and Atmospheric Administration Atmospheric Chemistry, Carbon Cycle & Climate Program, awards NA16OAR4310111 and NA16OAR4310112. CL and ARK were additionally supported by the National Science Foundation Graduate Research Fellowship Program. The authors thank all those who helped organize and participated in the 2016 FIREX intensive, particularly Edward O'Donnell and Maegan Dills for lighting the fires, Ted Christian, Roger Ottmar, David Weise, Mark Cochrane, Kevin Ryan, and Robert Keane for assistance with the fuels, and Shawn Urbanski and Thomas Dzomba for logistical support. The authors also thank Denise D. Montzka, David J. Knapp, and Andrew J. Weinheimer for permission to use NO_x and O_3 measurements from the WP-3D, and John D. Barrick for permission to use j_{NO2} measurements.

Data from mini chamber experiments and the SONGNEX flight from April 21, 2015 are available online (https://www.esrl.noaa.gov/csd/datasets.html)

References

Ahern, A. T., Goldberger, L., Jahl, L., Thornton, J., and Sullivan, R. C.: Production of N2O5 and ClNO2 through Nocturnal Processing of Biomass-Burning Aerosol, Environmental Science & Technology, 52, 550–559, https://doi.org/10.1021/acs.est.7b04386, 2018.

Akagi, S. K., Craven, J. S., Taylor, J. W., McMeeking, G. R., Yokelson, R. J., Burling, I. R., Urbanski, S. P., Wold, C. E., Seinfeld, J. H., Coe, H., Alvarado, M. J., and Weise, D. R.: Evolution of trace gases and particles emitted by a chaparral fire in California, Atmospheric Chemistry and Physics, 12, 1397–1421, https://doi.org/10.5194/acp-12-1397-2012, 2012.

Akagi, S. K., Yokelson, R. J., Burling, I. R., Meinardi, S., Simpson, I., Blake, D. R., McMeeking, G. R., Sullivan, A., Lee, T., Kreidenweis, S., Urbanski, S., Reardon, J., Griffith, D. W. T., Johnson, T. J., and Weise, D. R.: Measurements of reactive trace gases and variable O_3 formation rates in some South Carolina biomass burning plumes, Atmospheric Chemistry and Physics, 13, 1141–1165, https://doi.org/10.5194/acp-13-1141-2013, 2013.

Alvarado, M. J., Logan, J. A., Mao, J., Apel, E., Riemer, D., Blake, D., Cohen, R. C., Min, K. E., Perring, A. E., Browne, E. C., Wooldridge, P. J., Diskin, G. S., Sachse, G. W., Fuelberg, H., Sessions, W. R., Harrigan, D. L., Huey, G., Liao, J., Case-Hanks, A., Jimenez, J. L., Cubison, M. J., Vay, S. A., Weinheimer, A. J., Knapp, D. J., Montzka, D. D., Flocke, F. M., Pollack, I. B., Wennberg, P. O., Kurten, A., Crounse, J., Clair, J. M. S., Wisthaler, A., Mikoviny, T., Yantosca, R. M., Carouge, C. C., and Le Sager, P.: Nitrogen oxides and PAN in plumes from boreal fires during ARCTAS-B and their impact on ozone: an integrated analysis of aircraft and satellite observations, Atmospheric Chemistry and Physics, 10, 9739–9760, 2010.

Alvarado, M. J., Lonsdale, C. R., Yokelson, R. J., Akagi, S. K., Coe, H., Craven, J. S., Fischer, E. V., McMeeking, G. R., Seinfeld, J. H., Soni, T., Taylor, J. W., Weise, D. R., and Wold, C. E.: Investigating the links between ozone and organic aerosol chemistry in a biomass burning plume from a prescribed fire in California chaparral, Atmospheric Chemistry and Physics, 15, 6667–6688, 2015.

Alvarez, E. G., BorrAs, E., Viidanoja, J., and Hjorth, J.: Unsaturated dicarbonyl products from the OH-initiated photo-oxidation of furan, 2-methylfuran and 3-methylfuran, Atmospheric Environment, 43, 1603–1612, 2009.

Andreae, M. O., Browell, E. V., Garstang, M., Gregory, G. L., Harriss, R. C., Hill, G. F., Jacob, D. J., Pereira, M. C., Sachse, G. W., Setzer, A. W., Dias, P. L. S., Talbot, R. W., Torres, A. L., and Wofsy, S. C.: Biomass-burning emissions and associated haze layers over Amazonia, Journal of Geophysical Research: Atmospheres, 93, 1509–1527, https://doi.org/10.1029/JD093iD02p01509, 1988.

Aschmann, S. M., Nishino, N., Arey, J., and Atkinson, R.: Kinetics of the Reactions of OH Radicals with 2- and 3-Methylfuran, 2,3- and 2,5-Dimethylfuran, and E- and Z-3-Hexene-2,5-dione, and Products of OH + 2,5-Dimethylfuran, Environmental Science & Technology, 45, 1859–1865, 2011.

Aschmann, S. M., Nishino, N., Arey, J., and Atkinson, R.: Products of the OH Radical-Initiated Reactions of Furan, 2- and 3-Methylfuran, and 2,3- and 2,5-Dimethylfuran in the Presence of NO, J. Phys. Chem. A., 118, 457–466, 2014.

Atkinson, R., Baulch, D. L., Cox, R. A., Crowley, J. N., Hampson, R. F., Hynes, R. G., Jenkin, M. E., Rossi, M. J., Troe, J., and Subcommittee, I.: Evaluated kinetic and photochemical data for atmospheric chemistry: Volume II — gas phase reactions of organic species, Atmospheric Chemistry and Physics, 6, 3625–4055, https://doi.org/10.5194/acp-6-3625-2006, 2006.

Barmet, P., Dommen, J., DeCarlo, P. F., Tritscher, T., Praplan, A. P., Platt, S. M., Prévôt, A. S. H., Donahue, N. M., and Baltensperger, U.: OH clock determination by proton transfer reaction mass spectrometry at an environmental chamber, Atmospheric Measurement Techniques, 5, 647–656, 2012.

Baylon, P., Jaffe, D. A., de Gouw, J., and Warneke, C.: Influence of Long-Range Transport of Siberian Biomass Burning at the Mt. Bachelor Observatory during the Spring of 2015, Aerosol and Air Quality Research, 17, 2751–2761, 2017.

Bian, Q., May, A. A., Kreidenweis, S. M., and Pierce, J. R.: Investigation of particle and vapor wall-loss effects on controlled wood-smoke smog-chamber experiments, Atmospheric Chemistry and Physics, 15, 11 027–11 045, https://doi.org/10.5194/acp-15-11027-2015, https://www.atmos-chem-phys.net/15/11027/2015/, 2015.

Bierbach, A., Barnes, I., and Becker, K. H.: Atmospheric chemistry of unsaturated carbonyls: Butenedial, 4-oxo-2-pentenal, 3-hexene-2, 5-dione, maleic anhydride, 3H-furan-2-one, and 5-methyl-3H-furan-2-one, Environmental Science & Technology, 28, 715–729, 1994.

Bierbach, A., Barnes, I., and Becker, K. H.: Product and kinetic study of the OH-initiated gas-phase oxidation of furan, 2-methylfuran and furanaldehydes at≈ 300 K, Atmospheric Environment, 29, 2651–2660, 1995.

Brey, S. J. and Fischer, E. V.: Smoke in the City: How Often and Where Does Smoke Impact Summertime Ozone in the United States?, Environmental Science & Technology, 50, 1288–1294, 2016.

Bruns, E. A., Slowik, J. G., El Haddad, I., Kilic, D., Klein, F., Dommen, J., Temime-Roussel, B., Marchand, N., Baltensperger, U., and Prévôt, A. S. H.: Characterization of gas-phase organics using proton transfer reaction time-of-flight mass spectrometry: fresh and aged residential wood combustion emissions, Atmospheric Chemistry and Physics, 17, 705–720, 2017.

Buhr, K., van Ruth, S., and Delahunty, C.: Analysis of volatile flavour compounds by Proton Transfer Reaction-Mass Spectrometry: fragmentation patterns and discrimination between isobaric and isomeric compounds, International Journal of Mass Spectrometry, 221, 1–7, 2002.

Burkholder, J., Sander, S., Abbatt, J., Barker, J., Huie, R., Kolb, C., Kurylo, M., Orkin, V., Wilmouth, D., and Wine, P.: Chemical Kinetics and Photochemical Data for Use in Atmospheric Studies, Evluation No. 18, Jet Propulsion Laboratory, Pasadena, CA, 2015.

Burling, I. R., Yokelson, R. J., Griffith, D. W. T., Johnson, T. J., Veres, P., Roberts, J. M., Warneke, C., Urbanski, S. P., Reardon, J., Weise, D. R., Hao, W. M., and de Gouw, J.: Laboratory measurements of trace gas emissions from biomass burning of fuel types from the southeastern and southwestern United States, Atmospheric Chemistry and Physics, 10, 11 115–11 130, 2010.

Chapleski, R. C., Zhang, Y., Troya, D., and Morris, J. R.: Heterogeneous chemistry and reaction dynamics of the atmospheric oxidants, O3, NO3, and OH, on organic surfaces, Chem. Soc. Rev., 45, 3731–3746, https://doi.org/10.1039/C5CS00375J, http://dx.doi.org/10.1039/C5CS00375J, 2016.

Colmenar, I., González, S., Jiménez, E., Martín, P., Salgado, S., Cabañas, B., and Albaladejo, J.: UV absorption cross sections between 290 and 380 nm of a series of furanaldehydes: Estimation of their photolysis lifetimes, Atmospheric Environment, 103, 1–6, 2015.

Crounse, J. D., Nielsen, L. B., Jørgensen, S., Kjaergaard, H. G., and Wennberg, P. O.: Autoxidation of Organic Compounds in the Atmosphere, The Journal of Physical Chemistry Letters, 4, 3513–3520, https://doi.org/10.1021/jz4019207, 2013.

Deming, B., Pagonis, D., Liu, X., Day, D., Talukdar, R., Krechmer, J., de Gouw, J. A., Jimenez, J. L., and Ziemann, P. J.: Measurements of Delays of Gas-Phase Compounds in a Wide Variety of Tubing Materials due to Gas-Wall Interactions, Atmospheric Measurement Techniques Discussions, 2019, 1–19, https://doi.org/10.5194/amt-2019-25, https://www.atmos-meas-tech-discuss.net/amt-2019-25/, 2019.

Ferreira da Silva, F., Lange, E., Limão-Vieira, P., Jones, N. C., Hoffmann, S. V., Hubin-Franskin, M. J., Delwiche, J., Brunger, M. J., Neves, R. F. C., Lopes, M. C. A., de Oliveira, E. M., da Costa, R. F., Varella, M. T. d. N., Bettega, M. H. F., Blanco, F., García, G., Lima, M. A. P., and Jones, D. B.: Electronic excitation of furfural as probed by high-resolution vacuum ultraviolet spectroscopy, electron energy loss spectroscopy, and ab initiocalculations, The Journal of Chemical Physics, 143, 144 308–14, 2015.

Finewax, Z., de Gouw, J. A., and Ziemann, P. J.: Identification and Quantification of 4-Nitrocatechol Formed from OH and NO 3Radical-Initiated Reactions of Catechol in Air in the Presence of NO x: Implications for Secondary Organic Aerosol Formation from Biomass Burning, Environmental Science & Technology, 52, 1981–1989, 2018.

Ford, B., Val Martin, M., Zelasky, S. E., Fischer, E. V., Anenberg, S. C., Heald, C. L., and Pierce, J. R.: Future Fire Impacts on Smoke Concentrations, Visibility, and Health in the Contiguous United States, GeoHealth, 2, 229–247, 2018.

Gandini, A., Parsons, J. M., and Back, R. A.: The photochemistry of 2-furaldehyde vapour. II. Photodecomposition: direct photolysis at 253.7 and 313 nm and Hg(3P1)-sensitized decomposition, Canadian Journal of Chemistry, 54, 3095–3101, 1976.

Gaston, C. J., Lopez-Hilfiker, F. D., Whybrew, L. E., Hadley, O., McNair, F., Gao, H., Jaffe, D. A., and Thornton, J. A.: Online molecular characterization of fine particulate matter in Port Angeles, WA: Evidence for a major impact from residential wood smoke, Atmos. Envrion., 138, 99–107, https://doi.org/10.1016/j.atmosenv.2016.05.013, 2016.

Gilman, J. B., Lerner, B. M., Kuster, W. C., Goldan, P. D., Warneke, C., Veres, P. R., Roberts, J. M., de Gouw, J. A., Burling, I. R., and Yokelson, R. J.: Biomass burning emissions and potential air quality impacts of volatile organic compounds and other trace gases from fuels common in the US, Atmospheric Chemistry and Physics, 15, 13 915–13 938, 2015.

Hartikainen, A., Yli-Pirilä, P., Tiitta, P., Leskinen, A., Kortelainen, M., Orasche, J., Schnelle-Kreis, J., Lehtinen, K. E. J., Zimmermann, R., Jokiniemi, J., and Sippula, O.: Volatile Organic Compounds from Logwood Combustion: Emissions and Transformation under Dark and Photochemical Aging Conditions in a Smog Chamber, Environmental Science & Technology, 52, 4979–4988, 2018.

Hatch, L. E., Luo, W., Pankow, J. F., Yokelson, R. J., Stockwell, C. E., and Barsanti, K. C.: Identification and quantification of gaseous organic compounds emitted from biomass burning using two-dimensional gas chromatography–time-of-flight mass spectrometry, Atmospheric Chemistry and Physics, 15, 1865–1899, 2015.

Hatch, L. E., Yokelson, R. J., Stockwell, C. E., Veres, P. R., Simpson, I. J., Blake, D. R., Orlando, J. J., and Barsanti, K. C.: Multi-instrument comparison and compilation of non-methane organic gas emissions from biomass burning and implications for smoke-derived secondary organic aerosol precursors, Atmospheric Chemistry and Physics, 17, 1471–1489, 2017.

Hiraoka, H. and Srinivasan, R.: Vapor-Phase Photochemistry of Furfural, The Journal of Chemical Physics, 48, 2185–2189, 1968.

Hobbs, P. V., Sinha, P., Yokelson, R. J., Christian, T. J., Blake, D. R., Gao, S., Kirchstetter, T. W., Novakov, T., and Pilewskie, P.: Evolution of gases and particles from a savanna fire in South Africa, Journal of Geophysical Research, 108, 2003.

Hodshire, A. L., Bian, Q., Ramnarine, E., Lonsdale, C. R., Alvarado, M. J., Kreidenweis, S. M., Jathar, S. H., and Pierce, J. R.: More Than Emissions and Chemistry: Fire Size, Dilution, and Background Aerosol Also Greatly Influence Near-Field Biomass Burning Aerosol Aging, Journal of Geophysical Research: Atmospheres, 124, 5589–5611, https://doi.org/10.1029/2018JD029674, https://agupubs.onlinelibrary.wiley.com/doi/abs/10.1029/2018JD029674, 2019.

Huey, L. G., Hanson, D. R., and Howard, C. J.: Reactions of SF6- and I- with Atmospheric Trace Gases, The Journal of Physical Chemistry, 99, 5001–5008, https://doi.org/10.1021/j100014a021, 1995.

Jaffe, D., Chand, D., Hafner, W., Westerling, A., and Spracklen, D.: Influence of Fires on O 3Concentrations in the Western U.S., Environmental Science & Technology, 42, 5885–5891, 2008.

Jaffe, D. A. and Wigder, N. L.: Ozone production from wildfires: A critical review, Atmospheric Environment, 51, 1–10, 2012.

Jaffe, D. A., Wigder, N., Downey, N., Pfister, G., Boynard, A., and Reid, S. B.: Impact of Wildfires on Ozone Exceptional Events in the Western U.S., Environmental Science & Technology, 47, 11 065–11 072, 2013.

Jaffe, D. A., Cooper, O. R., Fiore, A. M., Henderson, B. H., Tonneson, G. S., Russell, A. G., Henze, D. K., Langford, A. O., Lin, M., and Moore, T.: Scientific assessment of background ozone over the U.S.: Implications for air quality management, Elem Sci Anth, 6, 56, 2018.

Jenkin, M. E., Saunders, S. M., and Pilling, M. J.: The tropospheric degradation of volatile organic compounds: a protocol for mechanism development, Atmospheric Environment, 31, 81–104, 1997.

Jenkin, M. E., Saunders, S. M., Wagner, V., and Pilling, M. J.: Protocol for the development of the Master Chemical Mechanism, MCM v3 (Part B): tropospheric degradation of aromatic volatile organic compounds, Atmospheric Chemistry and Physics, 3, 181–193, 2003.

Jenkin, M. E., Young, J. C., and Rickard, A. R.: The MCM v3.3.1 degradation scheme for isoprene, Atmospheric Chemistry and Physics, 15, 11 433–11 459, 2015.

Keller-Rudek, H., Moortgat, G. K., Sander, R., and Sörensen, R.: The MPI-Mainz UV/VIS Spectral Atlas of Gaseous Molecules of Atmospheric Interest, Earth System Science Data, 5, 365–373, https://doi.org/10.5194/essd-5-365-2013, https://www.earth-syst-sci-data.net/5/365/2013/, 2013.

Koss, A. R., Sekimoto, K., Gilman, J. B., Selimovic, V., Coggon, M. M., Zarzana, K. J., Yuan, B., Lerner, B. M., Brown, S. S., Jimenez, J. L., Krechmer, J., Roberts, J. M., Warneke, C., Yokelson, R. J., and de Gouw, J.: Non-methane organic gas emissions from biomass burning: identification, quantification, and emission factors from PTR-ToF during the FIREX 2016 laboratory experiment, Atmospheric Chemistry and Physics, 18, 3299–3319, https://doi.org/10.5194/acp-18-3299-2018, 2018.

Krechmer, J. E., Pagonis, D., Ziemann, P. J., and Jimenez, J. L.: Quantification of Gas-Wall Partitioning in Teflon Environmental Chambers Using Rapid Bursts of Low-Volatility Oxidized Species Generated in Situ, Environmental Science & Technology, 50, 5757–5765, https://doi.org/10.1021/acs.est.6b00606, 2016.

Lauraguais, A., Coeur-Tourneur, C., Cassez, A., Deboudt, K., Fourmentin, M., and Choël, M.: Atmospheric reactivity of hydroxyl radicals with guaiacol (2-methoxyphenol), a biomass burning emitted compound: Secondary organic aerosol formation and gas-phase oxidation products, Atmospheric Environment, 86, 155–163, 2014.

Lee, B. H., Lopez-Hilfiker, F. D., Mohr, C., Kurtén, T., Worsnop, D. R., and Thornton, J. A.: An Iodide-Adduct High-Resolution Time-of-Flight Chemical-Ionization Mass Spectrometer: Application to Atmospheric Inorganic and Organic Compounds, Environmental Science & Technology, 48, 6309–6317, 2014.

Lim, C. Y., Hagan, D. H., Coggon, M. M., Koss, A. R., Sekimoto, K., de Gouw, J., Warneke, C., Cappa, C. D., and Kroll, J. H.: Secondary organic aerosol formation from the laboratory oxidation of biomass burning emissions, Atmospheric Chemistry and Physics, 19, 12 797–12 809, https://doi.org/10.5194/acp-19-12797-2019, https://www.atmos-chem-phys.net/19/12797/2019/, 2019.

Liu, X., Jeffries, H. E., and Sexton, K. G.: Atmospheric Photochemical Degradation of 1,4-Unsaturated Dicarbonyls, Environmental Science & Technology, 33, 4212–4220, 1999.

Liu, X., Zhang, Y., Huey, L. G., Yokelson, R. J., Wang, Y., Jimenez, J. L., Campuzano-Jost, P., Beyersdorf, A. J., Blake, D. R., Choi, Y., St. Clair, J. M., Crounse, J. D., Day, D. A., Diskin, G. S., Fried, A., Hall, S. R., Hanisco, T. F., King, L. E., Meinardi, S., Mikoviny, T., Palm, B. B., Peischl, J., Perring, A. E., Pollack, I. B., Ryerson, T. B., Sachse, G., Schwarz, J. P., Simpson, I. J., Tanner, D. J., Thornhill, K. L., Ullmann, K., Weber, R. J., Wennberg, P. O., Wisthaler, A., Wolfe, G. M., and Ziemba, L. D.: Agricultural fires in the southeastern U.S. during SEAC4RS: Emissions of trace gases and particles and evolution of ozone, reactive nitrogen, and organic aerosol, Journal of Geophysical Research: Atmospheres, 121, 7383–7414, https://doi.org/10.1002/2016JD025040, 2016.

Mason, S. A., Field, R. J., Yokelson, R. J., Kochivar, M. A., Tinsley, M. R., Ward, D. E., and Hao, W. M.: Complex effects arising in smoke plume simulations due to inclusion of direct emissions of oxygenated organic species from biomass combustion, Journal of Geophysical Research: Atmospheres, 106, 12 527–12 539, https://doi.org/10.1029/2001JD900003, 2001.

Mauzerall, D. L., Logan, J. A., Jacob, D. J., Anderson, B. E., Blake, D. R., Bradshaw, J. D., Heikes, B., Sachse, G. W., Singh, H., and Talbot, B.: Photochemistry in biomass burning plumes and implications for tropospheric ozone over the tropical South Atlantic, Geophys Res, 103, 8401–8423, 1998.

Millet, D. B., Baasandorj, M., Farmer, D. K., Thornton, J. A., Baumann, K., Brophy, P., Chaliyakunnel, S., de Gouw, J. A., Graus, M., Hu, L., Koss, A., Lee, B. H., Lopez-Hilfiker, F. D., Neuman, J. A., Paulot, F., Peischl, J., Pollack, I. B., Ryerson, T. B., Warneke, C., Williams, B. J., and Xu, J.: A large and ubiquitous source of atmospheric formic acid, Atmospheric Chemistry and Physics, 15, 6283–6304, 2015.

Müller, M., Anderson, B. E., Beyersdorf, A. J., Crawford, J. H., Diskin, G. S., Eichler, P., Fried, A., Keutsch, F. N., Mikoviny, T., Thornhill, K. L., Walega, J. G., Weinheimer, A. J., Yang, M., Yokelson, R. J., and Wisthaler, A.: In situ measurements and modeling of reactive trace gases in a small biomass burning plume, Atmospheric Chemistry and Physics, 16, 3813–3824, 2016.

Orlando, J. J. and Tyndall, G. S.: Laboratory studies of organic peroxy radical chemistry: an overview with emphasis on recent issues of atmospheric significance, Chem. Soc. Rev., 41, 6294–6317, https://doi.org/10.1039/c2cs35166h, 2012.

Pagonis, D., Krechmer, J. E., de Gouw, J., Jimenez, J. L., and Ziemann, P. J.: Effects of gas–wall partitioning in Teflon tubing and instrumentation on time-resolved measurements of gas-phase organic compounds, Atmospheric Measurement Techniques, 10, 4687–4696, 2017.

Pagonis, D., Sekimoto, K., and de Gouw, J.: A library of proton-transfer reactions of H3O+ ions used for trace gas detection, J. Am. Soc. Mass Spectrom., p. in press, 2019.

Peng, Z. and Jimenez, J. L.: Modeling of the chemistry in oxidation flow reactors with high initial NO, Atmospheric Chemistry and Physics, 17, 11 991–12 010, 2017.

Peng, Z., Day, D. A., Ortega, A. M., Palm, B. B., Hu, W., Stark, H., Li, R., Tsigaridis, K., Brune, W. H., and Jimenez, J. L.: Non-OH chemistry in oxidation flow reactors for the study of atmospheric chemistry systematically examined by modeling, Atmospheric Chemistry and Physics, 16, 4283–4305, 2016.

Peng, Z., Lee-Taylor, J., Orlando, J. J., Tyndall, G. S., and Jimenez, J. L.: Organic peroxy radical chemistry in oxidation flow reactors and environmental chambers and their atmospheric relevance, Atmospheric Chemistry and Physics, 19, 813–834, https://doi.org/10.5194/acp-19-813-2019, https://www.atmos-chem-phys.net/19/813/2019/, 2019.

Praske, E., Otkjær, R. V., Crounse, J. D., Hethcox, J. C., Stoltz, B. M., Kjaergaard, H. G., and Wennberg, P. O.: Atmospheric autoxidation is increasingly important in urban and suburban North America, Proceedings of the National Academy of Sciences, 115, 64–69, https://doi.org/10.1073/pnas.1715540115, 2018.

Priestley, M., Le Breton, M., Bannan, T. J., Leather, K. E., Bacak, A., Reyes-Villegas, E., De Vocht, F., Shallcross, B. M. A., Brazier, T., Anwar Khan, M., Allan, J., Shallcross, D. E., Coe, H., and Percival, C. J.: Observations of Isocyanate, Amide, Nitrate, and Nitro Compounds From an Anthropogenic Biomass Burning Event Using a ToF-CIMS, Journal of Geophysical Research: Atmospheres, 123, 7687–7704, https://doi.org/10.1002/2017JD027316, 2018.

Reyes-Villegas, E., Priestley, M., Ting, Y.-C., Haslett, S., Bannan, T., Le Breton, M., Williams, P. I., Bacak, A., Flynn, M. J., Coe, H., Percival, C., and Allan, J. D.: Simultaneous aerosol mass spectrometry and chemical ionisation mass spectrometry measurements during a biomass burning event in the UK: insights into nitrate chemistry, Atmospheric Chemistry and Physics, 18, 4093–4111, https://doi.org/10.5194/acp-18-4093-2018, 2018.

Saunders, S. M., Jenkin, M. E., Derwent, R. G., and Pilling, M. J.: Protocol for the development of the Master Chemical Mechanism, MCM v3 (Part A): tropospheric degradation of non-aromatic volatile organic compounds, Atmospheric Chemistry and Physics, 3, 161–180, 2003.

Sekimoto, K., Li, S.-M., Yuan, B., Koss, A., Coggon, M., Warneke, C., and de Gouw, J.: Calculation of the sensitivity of proton-transfer-reaction mass spectrometry (PTR-MS) for organic trace gases using molecular properties, International Journal of Mass Spectrometry, 421, 71–94, 2017.

Sekimoto, K., Koss, A. R., Gilman, J. B., Selimovic, V., Coggon, M. M., Zarzana, K. J., Yuan, B., Lerner, B. M., Brown, S. S., Warneke, C., Yokelson, R. J., Roberts, J. M., and de Gouw, J.: High- and low-temperature pyrolysis profiles describe volatile organic compound emissions from western US wildfire fuels, Atmospheric Chemistry and Physics, 18, 9263–9281, 2018.

Selimovic, V., Yokelson, R. J., Warneke, C., Roberts, J. M., de Gouw, J., Reardon, J., and Griffith, D. W. T.: Aerosol optical properties and trace gas emissions by PAX and OP-FTIR for laboratory-simulated western US wildfires during FIREX, Atmospheric Chemistry and Physics, 18, 2929–2948, https://doi.org/10.5194/acp-18-2929-2018, 2018.

Stockwell, C. E., Yokelson, R. J., Kreidenweis, S. M., Robinson, A. L., DeMott, P. J., Sullivan, R. C., Reardon, J., Ryan, K. C., Griffith, D. W. T., and Stevens, L.: Trace gas emissions from combustion of peat, crop residue, domestic biofuels, grasses, and other fuels: configuration and Fourier transform infrared (FTIR) component of the fourth Fire Lab at Missoula Experiment (FLAME-4), Atmospheric Chemistry and Physics, 14, 9727–9754, https://doi.org/10.5194/acp-14-9727-2014, 2014.

Stockwell, C. E., Veres, P. R., Williams, J., and Yokelson, R. J.: Characterization of biomass burning emissions from cooking fires, peat, crop residue, and other fuels with high-resolution proton-transfer-reaction time-of-flight mass spectrometry, Atmospheric Chemistry and Physics, 15, 845–865, https://doi.org/10.5194/acp-15-845-2015, 2015.

Stockwell, C. E., Kupc, A., Witkowski, B., Talukdar, R. K., Liu, Y., Selimovic, V., Zarzana, K. J., Sekimoto, K., Warneke, C., Washenfelder, R. A., Yokelson, R. J., Middlebrook, A. M., and Roberts, J. M.: Characterization of a catalyst-based conversion technique to measure total particulate nitrogen and organic carbon and comparison to a particle mass measurement instrument, Atmospheric Measurement Techniques, 11, 2749–2768, 2018.

Strollo, C. M. and Ziemann, P. J.: Products and mechanism of secondary organic aerosol formation from the reaction of 3-methylfuran with OH radicals in the presence of NOx, Atmospheric Environment, 77, 534–543, 2013.

Tomaz, S., Cui, T., Chen, Y., Sexton, K. G., Roberts, J. M., Warneke, C., Yokelson, R. J., Surratt, J. D., and Turpin, B. J.: Photochemical Cloud Processing of Primary Wildfire Emissions as a Potential Source of Secondary Organic Aerosol, Environmental Science & Technology, 52, 11 027–11 037, https://doi.org/10.1021/acs.est.8b03293, 2018.

Westerling, A. L.: Warming and Earlier Spring Increase Western U.S. Forest Wildfire Activity, Science, 313, 940–943, 2006.

Wolfe, G. M., Marvin, M. R., Roberts, S. J., Travis, K. R., and Liao, J.: The Framework for 0-D Atmospheric Modeling (F0AM) v3.1, Geoscientific Model Development, 9, 3309–3319, 2016.

Yee, L. D., Kautzman, K. E., Loza, C. L., Schilling, K. A., Coggon, M. M., Chhabra, P. S., Chan, M. N., Chan, A. W. H., Hersey, S. P., Crounse, J. D., Wennberg, P. O., Flagan, R. C., and Seinfeld, J. H.: Secondary organic aerosol formation from biomass burning intermediates: phenol and methoxyphenols, Atmospheric Chemistry and Physics, 13, 8019–8043, 2013.

Yokelson, R. J., Griffith, D. W. T., and Ward, D. E.: Open-path Fourier transform infrared studies of large-scale laboratory biomass fires, Journal of Geophysical Research: Atmospheres, 101, 21 067–21 080, https://doi.org/10.1029/96JD01800, 1996.

Yokelson, R. J., Bertschi, I. T., Christian, T. J., Hobbs, P. V., Ward, D. E., and Hao, W. M.: Trace gas measurements in nascent, aged, and cloud-processed smoke from African savanna fires by airborne Fourier transform infrared spectroscopy (AFTIR), Journal of Geophysical Research: Atmospheres, 108, https://doi.org/10.1029/2002JD002322, 2003.

Yokelson, R. J., Crounse, J. D., DeCarlo, P. F., Karl, T., Urbanski, S., Atlas, E., Campos, T., Shinozuka, Y., Kapustin, V., Clarke, A. D., Weinheimer, A., Knapp, D. J., Montzka, D. D., Holloway, J., Weibring, P., Flocke, F., Zheng, W., Toohey, D., Wennberg, P. O., Wiedinmyer, C., Mauldin, L., Fried, A., Richter, D., Walega, J., Jimenez, J. L., Adachi, K., Buseck, P. R., Hall, S. R., and Shetter, R.: Emissions from biomass burning in the Yucatan, Atmospheric Chemistry and Physics, 9, 5785–5812, https://doi.org/10.5194/acp-9-5785-2009, 2009.

Yuan, B., Koss, A., Warneke, C., Gilman, J. B., Lerner, B. M., Stark, H., and de Gouw, J. A.: A high-resolution time-of-flight chemical ionization mass spectrometer utilizing hydronium ions (H_3O^+ ToF-CIMS) for measurements of volatile organic compounds in the atmosphere, Atmospheric Measurement Techniques, 9, 2735–2752, https://doi.org/10.5194/amt-9-2735-2016, 2016.

Yuan, B., Koss, A. R., Warneke, C., Coggon, M., Sekimoto, K., and de Gouw, J. A.: Proton-Transfer-Reaction Mass Spectrometry: Applications in Atmospheric Sciences, Chemical Reviews, 117, 13 187–13 229, 2017.

Zádor, J., Turányi, T., Wirtz, K., and Pilling, M. J.: Measurement and investigation of chamber radical sources in the European Photoreactor (EUPHORE), Journal of Atmospheric Chemistry, 55, 147–166, https://doi.org/10.1007/s10874-006-9033-y, https://doi.org/10.1007/s10874-006-9033-y, 2006.

Zarzana, K. J., Selimovic, V., Koss, A. R., Sekimoto, K., Coggon, M. M., Yuan, B., Dubé, W. P., Yokelson, R. J., Warneke, C., de Gouw, J. A., Roberts, J. M., and Brown, S. S.: Primary emissions of glyoxal and methylglyoxal from laboratory measurements of open biomass burning, Atmospheric Chemistry and Physics, 18, 15 451–15 470, 2018.

Zhao, X. and Wang, L.: Atmospheric Oxidation Mechanism of Furfural Initiated by Hydroxyl Radicals, J. Phys. Chem. A., 121, 3247–3253, 2017.

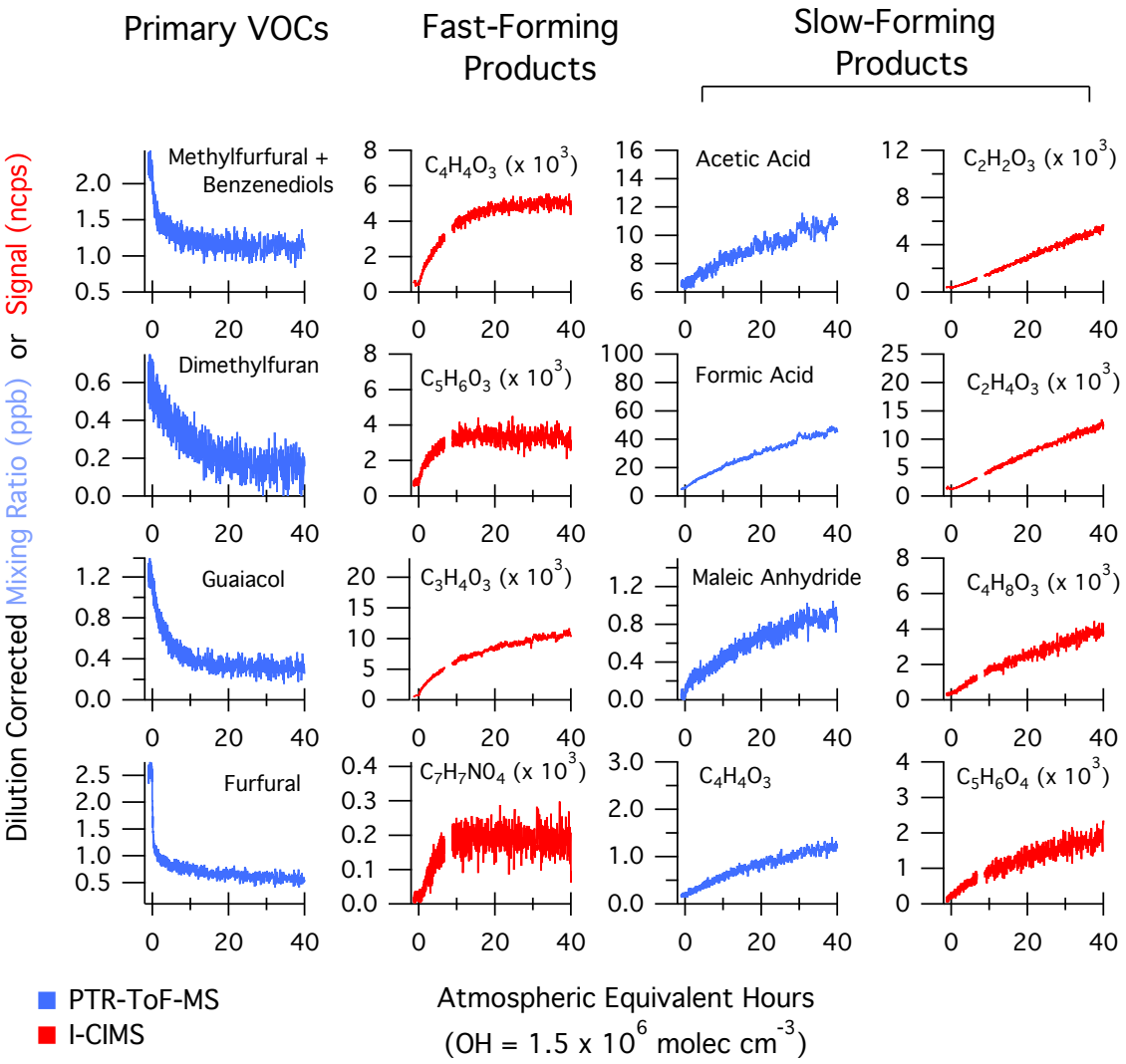

Figure 1. Temporal evolution of select NMOG from the OH oxidation of smoke resulting from Fire 38 (Ponderosa Pine). The data have been dilution-corrected based on the decay of acetonitrile. The time basis is calculated based on the decay of deuterated butanol. The first column shows primary NMOG, the second column illustrates species formed within 20 hrs of atmospheric-equivalent oxidation ("fast-forming" products), while other columns show species formed over longer time scales ("slow-forming" products).

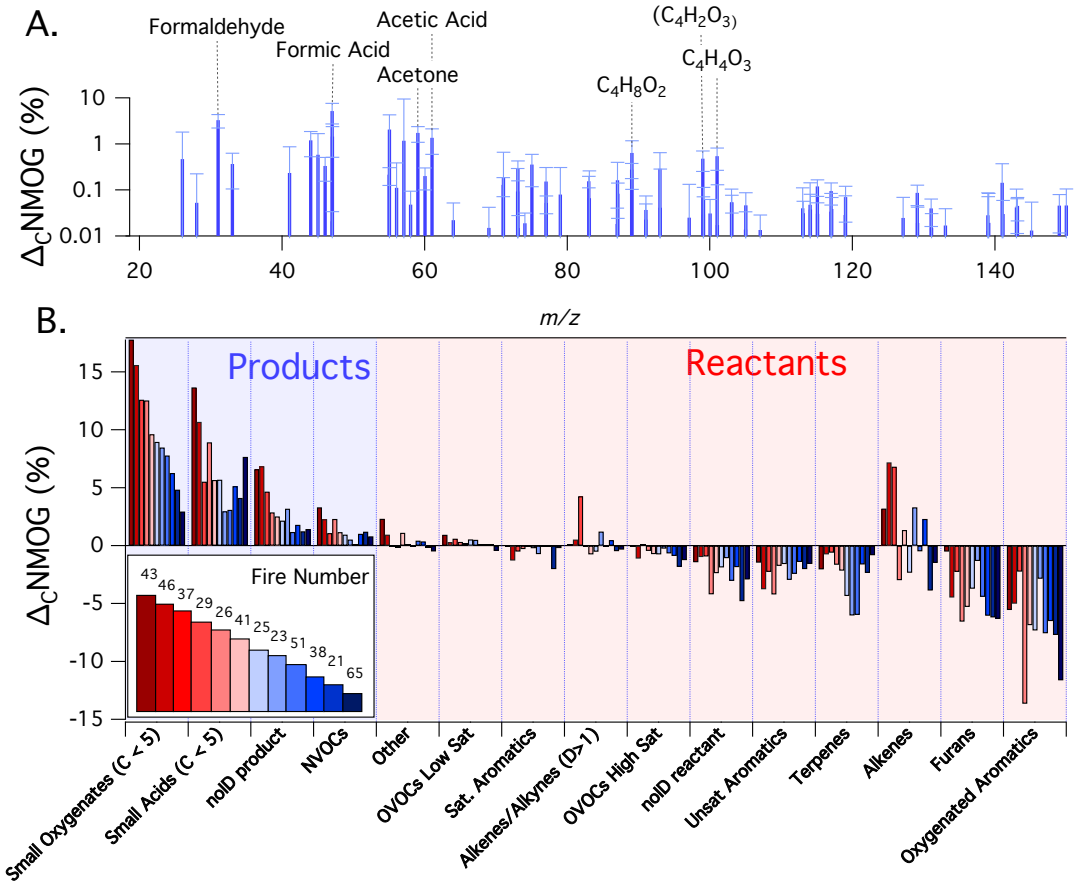

Figure 2. Summary of PTR-ToF-MS measurements during 12 mini chamber experiments. Shown is the amount of initial NMOG carbon (Δ_CNMOG, %) that was consumed (reactant) or formed (product) for a given species after12 hours of atmospheric-equivalent oxidation (OH concentration of 1.5×10^6 molecules cm^{-3}). Panel (A) shows the average speciated distribution of products (error bars are standard deviations). Panel (B) shows Δ_CNMOG for reactants and products as lumped categories. A species is classified as a product if the dilution-corrected signal measured by the PTR-ToF-MS increased after 12 hours of simulated oxidation, and a reactant if the signal decreased. Categories labeled as "no ID" refer to species for which an assignment could not be confidently prescribed. The numbers in the legend refer to the fire number (composition and initial conditions can be found in Fig. S2). Experiments are ordered according to the fraction of primary carbon transformed to measurable secondary NMOG (greatest to least).

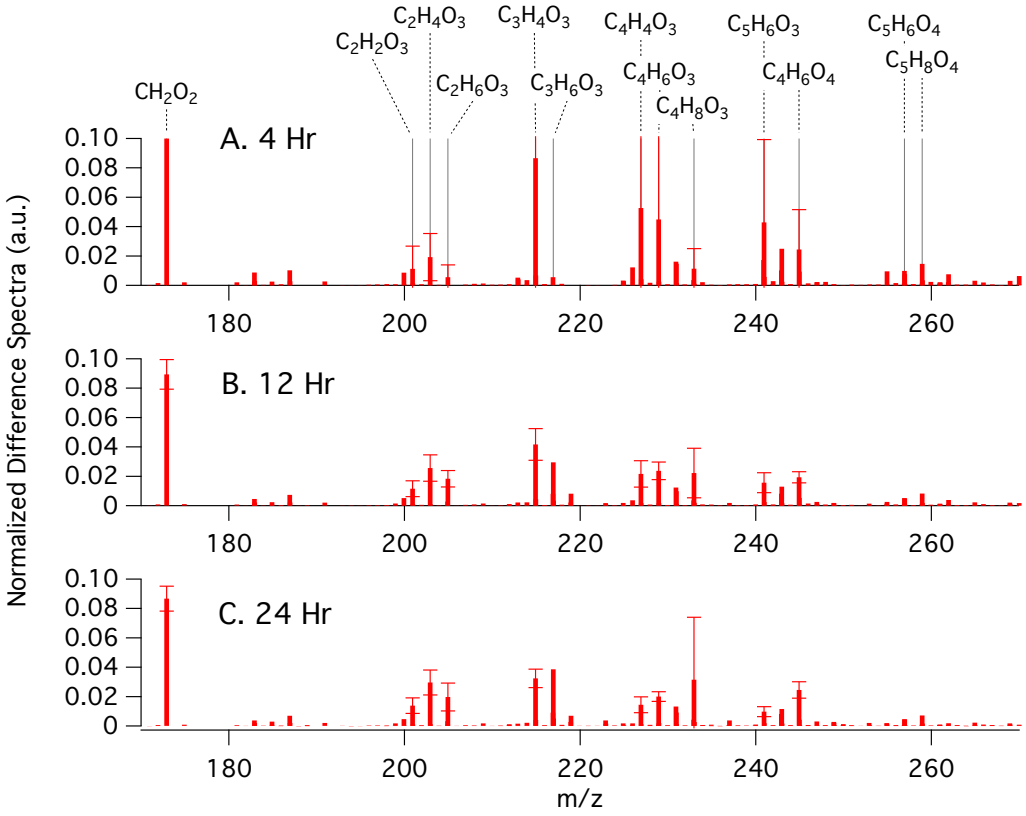

Figure 3. Summary of secondary NMOG measured by I-CIMS during 12 mini chamber experiments. Shown are ion signals that increased after initiating photochemistry relative to the total integrated signal measured prior to photochemistry. Panels (A)-(C) show changes in signal after 4, 12, and 24 hrs of atmospheric-equivalent oxidation, respectively. Error bars represent standard deviations. Note that the masses are presented as I^- adducts.

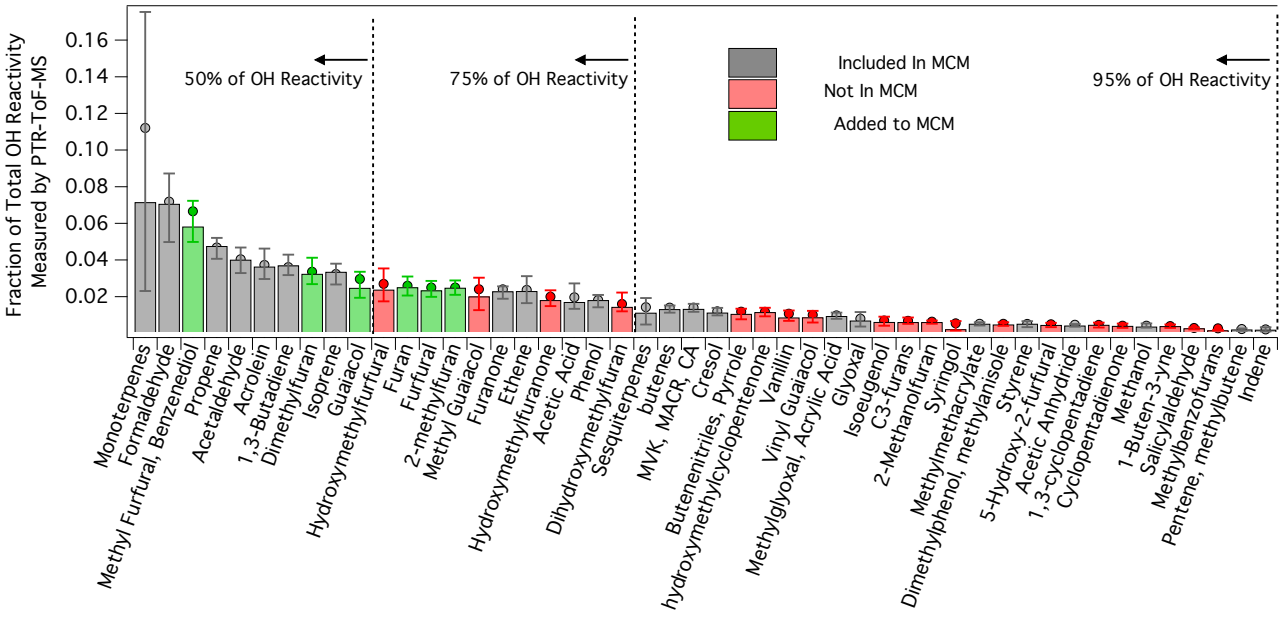

Figure 4. Contribution of individual species to the total primary OH reactivity estimated from PTR-ToF-MS measurements following Equation 2. Bar intensity is median for all burns measured by PTR-ToF-MS, whereas circle markers are averages. Error bars indicate 25^{th} and 75^{th} percentiles. Bar colors indicate if a species is included (grey) or not included (red) in the MCM v. 3.3.1. Green bars indicate OH oxidation mechanisms that were added to the MCM (sub-mechanisms for each species can be found in Figures S4-S9). The concentrations of each species were calculated following the methods described by Koss et al. (2018). Only species that were positively identified are included in these calculations. The assumed OH rate constant for each species is given by Koss et al. (2018).

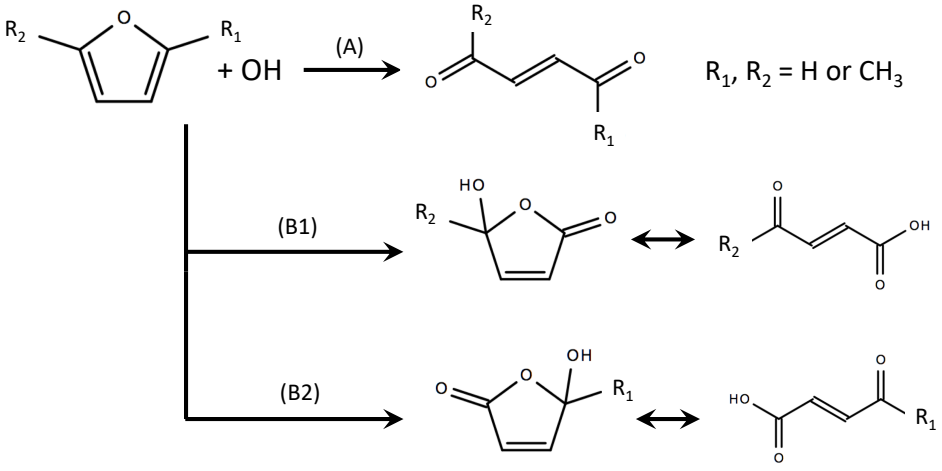

Figure 5. Summary of OH oxidation pathways and final products for furan, 2-methylfuran, and 2,5-dimethylfuran where branch A is the substituent-retention pathway, and branches B1 and B2 are substituent-loss pathways (adapted from Aschmann et al., 2014). In this study, the branching ratios are assumed to be [0.7 (A), 0.3 (B1)] for furan, [0.31 (A), 0.39 (B1), 0.31 (B2)] for 2-methylfuran, and [0.27 (A), 0.73 (B1)] for 2,5-dimethylfuran. Details of the assumed RO_2 reaction schemes are provided in Figures S4 - S6.

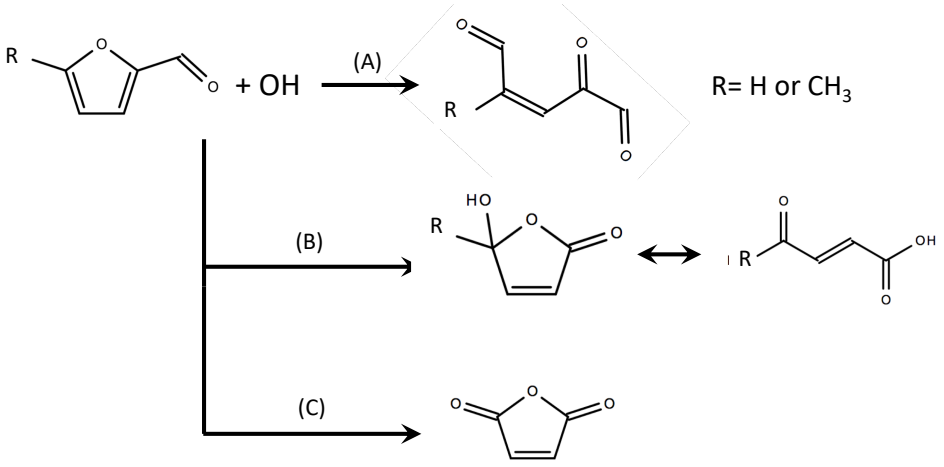

Figure 6. Summary of OH oxidation pathways and final products for furfural and 5-methylfurfural, where branch A is the substituent-retention pathway, and branches B and C are substituent-loss pathways (adapted from Zhao and Wang, 2017). The branching ratios estimated by Zhao and Wang (2017) are 0.37 for channel A, 0.6 for channel B, and 0.03 for channel C. Details of the assumed RO_2 reaction schemes are provided in Figures S7 - S9.

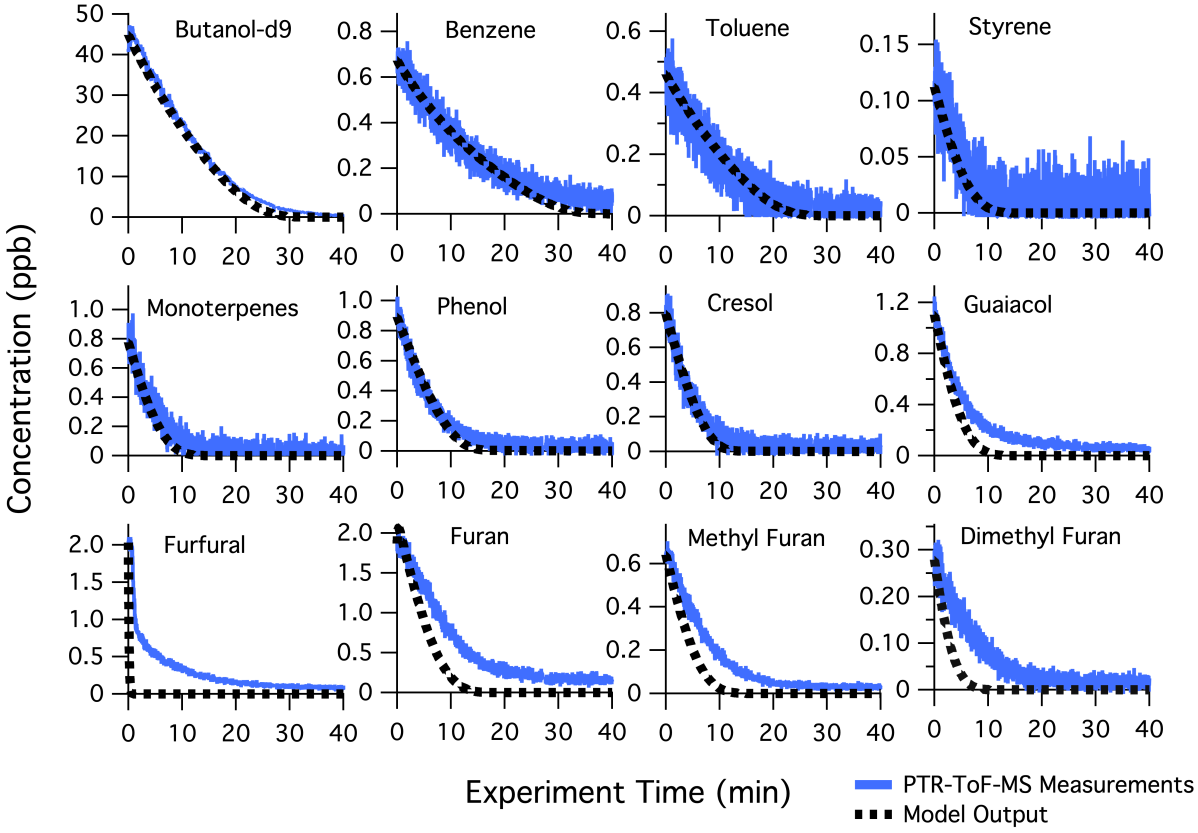

Figure 7. Primary NMOG measurements (blue lines) compared to modeled output (black dotted lines) for Fire 38. The decay of butanol-d9 is shown to demonstrate model performance in reproducing OH exposures, which was achieved by adjusted the measured photon flux by a factor of 1.5. Fuel = Ponderosa Pine Litter, NO_x/NMOG = 0.3, mixture of high and low-temperature pyrolysis products.

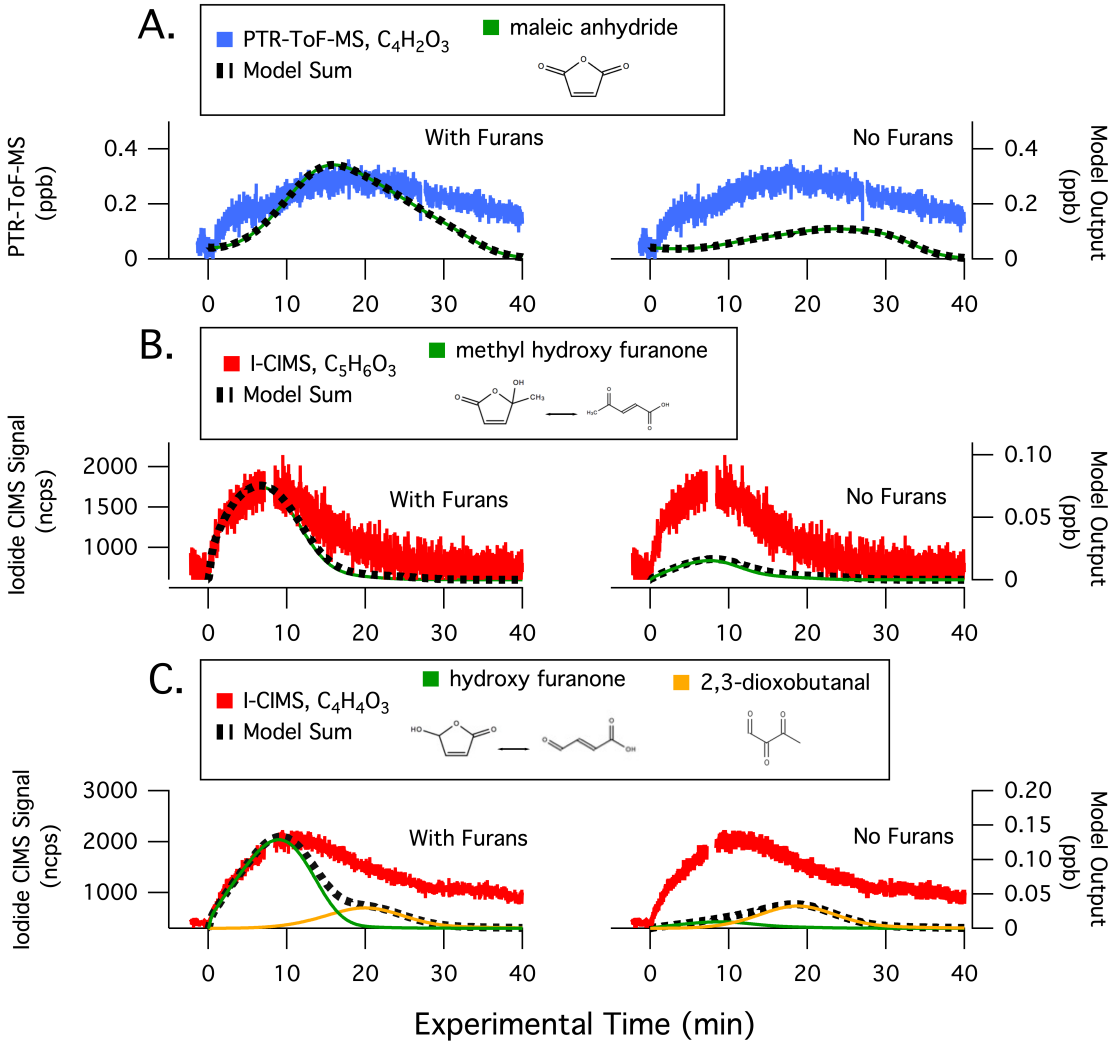

Figure 8. Secondary NMOG measurements compared to modeled output for Fire 38. Row (A) shows PTR-ToF-MS measurements of $C_4H_2O_3$ compared to model output of maleic anhydride. Row (B) shows I^--ToF-CIMS measurements of $C_5H_6O_3$ compared to model output of methyl hydroxy furanone and its tautomer, β-acetylacrylic acid. Row (C) shows I^--ToF-CIMS measurements of $C_4H_4O_3$ compared to model output of hydroxy furanone, its tautomer malealdehydic acid, and 2,3-dioxobutanal. All graphs to the left show full model runs, while graphs to the right show model runs when the initial conditions of furan, 2-methylfuran, 2,5-dimethylfuran, furfural, 5-methylfurfural, and furanone are set to zero.

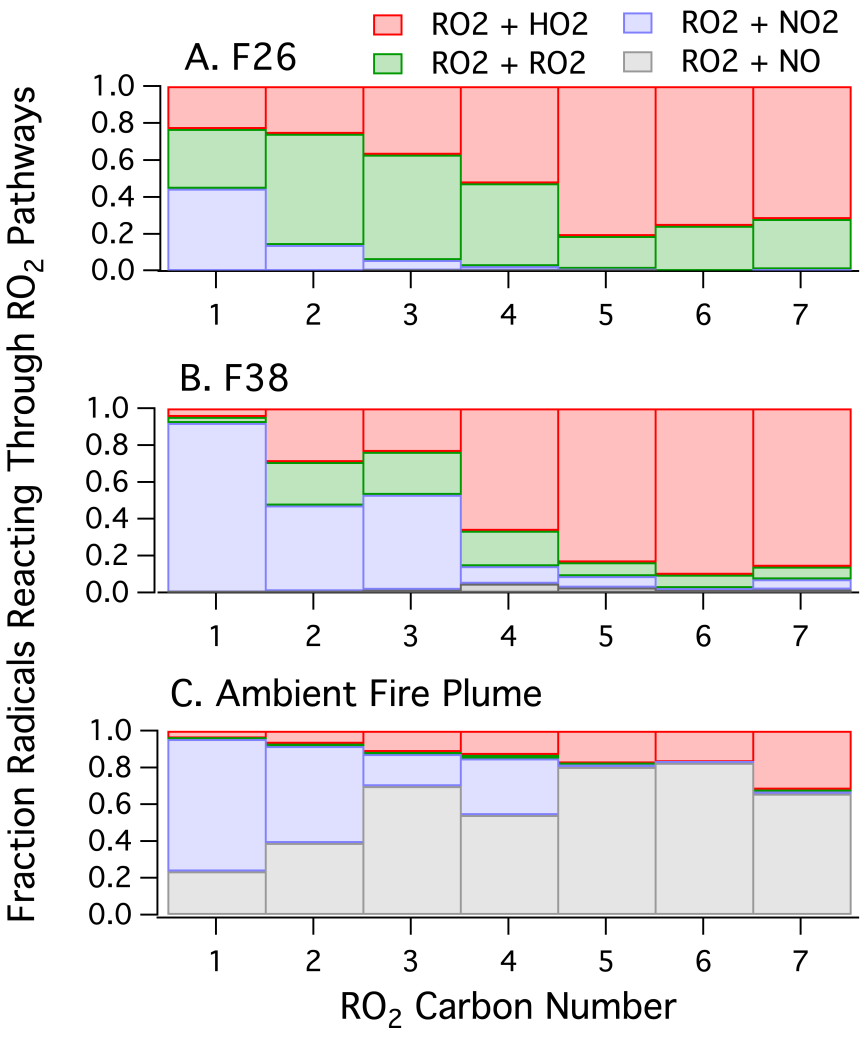

Figure 9. The fate of RO_2 species for (A) F26, (B) F38, and (C) the ambient biomass burning plume described by Müller et al. (2016). RO_2 species are grouped by carbon number, and the color of each bar shows the fraction of RO_2 species reacted by RO_2 + HO_2, RO_2 + RO2, RO_2 + NO_2, and RO_2 + NO pathways.

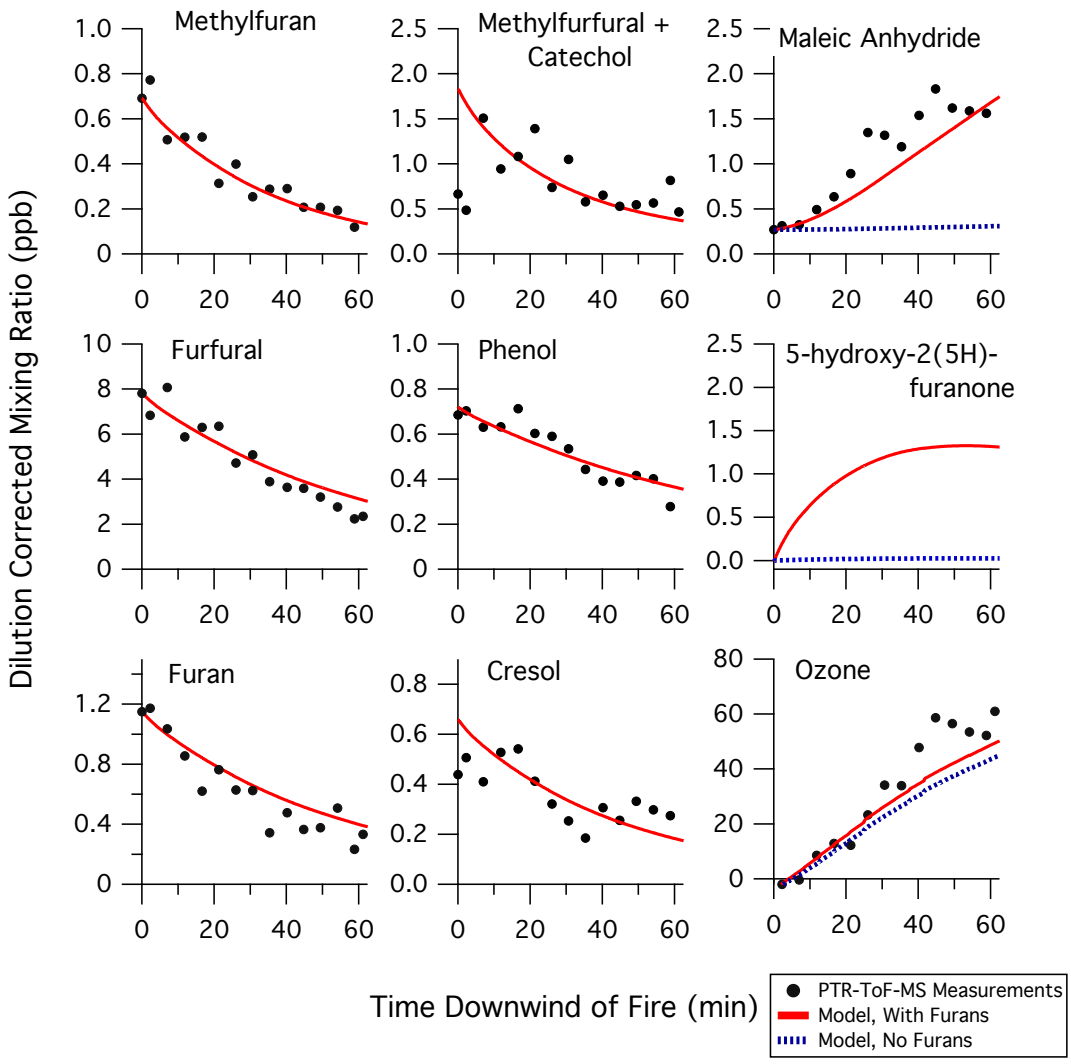

Figure 10. Summary of model results for the understory fire described by Müller et al. (2016). Data are presented as mixing ratios corrected for dilution (calculated based on the decay of CO). The initial conditions for methylfurfural + catechol and cresol were adjusted to best match the observed decay. Results with furans excluded from the model are shown as dotted lines. Maleic anhydride and ozone are shown to illustrate the impact of furans on secondary product formation.

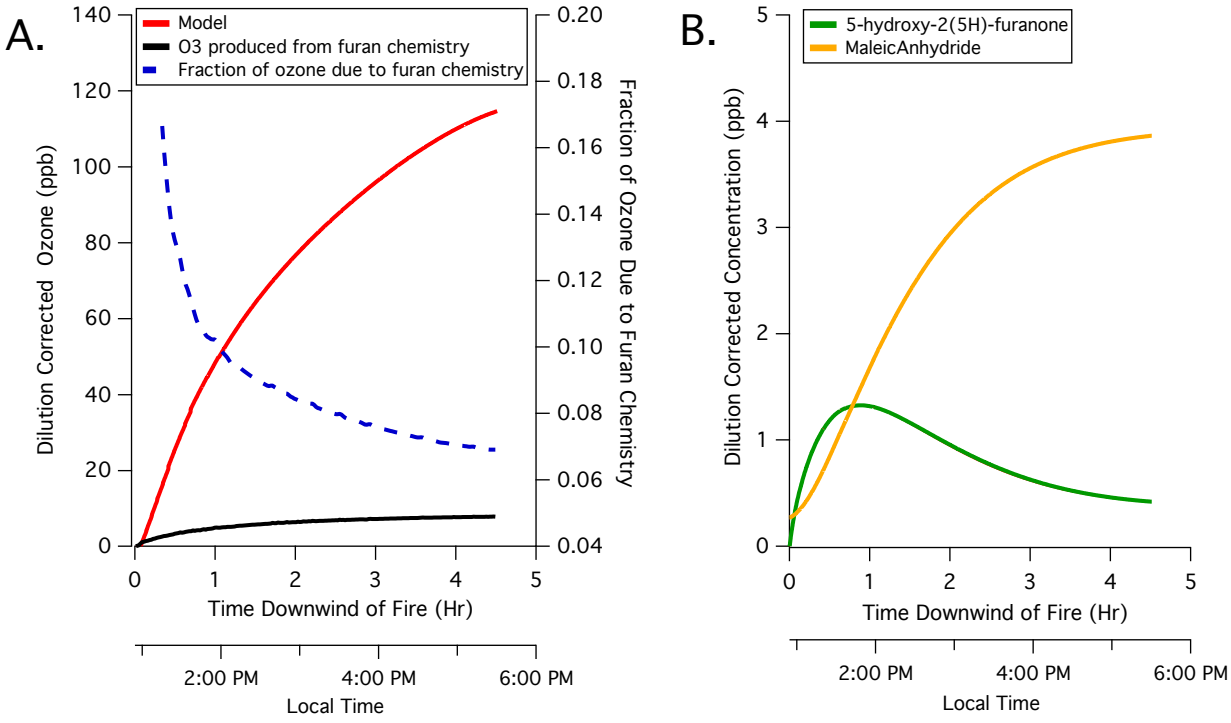

Figure 11. A. Total ozone, estimated ozone produced by furan chemistry, and fraction of total ozone associated with furan chemistry for the modeled biomass burning plume measured by Müller et al. (2016). B. Model predictions of 5-hydroxy-2(5H)-furanone and maleic anhydride production. Shown is an extrapolation of the 1 hr model described in Section 3.2.4. After 10 minutes of oxidation, furan chemistry is responsible for $>$ 15% of total ozone production in the model. The predicted contribution from furan chemistry decreases as furans are consumed and other, slower-reacting primary NMOG begin to oxidize. Furan chemistry contributes $\sim$ 8 ppb of ozone after 4.5 hr of oxidation.

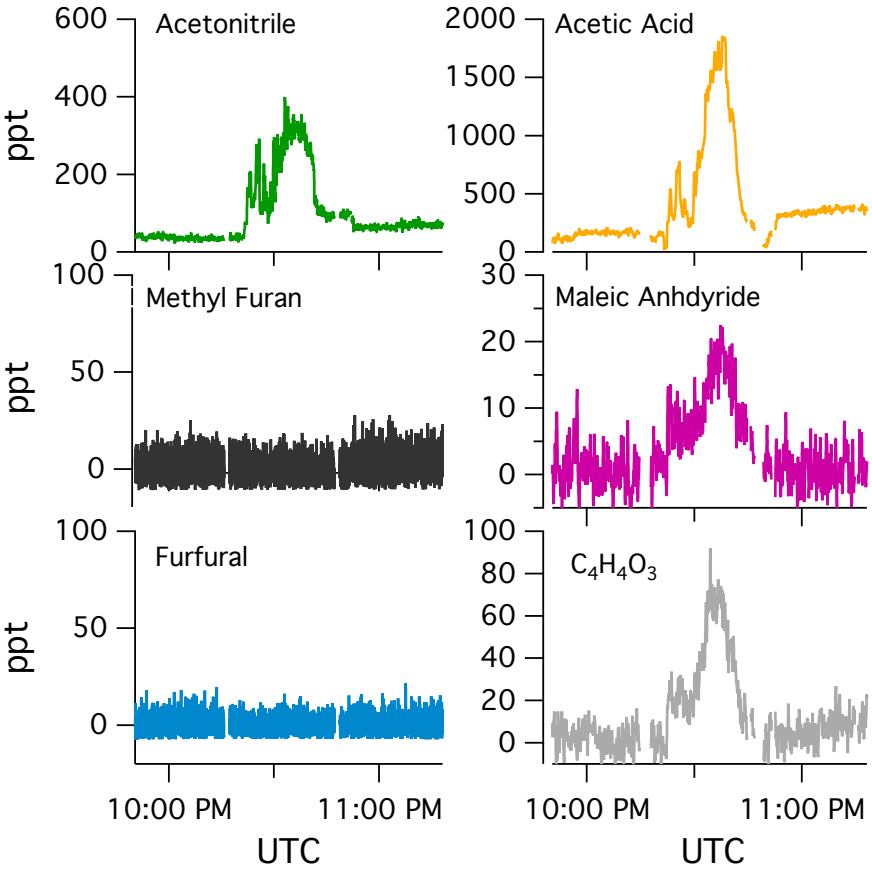

Figure 12. PTR-ToF-MS measurements of a wild fire plume transported to the U.S. from southern Siberia. The plume was intercepted April 21, 2015 during the SONGNEX field campaign and is described in detail by Baylon et al. (2017).

OH-chemistry of non-methane organic gases (NMOG) emitted from laboratory and ambient biomass burning smoke: evaluating the influence of furans and oxygenated aromatics on ozone and secondary NMOG formation.

Matthew M. Coggon[1,2], Christopher Y. Lim[3], Abigail R. Koss[1,2,‡], Kanako Sekimoto[1,2,4], Bin Yuan[1,2,†], Jessica B Gilman[2], David H. Hagan[3], Vanessa Selimovic[5], Kyle J. Zarzana[1,2,§], Steven S. Brown[2], James M. Roberts[2], Markus Müller[6], Robert Yokelson[5], Armin Wisthaler[7,8], Jordan E. Krechmer[9], Jose L. Jimenez[1,10], Christopher Cappa[11], Jesse H. Kroll[3], Joost de Gouw[1,10], and Carsten Warneke[1,2]

[1]Cooperative Institute for Research in Environmental Sciences, University of Colorado, Boulder, CO, USA
[2]NOAA Earth Systems Research Laboratory Chemical Sciences Division, Boulder, CO, USA
[3]Department of Civil and Environmental Engineering, Massachusetts Institute of Technology, Cambridge, MA, USA
[4]Graduate School of Nanobioscience, Yokohama City University, Yokohama, Kanagawa, Japan
[5]Department of Chemistry and Biochemistry, University of Montana, Missoula, MT, USA
[6]Ionicon Analytik, Innsbruck, Austria
[7]Institute for Ion Physics and Applied Physics, University of Innsbruck, Innsbruck , Austria
[8]Department of Chemistry, University of Oslo, Oslo, Norway
[9]Aerodyne Research, Inc., Billerica, MA, USA
[10]Department of Chemistry, University of Colorado, Boulder, CO, USA
[11]Department of Civil and Environmental Engineering, University of California, Davis, CA, USA
[‡]now Tofwerk A.G., Boulder, CO, USA
[†]now at Institute for Environment and Climate Research, Jinan University, Guangzhou, China.
[§]now at Department of Chemistry, University of Colorado Boulder, Boulder, CO, USA

Correspondence: Matthew Coggon (matthew.m.coggon@noaa.gov), Carsten Warneke (carsten.warneke@noaa.gov)

1 Evaluating NOMOG Losses Through Metal Ductwork

As described in the main text, smoke was passed through metal ductwork before injection to the mini chamber. Deming et al. (2019) showed that surface partitioning is dependent on NMOG volatility, functionality, and displacement processes at adsorption sites. Prior to each small chamber experiment, the PTR-ToF-MS sampled NMOG directly from the stack, as described by Koss et al. (2018). To evaluate biases associated with NMOG transmission through the ductwork, we compare the distribution of NMOG measured from the stack with that inside the small chamber prior to the initiation of OH chemistry. Figure S15 shows the difference in NMOG profiles between small chamber and stack measurements (Small Chamber Bias = $[\mathrm{NMOG_i}/\mathrm{CH_3CN}]_{\mathrm{chamber}}$ - $[\mathrm{NMOG_i}/\mathrm{CH_3CN}]_{\mathrm{stack}}$). We normalize the NMOG distribution to $\mathrm{CH_3CN}$ under the assumption the acetonitrile is not lost to surfaces to a greater degree than other NMOG. The top row shows bias histograms for three fires, while the bottom row shows a comparison between the normalized profiles with 1:1, 1:2, and 2:1 lines.

In general, most NMOG fall within 20% of the 1:1 line. Bias histograms (top row, Fig. S15) show that the NMOG/CH_3CN ratios are lower in the small chamber, which suggests that NMOG are lost to the ductwork; however, this loss appears to be normally distributed and not weighted towards any specific NMOG functionality. Some masses exhibit significantly higher ratios with acetonitrile inside the small chamber (e.g. butenes, ethanol, formamide for F29); however, PTR-ToF-MS detection of these masses is poor due to contributions of fragments from higher masses (e.g. butene), or low sensitivity (e.g. ethanol).

Fig. S15 demonstrates that the relative NMOG distribution in the chamber is not significantly different from the NMOG distribution sampled from the stack. These results are consistent with the conclusions drawn by Lim et al. (2019), which showed that the volatility distribution was not significantly different between stack and mini chamber measurements.

2 Sensitivity of Modeled Secondary NMOG Formation to Furfural Branching Ratios

The reactions employed to represent furfural oxidation were estimated by Zhao and Wang (2017) via theoretical quantum chemistry calculations. To date, this mechanism has not been studied experimentally; consequently, the exact branching ratios of the three major pathways may differ from those used in this study (0.37 for channel A, 0.6 for channel B, and 0.03 for channel C, 6). Furfural plays a major role in the formation of secondary NMOG measured in the biomass burning plume described by Müller et al. (2016) and the assumed branching ratios may impact modeled formation of maleic anhydride, hydroxy furanone, and ozone.

Figure S16 shows model output of maleic anhydride, hydroxy furanone, and ozone for base case (A = 0.37, B = 0.6, B = 0.03), equal weight (0.33, 0.33, 0.33), and isolated channel (i.e., all channel A, B, or C) simulations of the biomass burning plume described by Müller et al. (2016). Overall, hydroxy furanone formation is most sensitive to the assumed branching ratio of channel B, which is the pathway that directly leads to hydroxy furanone formation (Fig. 6). Maleic anhydride is most sensitive to the assumed branching ratio of channel C; however, this sensitivity is weaker than that of hydroxy furanone since all pathways lead to a significant yield of maleic anhyride. The assumed branching ratios have little impact on ozone formation.

The sensitivity tests presented in Fig. S16 demonstrate the need for experimental evaluation of the furfural oxidation mechanism. This refinement may provide better constraints of important secondary NMOG; however, this will unlikely affect modeled ozone formation.

References

Aschmann, S. M., Nishino, N., Arey, J., and Atkinson, R.: Products of the OH Radical-Initiated Reactions of Furan, 2- and 3-Methylfuran, and 2,3- and 2,5-Dimethylfuran in the Presence of NO, J. Phys. Chem. A., 118, 457–466, 2014.

Atkinson, R., Baulch, D. L., Cox, R. A., Crowley, J. N., Hampson, R. F., Hynes, R. G., Jenkin, M. E., Rossi, M. J., Troe, J., and Subcommittee, I.: Evaluated kinetic and photochemical data for atmospheric chemistry: Volume II — gas phase reactions of organic species, Atmospheric Chemistry and Physics, 6, 3625–4055, https://doi.org/10.5194/acp-6-3625-2006, 2006.

Burkholder, J., Sander, S., Abbatt, J., Barker, J., Huie, R., Kolb, C., Kurylo, M., Orkin, V., Wilmouth, D., and Wine, P.: Chemical Kinetics and Photochemical Data for Use in Atmospheric Studies, Evluation No. 18, Jet Propulsion Laboratory, Pasadena, CA, 2015.

Deming, B., Pagonis, D., Liu, X., Day, D., Talukdar, R., Krechmer, J., de Gouw, J. A., Jimenez, J. L., and Ziemann, P. J.: Measurements of Delays of Gas-Phase Compounds in a Wide Variety of Tubing Materials due to Gas-Wall Interactions, Atmospheric Measurement Techniques Discussions, 2019, 1–19, https://doi.org/10.5194/amt-2019-25, https://www.atmos-meas-tech-discuss.net/amt-2019-25/, 2019.

Keller-Rudek, H., Moortgat, G. K., Sander, R., and Sörensen, R.: The MPI-Mainz UV/VIS Spectral Atlas of Gaseous Molecules of Atmospheric Interest, Earth System Science Data, 5, 365–373, https://doi.org/10.5194/essd-5-365-2013, https://www.earth-syst-sci-data.net/5/365/2013/, 2013.

Koss, A. R., Sekimoto, K., Gilman, J. B., Selimovic, V., Coggon, M. M., Zarzana, K. J., Yuan, B., Lerner, B. M., Brown, S. S., Jimenez, J. L., Krechmer, J., Roberts, J. M., Warneke, C., Yokelson, R. J., and de Gouw, J.: Non-methane organic gas emissions from biomass burning: identification, quantification, and emission factors from PTR-ToF during the FIREX 2016 laboratory experiment, Atmospheric Chemistry and Physics, 18, 3299–3319, https://doi.org/10.5194/acp-18-3299-2018, 2018.

Lauraguais, A., Coeur-Tourneur, C., Cassez, A., Deboudt, K., Fourmentin, M., and Choël, M.: Atmospheric reactivity of hydroxyl radicals with guaiacol (2-methoxyphenol), a biomass burning emitted compound: Secondary organic aerosol formation and gas-phase oxidation products, Atmospheric Environment, 86, 155–163, 2014.

Lim, C., Hagan, D., Cappa, C., Coggon, M. M., Koss, A. R., Sekimoto, K., de Gouw, J., Warneke, C., and Kroll, J.: Secondary organic aerosol formation from biomass burning emissions, in prep, 2019.

Müller, M., Anderson, B. E., Beyersdorf, A. J., Crawford, J. H., Diskin, G. S., Eichler, P., Fried, A., Keutsch, F. N., Mikoviny, T., Thornhill, K. L., Walega, J. G., Weinheimer, A. J., Yang, M., Yokelson, R. J., and Wisthaler, A.: In situ measurements and modeling of reactive trace gases in a small biomass burning plume, Atmospheric Chemistry and Physics, 16, 3813–3824, 2016.

Sekimoto, K., Li, S.-M., Yuan, B., Koss, A., Coggon, M., Warneke, C., and de Gouw, J.: Calculation of the sensitivity of proton-transfer-reaction mass spectrometry (PTR-MS) for organic trace gases using molecular properties, International Journal of Mass Spectrometry, 421, 71–94, 2017.

Wolfe, G. M., Crounse, J. D., Parrish, J. D., St. Clair, J. M., Beaver, M. R., Paulot, F., Yoon, T. P., Wennberg, P. O., and Keutsch, F. N.: Photolysis, OH reactivity and ozone reactivity of a proxy for isoprene-derived hydroperoxyenals (HPALDs), Phys. Chem. Chem. Phys., 14, 7276–7286, https://doi.org/10.1039/C2CP40388A, 2012.

Zhao, X. and Wang, L.: Atmospheric Oxidation Mechanism of Furfural Initiated by Hydroxyl Radicals, J. Phys. Chem. A., 121, 3247–3253, 2017.

Table S1. References and calculated photolysis frequencies for reactions used in the MCM v 3.3.1 during mini-chamber experiments. Photolysis frequencies are calculated as the product of the absorption cross section, quantum yield, and the scaled photon flux at 254 nm (4.5×10^{15} photons cm^2). The ratio to j_{NO2} is shown for ease of comparison.

Absorbing Species	MCM Reaction	MCM Name	Value (s^{-1})	j / j_{NO2}	Cross Section Database	Quantum Yield Ref.	QY (254 nm)
ozone	O3 → O1D	J1	4.5E-02	885.38	JPL	JPL	0.9
ozone	O3 → O	J2	5.0E-03	98.38	JPL	JPL	0.1
hydrogen peroxide	H2O2 → OH + OH	J3	3.0E-04	6.03	JPL	JPL	1
nitrogen dioxide	NO2 → NO + O	J4	5.0E-05	1.00	IUPAC	IUPAC	1
nitrate radical	NO3 → NO2 + O	J5	4.9E-04	9.79	Mainz	JPL	1
nitrate radical	NO3 → NO	J6	0	0	Mainz	JPL	0
nitrous acid	HONO → OH + NO	J7	5.9E-04	11.70	IUPAC	IUPAC	1
nitric acid	HNO3 → OH + NO2	J8	8.5E-05	1.68	JPL	IUPAC	1
formaldehyde	HCHO → CO + HO2 + HO2	J11	4.5E-06	0.09	JPL	JPL	0.3
formaldehyde	HCHO → H2 + CO	J12	7.5E-06	0.15	IUPAC	JPL	0.5
acetaldehyde[1]	CH3CHO → CH3O2 + HO2 + CO	J13	2.0E-05	0.39	IUPAC	IUPAC	0.3
propanal	C2H5CHO → C2H5O2 + HO2 + CO	J14	7.6E-05	1.50	IUPAC	IUPAC	1
butanal[2]	C3H7CHO → NC3H7O2 + CO + HO2	J15	1.3E-05	0.26	IUPAC	IUPAC	0.21
butanal	C3H7CHO → C2H4 +CH3CHO	J16	6.3E-06	0.12	IUPAC	IUPAC	0.1
2-methylpropanal	IPRCHO → IC3H7O2 + HO2 + CO	J17	1.4E-05	0.27	IUPAC	IUPAC	0.25
methacrolein[2]	MACR → CH3C2H2O2 + CO + HO2	J18	3.9E-07	0.01	IUPAC	JPL	0.05
methacrolein	MACR → MACO3 + HO2	J19	3.9E-07	0.01	IUPAC	JPL	0.05
(C5)-HPALD	C5HPALD1 → products	J20	7.7E-06	0.15	IUPAC	Wolfe et al. (2012)	1
	C5HPALD2 → products						
acetone[1]	CH3COCH3 → CH3CO3 + CH3O2	J21	5.6E-05	1.11	IUPAC	IUPAC	0.42
methyl ethyl ketone	MEK → CH3CO3 + C2H5O2	J22	4.6E-05	0.90	IUPAC	IUPAC	0.34
methyl vinyl ketone	MVK → C3H6 + CO	J23	4.0E-06	0.08	IUPAC	IUPAC	0.38
methyl vinyl ketone	MVK → CH3CO3 + HCHO + CO + HO2	J24	4.0E-06	0.08	IUPAC	IUPAC	0.38
glyoxal	GLYOX → CO + CO + H2	J31	3.6E-05	0.71	JPL	JPL	0.52
glyoxal	GLYOX → HCHO + CO	J32	2.3E-05	0.45	JPL	JPL	0.33
glyoxal	GLYOX → CO + CO + HO2 + HO2	J33	1.1E-05	0.21	JPL	JPL	0.16
methyl glyoxal	MGLYOX → CH3CO3 + CO + HO2	J34	1.2E-04	2.37	JPL	JPL	1
biacetyl	BIACET → CH3CO3 + CH3CO3	J35	2.6E-05	0.51	IUPAC	IUPAC	0.158
methyl hydroperoxide	CH3OOH → CH3O + OH	J41	1.5E-04	2.90	IUPAC	IUPAC	1
methyl nitrate	CH3NO3 → CH3O + NO2	J51	1.5E-04	2.88	IUPAC	IUPAC	1
ethyl nitrate	C2H5NO3 → C2H5O + NO2	J52	1.8E-04	3.59	IUPAC	IUPAC	1
propyl nitrate	NC3H7NO3 → NC3H7O + NO2	J53	1.9E-04	3.85	IUPAC	IUPAC	1
isopropyl nitrate	IC3H7NO3 → IC3H7O + NO2	J54	2.2E-04	4.30	IUPAC	IUPAC	1

JPL - Burkholder et al. (2015) (https://jpldataeval.jpl.nasa.gov/)

IUPAC - Atkinson et al. (2006) (http://iupac.pole-ether.fr/index.html)

Mainz - Keller-Rudek et al. (2013) (www.uv-vis-spectral-atlas-mainz.org)

[1] Additional photolysis rections added to account for losses at 254 nm (see Table S2)

[2] No Data for QY available at 254 nm; assume highest value reported at higher wavelengths

Table S2. Same as Table S1, but for reactions that are likely to be important in the mini-chamber that are not represented in MCM v 3.3.1.

Absorbing Species	MCM Reaction	MCM Name	Value (s^{-1})	j / j_{NO2}	Cross Section Database	Quantum Yield Ref.	QY (254 nm)
benzaldehyde	BENZAL → HO2 + C6H5CO3	Jn2	1.1E-03	21.30	IUPAC	IUPAC	0.3
	BENZAL → HO2 + CO + C6H5O2						
acetaldehyde	CH3CHO → CH4 + CO	Jn5	3.0E-05	0.60	IUPAC	IUPAC	0.46
acetaldehyde	CH3CHO → CH3CO3 + HO2	Jn6	7.9E-06	0.16	IUPAC	IUPAC	0.12
2-furfural	FURFURAL → FURAN + CO	Jn7	1.3E-01	2646.26	Mainz	Estimate[1]	0.6
	FURFURAL → C3H4 + CO + CO						
acetone	CH3COCH3 → CH3O2 + CH3O2 + CO	Jn8	2.7E-05	0.53	IUPAC	IUPAC	0.2
peroxyacetyl nitrate	PAN → CH3CO3 + NO2	Jn14	3.2E-04	6.41	IUPAC	IUPAC	0.745
peroxyacetyl nitrate	PAN → CH3O2 + NO3	Jn15	1.1E-04	2.23	IUPAC	IUPAC	0.26
methoxy nitrate	CH3O2NO2 → CH3O2 + NO2	Jn16	1.4E-03	27.26	IUPAC	Estimate	0.95
methoxy nitrate	CH3O2NO2 → CH3O + NO3	Jn17	7.2E-05	1.43	IUPAC	Estimate	0.05
dinitrogen pentoxide	N2O5 → NO3 + NO2	Jn19	2.8E-04	5.58	IUPAC	IUPAC	0.2
dinitrogen pentoxide	N2O5 → NO3 + NO + O	Jn20	8.8E-04	17.51	IUPAC	IUPAC	0.6
HO2NO2	HO2NO2 → HO2 + NO2	Jn21	9.2E-04	18.32	IUPAC	IUPAC	0.59
HO2NO2	HO2NO2 → OH + NO3	Jn22	6.4E-04	12.73	IUPAC	IUPAC	0.41

JPL - Burkholder et al. (2015) (https://jpldataeval.jpl.nasa.gov/)

IUPAC - Atkinson et al. (2006) (http://iupac.pole-ether.fr/index.html)

Mainz - Keller-Rudek et al. (2013) (www.uv-vis-spectral-atlas-mainz.org)

[1] Personal communication with V. Papadimitriou

Table S3. Rate constant parameters, photolysis frequency, and initial conditions for the species modeled in F26 and F38. Entries are ordered by mixing ratios measured during F38. Photolysis frequencies are calculated based on literature cross-sections, known/estimated quantum yields, and the scaled photon flux at 254 nm (4.5×10^{15} photons cm^2).

	MCM Name	k_{OH} (cm^3 $molec^{-1}$ s^{-1})	k_{O3} (cm^3 $molec^{-1}$ s^{-1})	k_{NO3} (cm^3 $molec^{-1}$ s^{-1})	j (s^{-1})	F26 (ppb)	F38 (ppb)
Butanol-d9	DBUTANOL	3.40E-12	0	0	0	37.26	44.86
Formaldehyde	HCHO	8.47E-12	0	5.50E-16	1.20E-05	14.07	17.84
1-butene	BUT1ENE	3.11E-11	1.06E-17	1.35E-14	0	4.53	13.84
Methanol	CH3OH	9.02E-13	0	0	0	22.23	11.79
Ethene	C2H4	7.74E-12	1.68E-18	2.24E-16	0	9.22	8.38
Acetaldehyde	CH3CHO	1.48E-11	0	2.84E-15	1.98E-05	15.44	7.86
Acetic Acid	CH3CO2H	8.00E-13	0	0	0	7.64	6.03
Ethyne	C2H2	7.46E-13	0	0	0	4.97	5.96
Formic Acid	HCOOH	4.50E-13	0	0	0	3.89	4.86
Acrolein	ACR	2.00E-11	2.90E-19	3.26E-15	3.86E-07	3.24	4.43
1-propene	C3H6	2.83E-11	1.04E-17	9.79E-15	0	7.52	2.64
2-furfural	FURFURAL	3.50E-11	0	0	1.34E-01	2.07	2.03
Acetone	CH3COCH3	1.78E-13	0	0	8.3E-05	5.60	1.95
Furan	FURAN	4.20E-11	0	0	0	2.26	1.87
Furanone	BZFUONE	4.45E-11	2.20E-19	3.00E-13	0	1.77	1.73
2,3-butanedione	BIACET	2.41E-13	0	0	2.55E-05	2.09	1.66
1,3-butadiene	C4H6	6.59E-11	6.64E-18	1.03E-13	0	2.40	1.42
Ethanol	C2H5OH	3.21E-12	0	0	0	1.63	1.34
Glyoxal	GLYOX	9.63E-12	0	2.84E-15	6.95E-05	0.98	1.25
Hydroxyacetone	ACETOL	4.42E-12	0	0	4.55E-05	1.30	1.12
Guaiacol	GUAIACOL	7.44E-11	0	0	0	2.94	1.10
5-methylfurfural	MEFURFURAL	5.10E-11	0	0	0	1.45	1.00
Catechol	CATECHOL	1.00E-10	9.20E-18	9.90E-11	0	1.45	1.00
Phenol	PHENOL	2.74E-11	0	3.80E-12	0	2.39	0.89
Methyl acetate	METHACET	3.50E-13	0	0	0	1.03	0.89
Propenoic acid	ACO2H	8.66E-12	0	0	0	0.87	0.86
Methyl vinyl ketone	MVK	1.99E-11	5.36E-18	0	8.06E-06	0.99	0.81

Table S3. (Continued)

	MCM Name	k_{OH} (cm^3 $molec^{-1}$ s^{-1})	k_{O3} (cm^3 $molec^{-1}$ s^{-1})	k_{NO3} (cm^3 $molec^{-1}$ s^{-1})	j (s^{-1})	F26 (ppb)	F38 (ppb)
o-cresol	CRESOL	4.65E-11	0	1.40E-11	0	2.58	0.79
alpha-pinene	APINENE	5.20E-11	9.53E-17	6.15E-12	0	0.76	0.78
Methyl glyoxal	MGLYOX	1.29E-11	0	6.82E-15	1.20E-04	0.69	0.69
Benzene	BENZENE	1.22E-12	0	0	0	1.93	0.67
2-methylfuran	MEFURAN	6.19E-11	0	0	0	1.35	0.64
Toluene	TOLUENE	5.59E-12	0	0	0	1.90	0.46
Isoprene	C5H8	9.91E-11	1.33E-17	7.03E-13	0	1.04	0.42
Methyl ethyl ketone	MEK	1.11E-12	0	0	4.55E-05	1.47	0.41
Acetic Anhydride	METHCOACET	1.00E-14	0	0	0	0.33	0.30
p-benzoquinone	PBZQONE	4.60E-12	0	3.00E-13	0	0.24	0.30
2,5-dimethylfuran	DIMEFURAN	1.32E-10	0	0	0	0.75	0.28
Methacrolein	MACR	2.84E-11	1.28E-18	3.40E-15	7.72E-07	0.29	0.24
Benzaldehyde	BENZAL	1.25E-11	0	2.40E-15	1.1E-3	0.28	0.19
2,3-dimethyl phenol	OXYLOL	8.00E-11	0	3.20E-11	0	0.71	0.16
Propenal	C4ALDB	3.40E-11	1.58E-18	6.00E-15	5.56E-07	0.18	0.15
Styrene	STYRENE	5.80E-11	1.70E-17	1.50E-12	0	0.36	0.11
1-pentene	PENT1ENE	3.10E-11	1.00E-17	1.20E-14	0	0.34	0.10
m-xylene	MXYL	2.31E-11	0	2.60E-16	0	0.26	0.09
p-xylene	PXYL	1.43E-11	0	5.00E-16	0	0.26	0.09
o-xylene	OXYL	1.36E-11	0	4.10E-16	0	0.17	0.06
Ethyl benzene	EBENZ	7.00E-12	0	1.20E-16	0	0.08	0.03
NO2	NO2	9.22E-12	3.72E-17	1.21E-12	5.05E-05	6.46	53.98
O3	O3	7.41E-14	4.96E-02	0	0	5.00	10.00
HONO	HONO	5.95E-12	0	0	5.90E-04	0.00	2.58
NO	NO	8.97E-12	1.78E-14	2.60E-11	0	0.08	0.40

Table S4. Calculated NMOG losses by reaction with OH, O_3, NO_3, and photolysis for F26, F38, and the ambient biomass burning plume described by Müller et al. (2016). All values are percentages of the integrated loss over 15 hr of atmospheric-equivalent OH oxidation. Entries are ordered according to the largest loss rates by each process, calculated for F38. Entries marked by a hyphen were not included in the modeling.

Primary Loss by OH

	F26				F38				Muller et al. (2016)			
	OH	O_3	NO_3	*hv*	OH	O_3	NO_3	*hv*	OH	O_3	NO_3	*hv*
5-methylfurfural	100	0	0	0	100	0	0	0	100	0	0	0
2,5-dimethylfuran	100	0	0	0	100	0	0	0	100	0	0	0
Guaiacol	100	0	0	0	100	0	0	0	—	—	—	—
Furan	100	0	0	0	100	0	0	0	100	0	0	0
2-methylfuran	100	0	0	0	100	0	0	0	100	0	0	0
Acetic Acid	100	0	0	0	100	0	0	0	100	0	0	0
Propenoic acid	100	0	0	0	100	0	0	0	—	—	—	—
Acetic Anhydride	100	0	0	0	100	0	0	0	—	—	—	—
Methanol	100	0	0	0	100	0	0	0	—	—	—	—
Benzene	100	0	0	0	100	0	0	0	100	0	0	0
Toluene	100	0	0	0	100	0	0	0	—	—	—	—
Ethene	100	0	0	0	100	0	0	0	97	3	0	0
Formic Acid	100	0	0	0	100	0	0	0	100	0	0	0
Ethanol	100	0	0	0	100	0	0	0	—	—	—	—
Methyl acetate	100	0	0	0	100	0	0	0	—	—	—	—
m-xylene	100	0	0	0	100	0	0	0	—	—	—	—
Ethyl benzene	100	0	0	0	100	0	0	0	—	—	—	—
o-xylene	100	0	0	0	100	0	0	0	—	—	—	—
p-xylene	100	0	0	0	100	0	0	0	—	—	—	—
Acrolein	100	0	0	0	100	0	0	0	—	—	—	—
Methacrolein	100	0	0	0	100	0	0	0	97	1	0	3
Propenal	100	0	0	0	100	0	0	0	—	—	—	—
1,3-butadiene	100	0	0	0	100	0	0	0	—	—	—	—
Ethyne	100	0	0	0	100	0	0	0	—	—	—	—
Isoprene	100	0	0	0	100	0	0	0	98	2	0	0
1-pentene	100	0	0	0	100	0	0	0	—	—	—	—
1-butene	100	0	0	0	100	0	0	0	—	—	—	—
1-propene	100	0	0	0	100	0	0	0	96	4	0	0
Methyl vinyl ketone	99	0	0	1	99	0	0	1	93	4	0	3
Furanone	100	0	0	0	99	0	1	0	100	0	0	0
Styrene	100	0	0	0	98	0	2	0	96	3	1	0

Table S4. (Continued)

Significant loss by NO3

	F26				F38				Muller et al. (2016)			
	OH	O_3	NO_3	*hv*	OH	O_3	NO_3	*hv*	OH	O_3	NO_3	*hv*
Catechol	93	0	7	0	66	0	34	0	82	1	17	0
o-cresol	98	0	2	0	83	0	17	0	94	0	6	0
2,3-dimethyl phenol	98	0	2	0	84	0	16	0	—	—	—	—
p-benzoquinone	99	0	1	0	91	0	9	0	—	—	—	—
Phenol	99	0	1	0	88	0	12	0	97	0	3	0
monoterpenes	98	1	1	0	92	1	7	0	—	—	—	—

Significant loss by photolysis

	F26				F38				Muller et al. (2016)			
	OH	O_3	NO_3	*hv*	OH	O_3	NO_3	*hv*	OH	O_3	NO_3	*hv*
2-furfural	0	0	0	100	1	0	0	99	99	0	0	1
Acetone	18	0	0	82	16	0	0	84	77	0	0	23
2,3-butanedione	48	0	0	52	46	0	0	54	1	0	0	99
Methyl ethyl ketone	70	0	0	30	68	0	0	32	—	—	—	—
Benzaldehyde	74	0	0	26	73	0	0	27	—	—	—	—
Hydroxyacetone	93	0	0	7	91	0	0	9	88	0	0	12
Methyl glyoxal	93	0	0	7	91	0	0	9	—	—	—	—
Glyoxal	95	0	0	5	93	0	0	7	—	—	—	—
Formaldehyde	99	0	0	1	98	0	0	2	39	0	0	61
Acetaldehyde	98	0	0	2	98	0	0	2	95	0	0	5

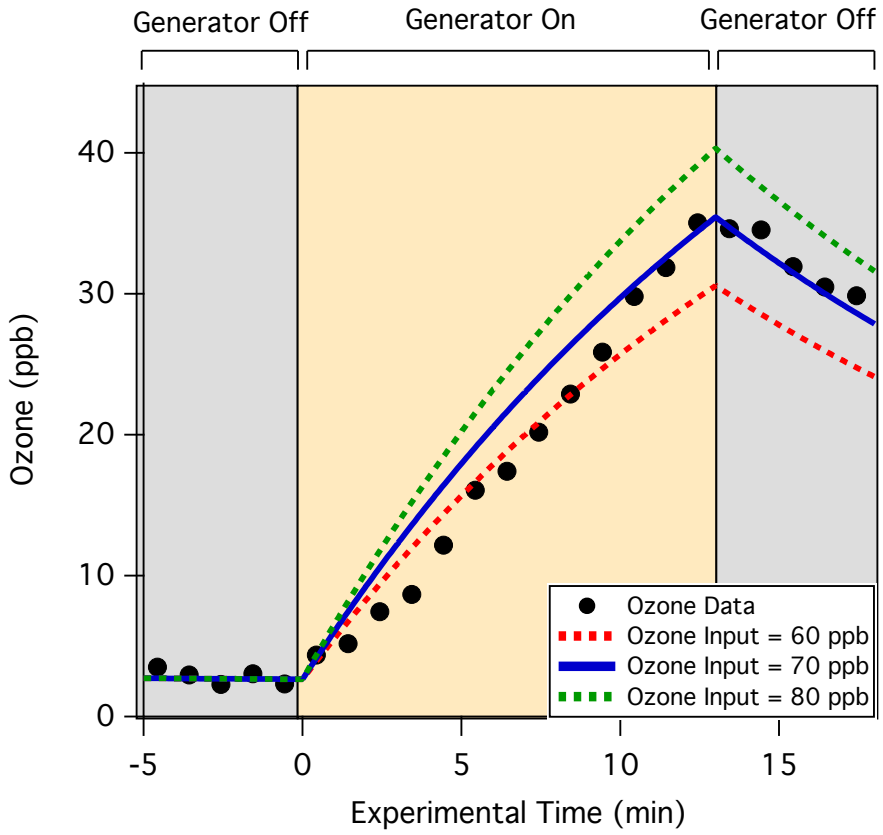

Figure S1. Modeled ozone compared to ozone measured during a dark, low NMOG (< 70 ppb) experiment. Output from the model is shown assuming that the dilution stream contains 60, 70, and 80 ppb of ozone. The input of ozone with the best fit (70 ppb) is applied to the photochemistry model described in Section 2.4

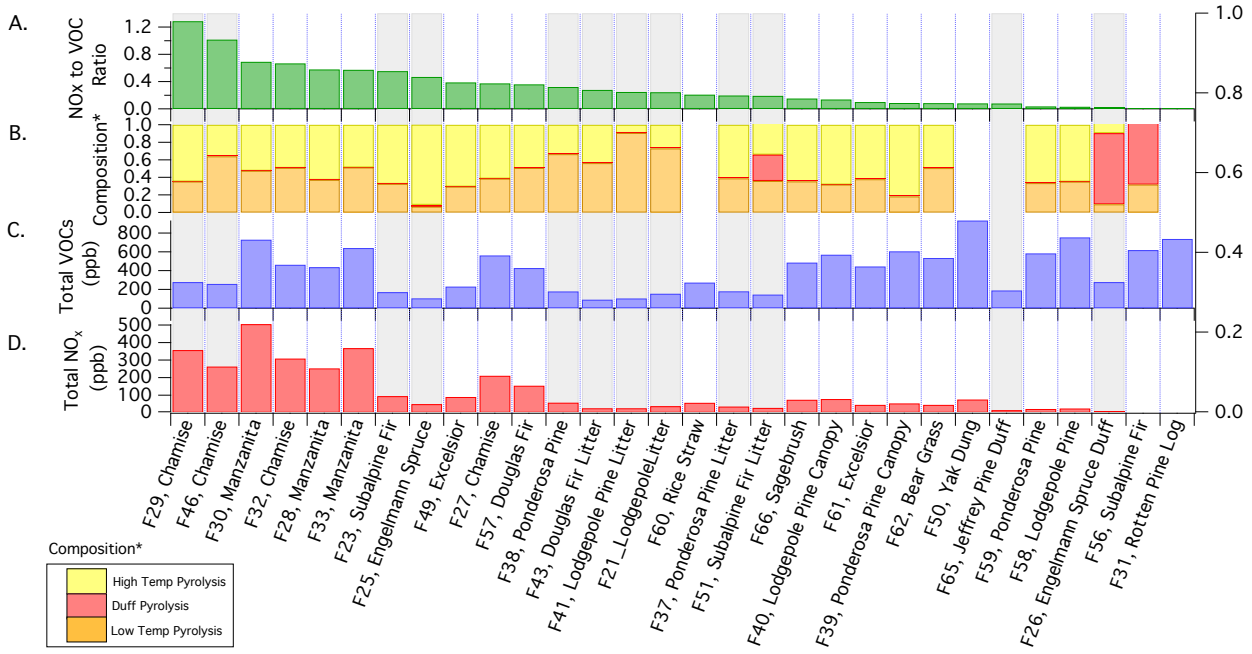

Figure S2. Small chamber (A) NO_x/NMOG ratio, (B) NMOG composition, (C) total NMOG loading, and (D) total NO_x prior to photochemical oxidation. Panel B shows the fraction of the total NMOG signal attributable to high temperature, low temperature, and duff pyrolysis as defined by Sekimoto et al. (2017). The grey bars indicate experiments in which initial NMOG loadings are sufficiently low to avoid significant OH titration.

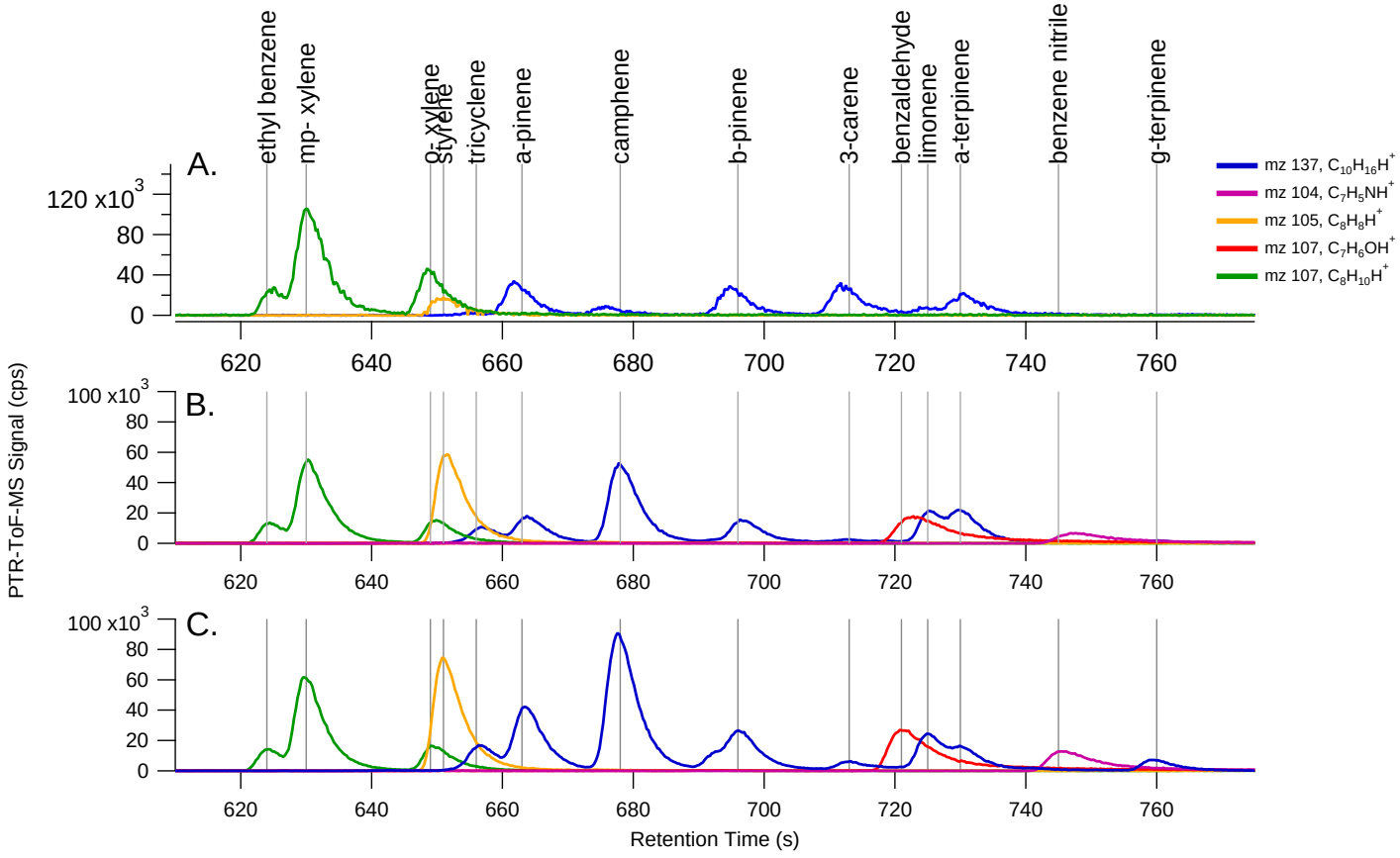

Figure S3. Distirbution of monoterpenes (*m/z* 137) and other select NMOG measured from the combustion of (A) Engelmann spruce, (B) Douglas fir, and (C) subalpine fir using GC-PTR-ToF-MS.

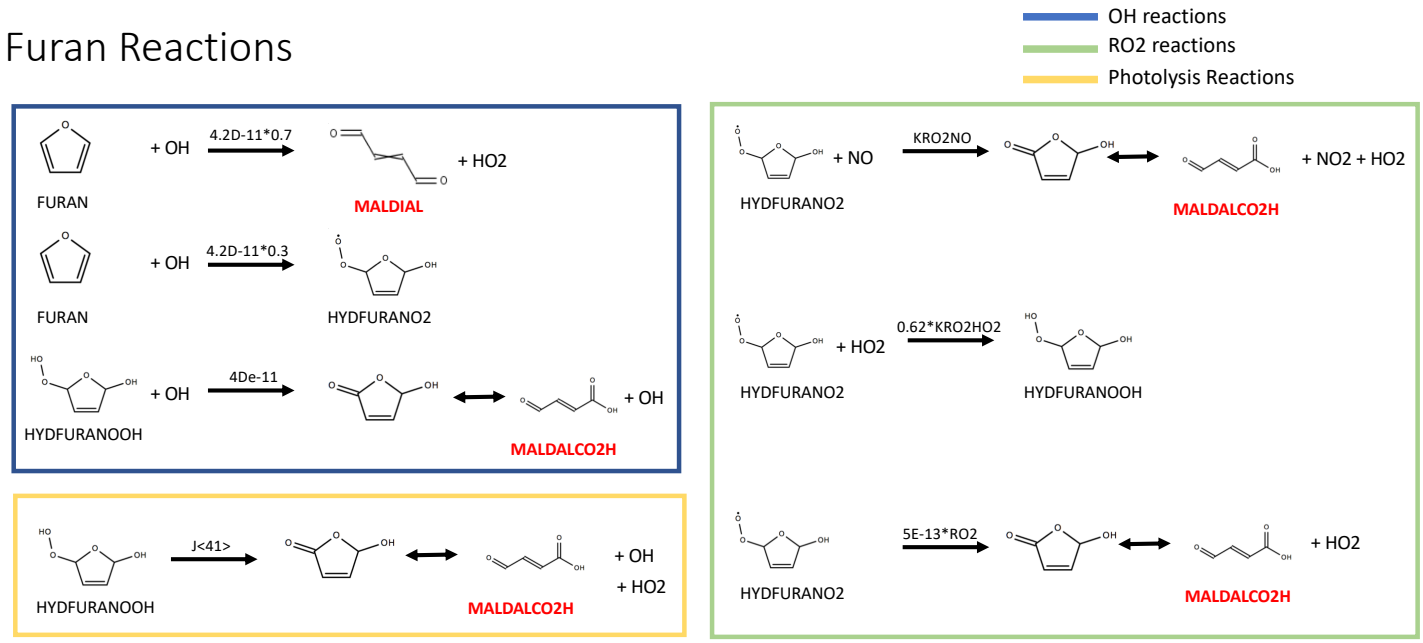

Figure S4. Furan reactions implemented into the MCM box model. Reactions are based on mechanism reported by Aschmann et al. (2014). Names in red indicate species currently represented in MCM v 3.3.1.

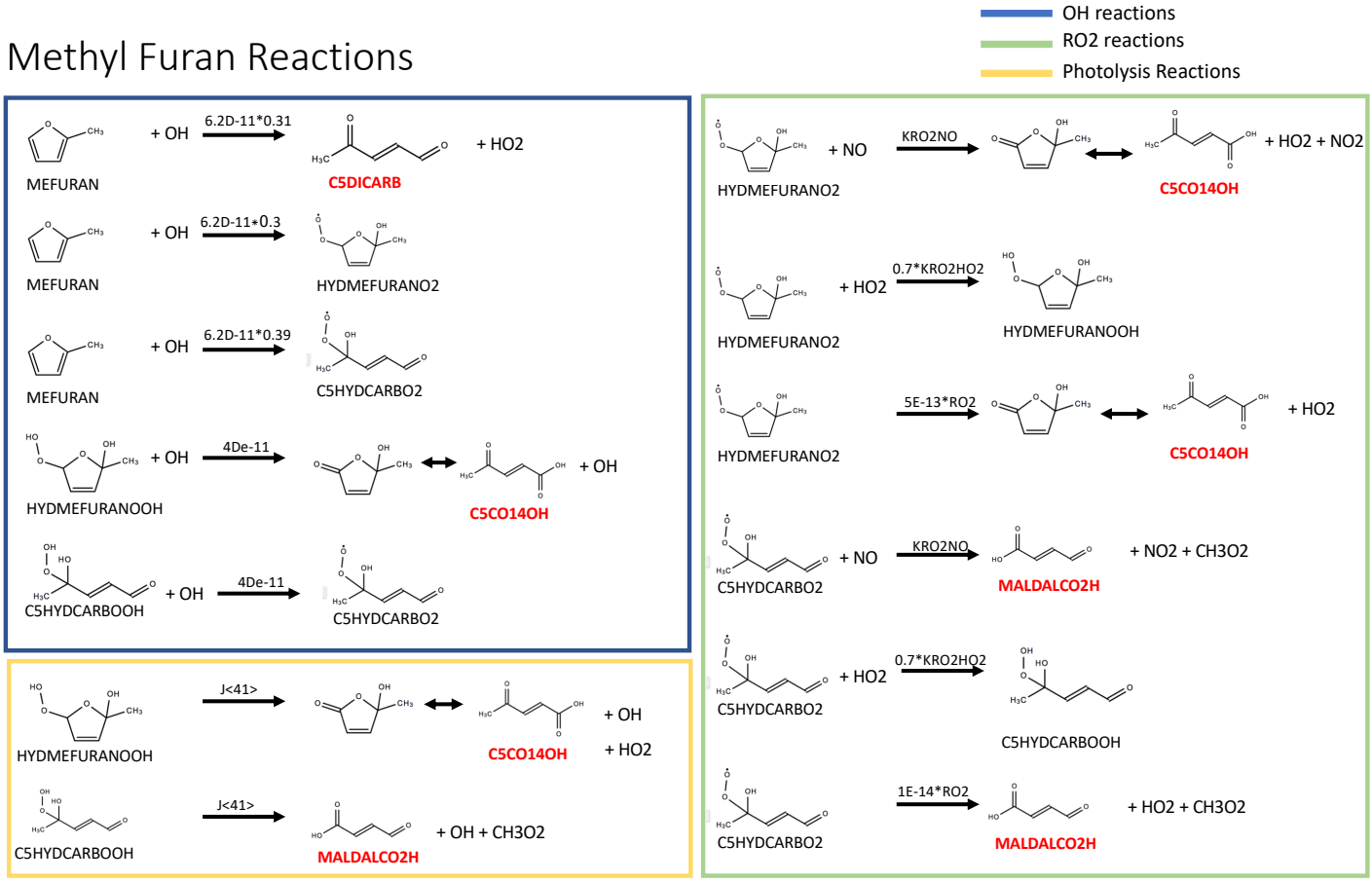

Figure S5. 2-methylfuran reactions implemented into the MCM box model. Reactions are based on mechanism reported by Aschmann et al. (2014). Names in red indicate species currently represented in MCM v 3.3.1.

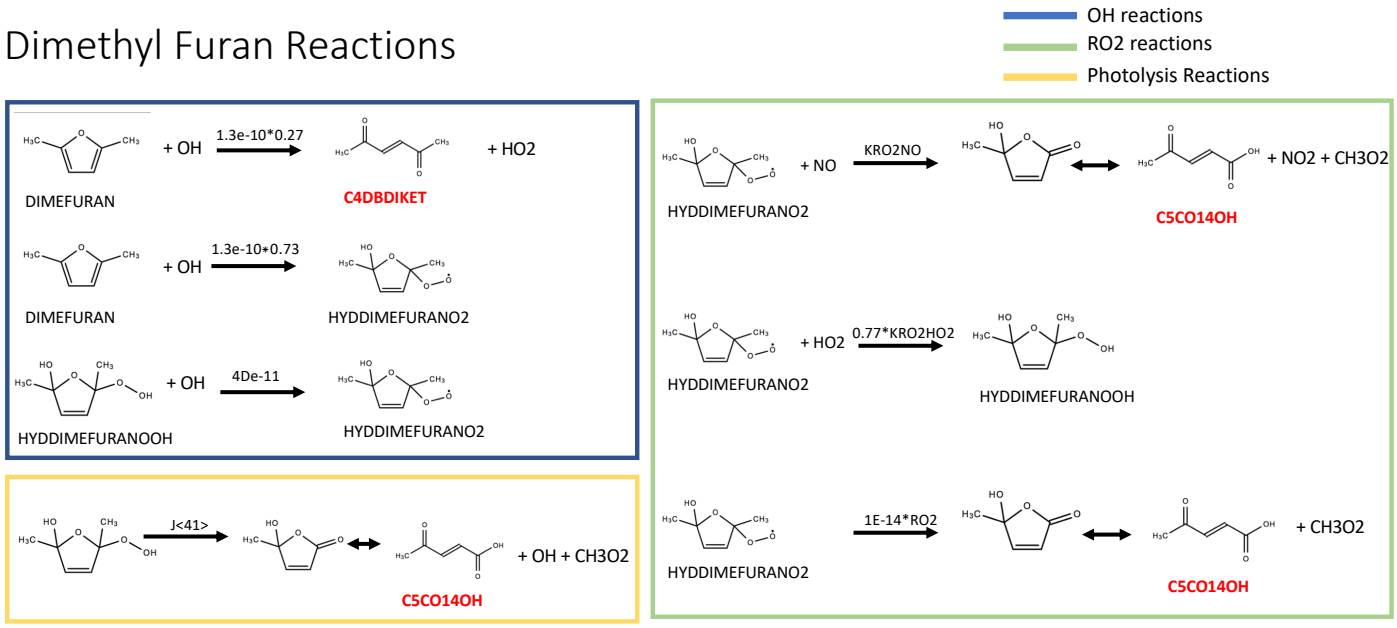

Figure S6. 2,5-dimethylfuran reactions implemented into the MCM box model. Reactions are based on mechanism reported by Aschmann et al. (2014). Names in red indicate species currently represented in MCM v 3.3.1.

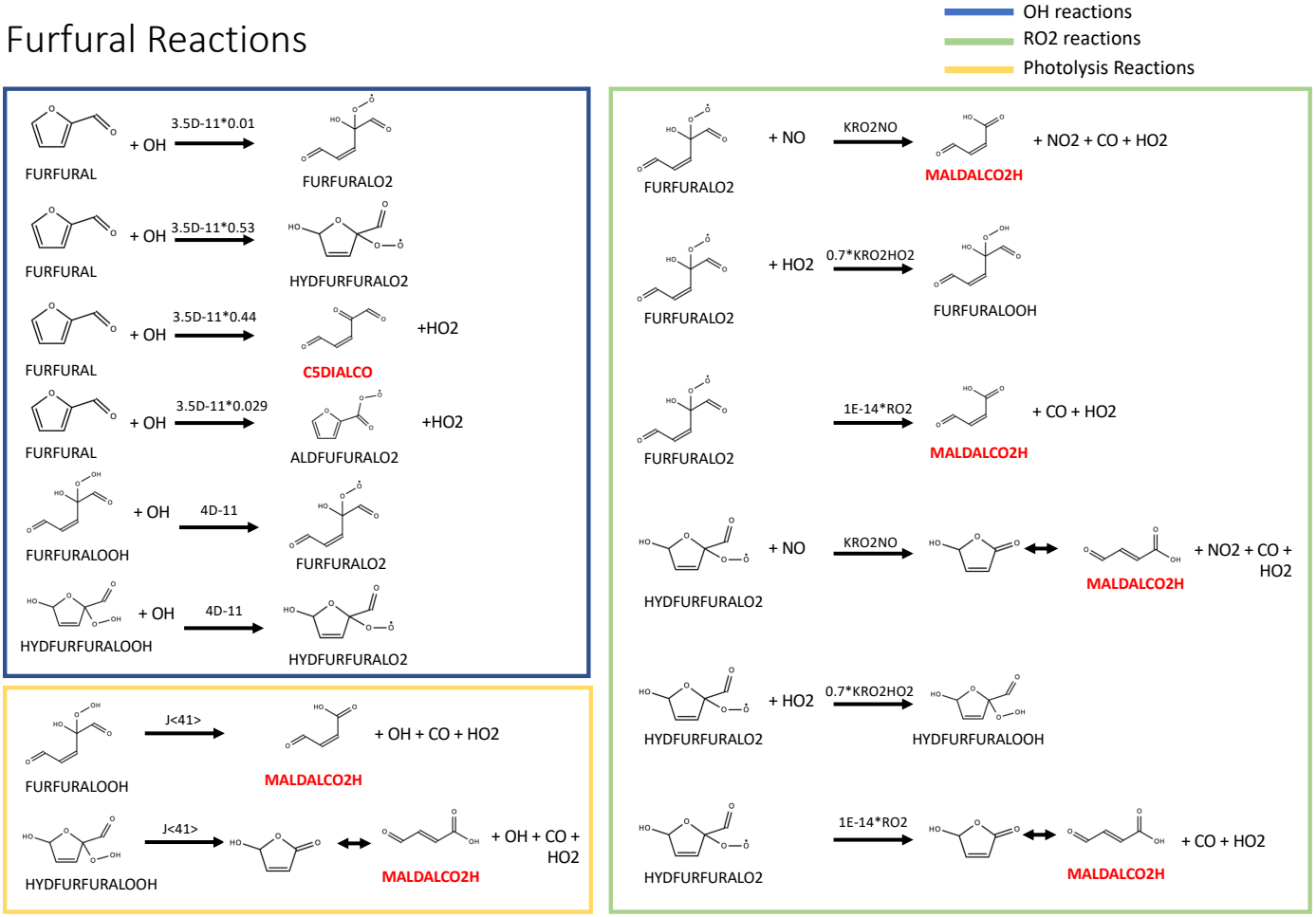

Figure S7. Furfural reactions implemented into the MCM box model. Reactions are based on mechanism reported by Zhao and Wang (2017). Names in red indicate species currently represented in MCM v 3.3.1.

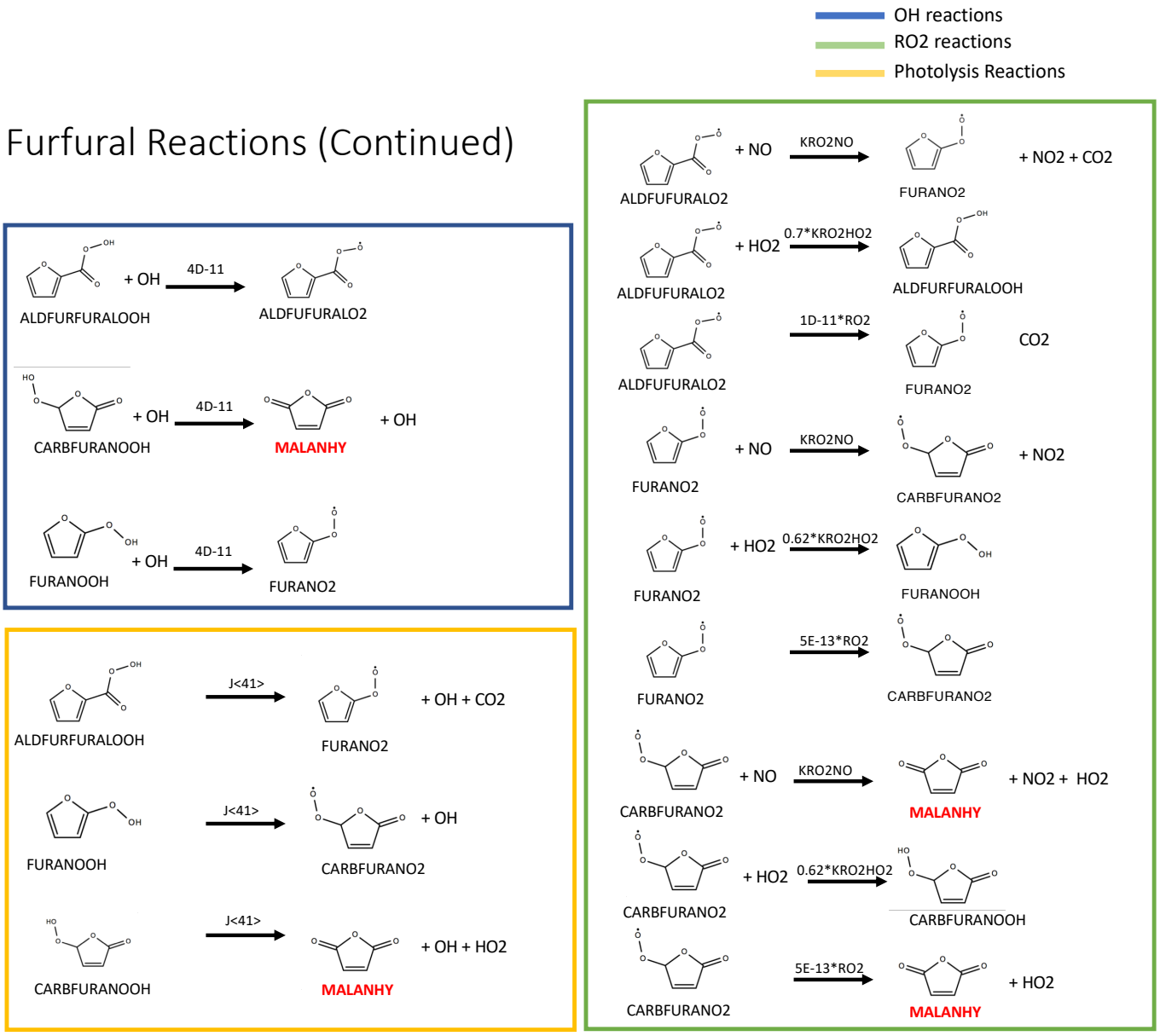

Figure S8. Furfural reactions implemented into the MCM box model (continued from Fig. S7). Reactions are based on mechanism reported by Zhao and Wang (2017). Names in red indicate species currently represented in MCM v 3.3.1.

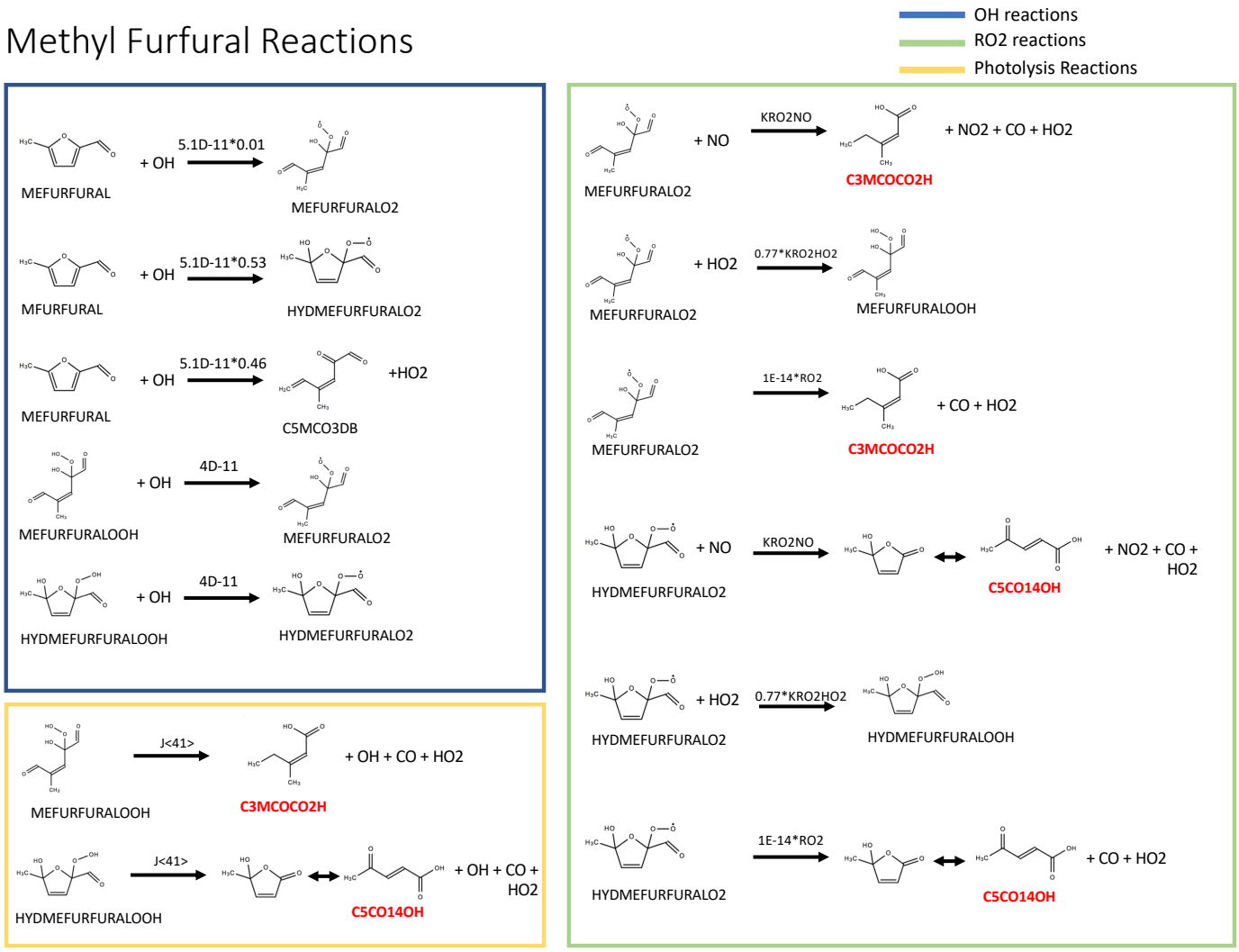

Figure S9. 5-methylfurfural reactions implemented into the MCM box model. Products and branching ratios are assumed to follow pathways analogous to the furfural mechanism reported by Zhao and Wang (2017). Names in red indicate species currently represented in MCM v 3.3.1.

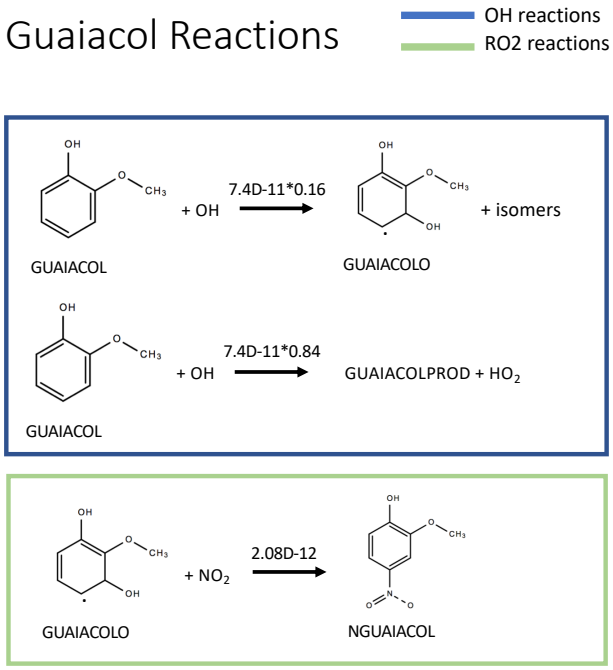

Figure S10. Guaiacol reactions implemented into the MCM box model. Reactions are based on the guaiacol mechanism reported by Lauraguais et al. (2014). GUAIACOLPROD is a generic, non-reactive product that is included to account for the fraction of guaiacol that does not react to form nitroguaiacols

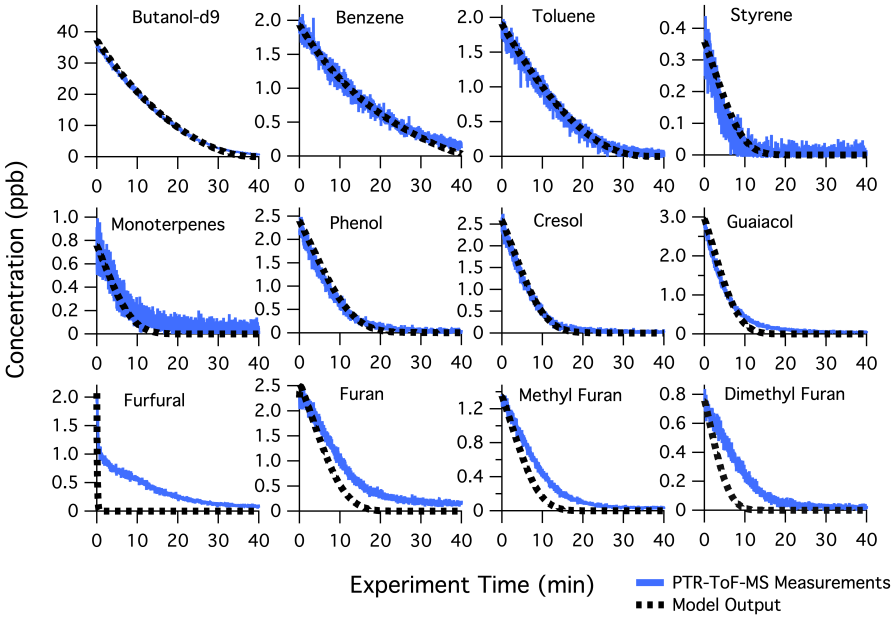

Figure S11. Primary NMOG measurements (blue lines) compared to modeled output (black dotted lines) for Fire 26. Fuel = Englemann Spruce Duff, NO_x/NMOG = 0.02, primarily duff pyrolysis NMOG mixture.

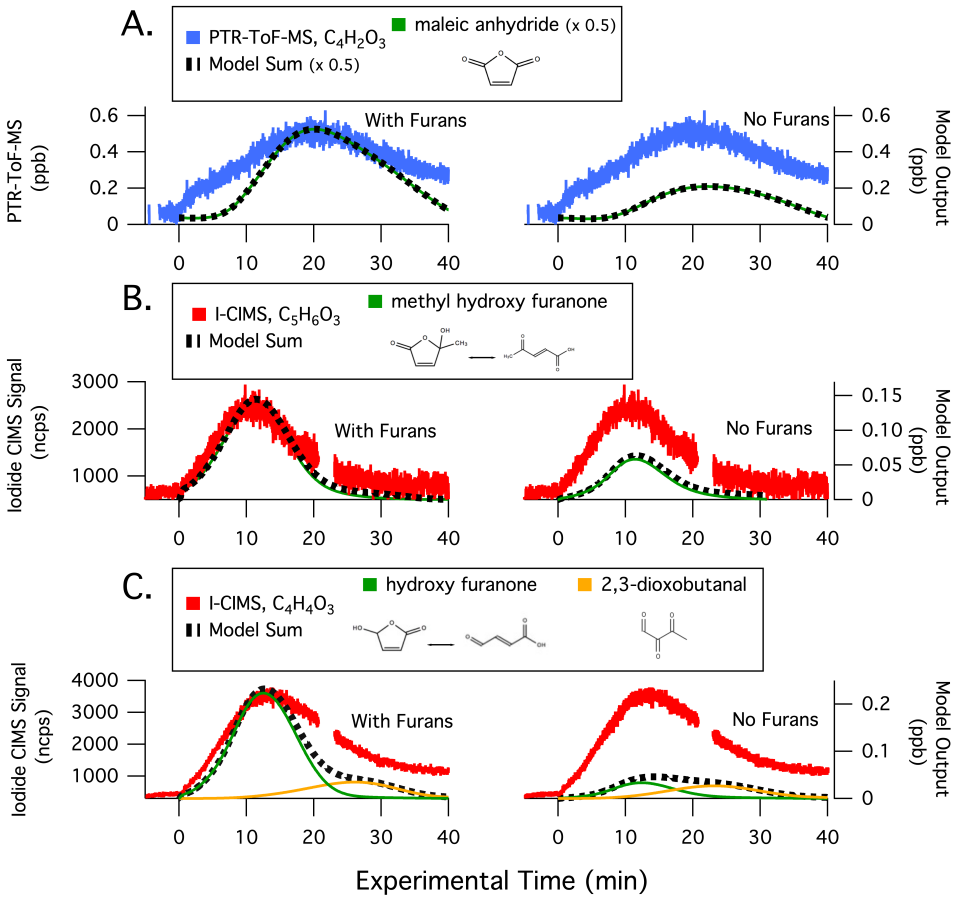

Figure S12. Secondary NMOG measurements compared to modeled output for Fire 26. Row (A) shows PTR-ToF-MS measurements of $C_4H_2O_3$ compared to model output of maleic anhydride. Row (B) shows I-ToF-CIMS measurements of $C_5H_6O_3$ compared to model output of methyl hydroxy furanone and its tautomer, β-acetylacrylic acid. Row (C) shows I-ToF-CIMS measurements of $C_4H_4O_3$ compared to model output of hydroxy furanone, its tautomer malealdehydic acid, and 2,3-dioxobutanal. All graphs to the left show full model runs, while graphs to the right show model runs when the initial conditions of furan, 2-methylfuran, 2,5-dimethylfuran, furfural, 5-methylfurfural, and furanone are set to zero

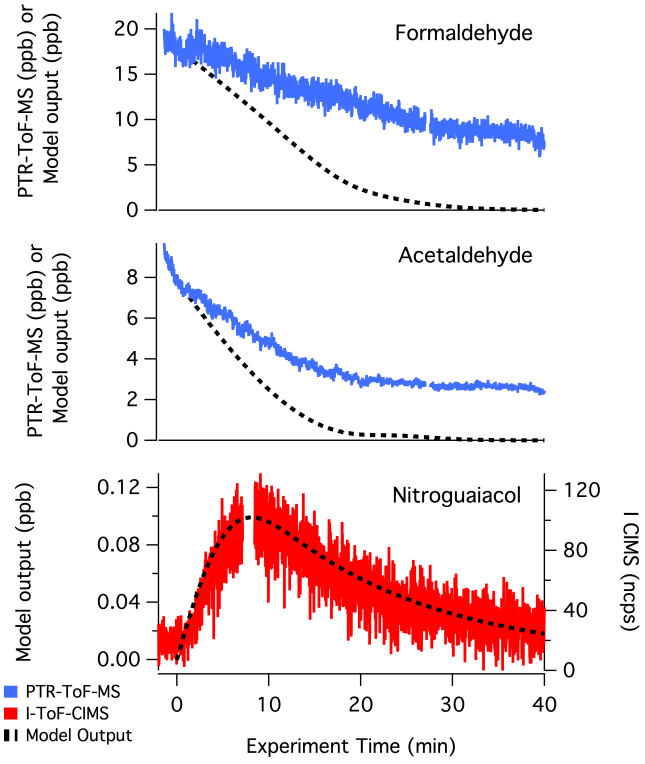

Figure S13. PTR-ToF-MS and I^--ToF-CIMS measurements of formaldehyde, acetaldehyde, and nitroguaiacol compared to model ouput for F38.

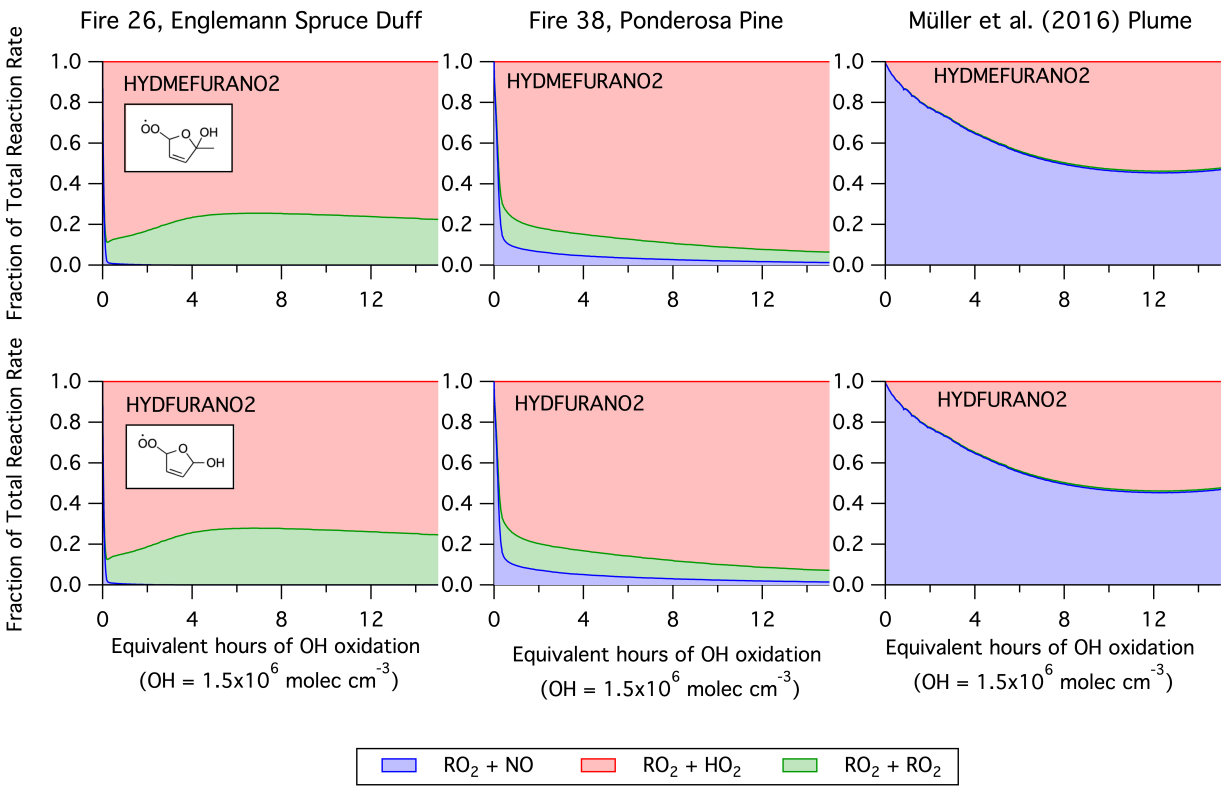

Figure S14. Fate of RO_2 species that lead to the formation of hydroxy furanone and methyl hydroxy furanone for F26, F38, and the ambient plume described by Müller et al. (2016). Shown is the fraction of RO_2 loss associated with reactions with HO_2, NO, and other RO_2 radicals.

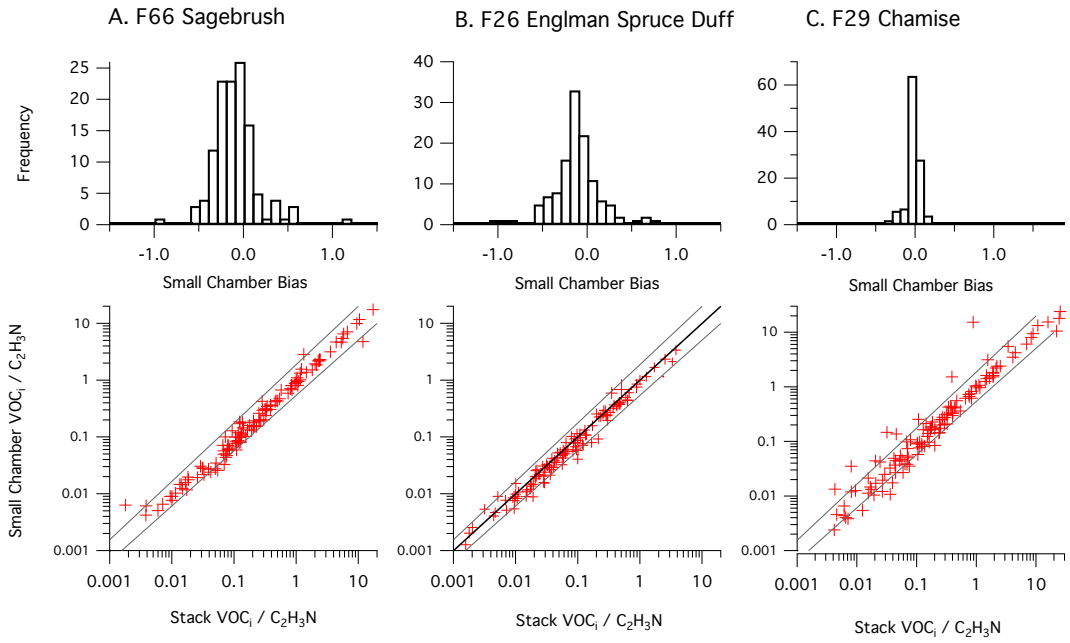

Figure S15. Comparison of NMOG distributions measured in the stack and small chamber prior to OH oxidation for (A) F66 - Sagebrush, (B) F26 - Englemann Spruce Duff, and (C) F29 Chamise. The bottom row shows the NMOG/C_2H_3N ratio for each species measured by the PTR-ToF-MS, along with 1:1, 2:1, and 1:2 lines.

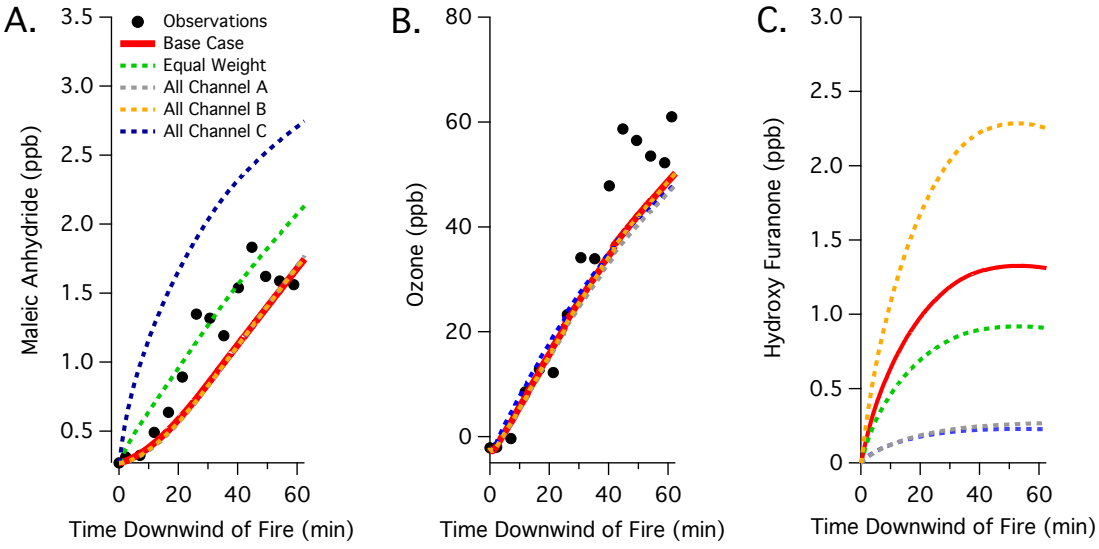

Figure S16. Model sensitivity of (A) maleic anhydride, (B) ozone, and (C) hydroxyfuranone to the assumed branching ratios of the furfural mechanism (Fig. 6). The "base case" simulation assumes branching ratios of A = 0.37, B = 0.6, B = 0.03 while the "equal weight" simulation assumes A = 0.33, B = 0.33, C = 0.33. All other simulations assume that furfural loss follows a single channel (i.e., all channel A, B, or C). Model output are compared to the measurements of maleic anhydride and ozone reported by Müller et al. (2016). Measurements of hydroxy furanone are not available.